Gas Chromatographic Microsystems: Development and Application to Problems in Homeland Security and Environmental Health

By

Gustavo Serrano

A dissertation submitted in partial fulfillment
of the requirements for the degree of
Doctor of Philosophy
(Environmental Health Sciences)
in The University of Michigan
2013

Doctoral Committee:

Professor Edward T. Zellers, Chair
Associate Professor Katsuo Kurabayashi
Assistant Professor Joseph T. Dvonch
Associate Professor Cagliyan Kurdak

DEDICATION

To My Parents, Maria Luisa and Manuel

ACKNOWLEDGMENTS

I was 23 years old when I traveled 3800 miles from Lima, Peru to Ann Arbor, MI to pursue my graduate studies at the University of Michigan. It was probably the most important decision I made in my life, and I knew when I made the decision that tough times were ahead. It was not an easy decision; being in my 20s and commiting to spend a lot of time, effort and dedication to do research requires a lot of encouragement and support, which can only come from your family. I want to thank with all my heart the great support and continuous encouragement I received from my parents and brother from the day I made the decision to come to Michigan, and up to these days.

Life and work in Ann Arbor for almost 6 years was marked by a wonderful wealth of friends, colleagues and collaborators. It will be hard to do justice to the many ways in which the people below have enriched the years at this wonderful city.

Thanks Ted, thanks for all your hard work, patience, and effort you dedicated in my training. I learned a lot under your guidance, and will always be grateful for that. A special thanks to my dissertation committee members, Dr. Katsuo Kurabayashi, Dr. Cagliyan Kurdak, and Dr Timothy Dvonch, for their insights, support, and time they put through the several milestones of my PhD candidacy.

I would also like to thank the Zellers group, current and former students. It was a great experience to be surrounded by such beautiful minds! Special thanks for those who trained me,

Shaelah Reidy (Sacks lab), Rebecca Veeneman, Judy Zhong, Forest Bohrer, and William Steinecker (Zellers Lab) for their patience and guidance. Special thanks to Thitiporn Sukaew, Will Collin, Lindsay Wright, Hungwei Chang, Nicolas Nunovero, Sung-Jin Kim (Kurabayashi lab), and Dibyadeep Paul (Kurabayashi lab), whowere my closer collaborators and with whom I will always share the co-authorships of several papers. Without them, it would have not been possible to finish this dissertation. Special thanks go to the staff affiliated with the Center for Wireless Integrated MicroSensing and Systems ($WIMS^2$), in particular Robert Gordenker, Katharine Beach, and Brendan Casey for their technical support and assistance, and Karen Richardson and Jonathan Plummer for their administrative assistance.

Finally, I want to acknowledge the institutions from which funding was obtained to support this research: the Department of Homeland Security, Science and Technology Directorate under Cooperative Agreement 06-G-024, the $WIMS^2$ Center, which is sponsored by the Engineering Research Centers Program of the National Science Foundation under Award Number ERC-9986866, and Agilent Technologies, which provide unrestricted gift funding to my advisor.

These pages are dedicated to you.

TABLE OF CONTENTS

LIST OF FIGURES

Figure

LIST OF TABLES

Table

CHAPTER I

INTRODUCTION

1.1 Dissertation overview

This dissertation describes a series of projects related to the development and characterization of microanalytical systems for trace-level determinations of airborne volatile and semi-volatile organic compounds (VOCs and SVOCs) in complex mixtures. A primary emphasis is placed on a gas chromatographic microsystem (μGC) designed for rapid determinations of the following marker compounds for the explosive 2,4,6-trinitrotoluene (TNT): 2,4-dinitrotoluene (2,4-DNT), 2,6-dinitrotoluene (2,4-DNT), and 2,3-dimethyl-2,3-dinitrobutane (DMNB) at sub-ppb concentrations (Figure 1-1). A secondary focus is placed on developing a comprehensive two-dimensional gas chromatographic system (GC×GC) that employs a novel micro thermal modulator (μTM) developed by collaborators in the Kurabayashi Lab in the Mechanical Engineering Department. The research has direct relevance to environmental and occupational health sciences, specifically to the development of novel direct-reading instrumentation for near-real time vapor monitoring at levels useful for homeland security, exposure assessment, and emergency response applications.

Relatively few reports of fully integrated μGC systems have been published to date [1-15], and none has focused on explosive markers. The μGC system described in this dissertation, dubbed INTREPID, is part of an ongoing effort in the Center for Wireless Integrated Microsensors and Systems ($WIMS^2$) at the University of Michigan concerned with the development of μGC

instrumentation (Figure 1-2) [16]. INTREPID has benefited from lessons learned in building other WIMS^2 μGC components and prototypes [3-10], but it incorporates several unique design and operational modifications to optimize it for the determination of the target analytes. INTREPID is designed to preconcentrate, inject, separate, and detect/recognize target vapors at sub-parts-per-billion concentrations in complex mixtures in as short a time period as possible. The key components are a pre-trap, a front-end high-volume sampler (not microfabricated), a micro-focuser (μF), a wall-coated microcolumn, and a chemiresistor (CR) array detector that uses monolayer-protected gold nanoparticle (MPN) interface layers (Figure 1-3).

Chapter 1 provides the background and significance of the research. Chapter 2 describes the development and testing of the front-end preconcentrator/focuser (PCF) module to be used with INTREPID. The work described in this chapter has been submitted for publication in the Journal of Chromatography A. Chapter 3 describes the design and development of the INTREPID laboratory prototype (INTREPID-I). This chapter also includes component-level and sub-system level testing focused on optimizing conditions prior to system integration, and on improving our understanding of key operating parameters. Results from this work were used to guide the design, assembly, and laboratory characterization of the field-deployable INTREPID μGC prototype (INTREPID-II), described in Chapter 4. The work described in this chapter will be submitted for publication in a peer-reviewed scientific journal. Chapter 5 describes the development and assembly of a GC×GC system using a μTM. This chapter was recently published in the journal Analytical Chemistry [17]. Chapter 6 summarizes the key findings and major contributions of this research and suggests future studies.

In summary, this dissertation entails several independent yet interrelated projects, each of which makes a significant contribution to the advancement of micro analytical systems, as the next

generation of portable direct-reading instrumentation for complex VOC mixtures of relevance to homeland security and occupational and environmental health.

1.2 Background and significance

1.2.1 Portable direct-reading instruments

On-site VOC monitoring with portable direct-reading instruments has been practiced for the last 40 years [18-46], and numerous manufacturers currently market compact instruments for field deployment [33-46]. However, currently available portable instruments are generally too large and expensive for routine implementation, only a few of them can provide determinations of multiples VOCs, and most lack the inherent sensitivity to detect the low-/sub-parts-per-billion concentrations demanded in many of these applications [47].

Technologies adapted for field use that are capable of generalized multi-VOC determinations are based on Fourier transform and single beam infrared (IR) spectrophotometry [18,19,33-35], direct-inlet mass spectrometry (MS) [20-24], ion mobility spectrometry (IMS) [25-27], and gas chromatography with various detectors (GC-flame ionization detector (FID), GC-photoionization detector (PID), GC-thermal conductivity detector (TCD), GC-surface acoustic wave (SAW), GC-mass spectrometry (MS) [28-32, 39-45]. So-called 'electronic noses', which generally consist of a set of sensor arrays whose collective response patterns are analyzed, are also among the current direct-reading monitoring systems available [46]; however they are not capable of quantitative multi-vapor analysis [48].

Portable GCs are probably the most common direct-reading instruments used for determinations of multiple VOCs in environmental and occupational health applications, in particular GC/MS systems. The reason why they are so popular is because of their ability to

provide unequivocal identification of eluting analytes by the combination of retention time and the fragmentation pattern/spectrum created by the MS detector. Among the portable commercial GC-MS systems, the Griffin 460 (~96 lbs, FLIR, Portland, OR) uses cylindrical ion trap (CIT) technology-and can detect VOCs at the ppt-level (with preconcentration) [39], and the TRIDION-9 (32 lbs, Torion, American Fork, UT) uses a miniaturized toroidal ion trap mass spectrometer, and can also detect VOCs at the ppt-level [41]. Portable GCs, however, have not been widely used for the analysis of explosives; only one report was found in the literature [32].

The most popular technique for portable instrumentation specifically adapted for the analysis of explosives is IMS technology [49]. The main advantage of this technique is its very high sensitivity for many explosive compounds and ease of operation, however it can suffer from ion suppression from other species in the environment, creating false positive alarms. Other techniques applied with relative success for analysis of explosives include MS, Raman scattering, fluorescing polymer sensors and GC coupled to MS and IMS [50-51]. Most of these systems, however, are not designed for standoff detection, and an operator is required to handle the potential threat to collect a swab sample [50]. Recently, many of these instruments are being adapted for standoff detection by implementing inlets more amenable to vapor analysis, which include high-volume samplers with filters [52-54], automated solid-phase micro extraction (SPME) [55], and micropreconcentrators [56-58].

1.2.2. Miniaturization of direct-reading instruments for VOC analysis

Over the last three decades, numerous efforts have been mounted toward the miniaturization of common analytical instruments [1-15, 59-63]. The key enabler is micro-electromechanical systems (MEMS) technology, a method of forming complex structures using microfabrication steps such as photolithography, deep reactive ion etching and

metallization, often on silicon substrates. Reports have appeared on MEMS-based MS [59], IMS [60], IR spectrophotometers (FTIR and Quantum Cascade Laser (QCL) array IR [61-63], and GC systems [1-15]. MEMS-based MS systems have been reported by Muller *et. al.*, and consist of a fully integrated MS on one chip with exterior mini-pumps [54]. Separation and identification of some gases was achieved within seconds, however it still has LODs of several hundred ppb, and limited resolution for differentiating components. There has also been a significant amount of research on miniaturized IR instruments, but due to the principle of IR, there are some inherent limitations towards miniaturization, including the use of smaller mirrors that reduces resolution [61]. The long path required for increased sensitivity and the power requirements for temperature control of the source and detector are also factors that limit the performance of miniaturized IR [62].

The most successful instrumentation miniaturized using MEMS technology is GC. The earliest report of a μGC was from Terry *et. al.* in the late 1970s [1]. Over the ensuing 30 years, several subsequent reports have appeared on μGC components, including micropumps [64], micropreconcentraotrs [56-58, 65-77], microcolumns [78-95], microthermal modulators [96-99], microsensor detectors [100-118], and μGC subsystems [119-122]. In general, these consist of a separation column coupled with one or another sampling, preconcentration, and/or detection device that may or may not have been microfabricated. Relatively few efforts have been successful, however, in integrating these into working microsystems. The small number of such reports attests to the challenges associated with microsystem integration.

Several years ago, Zellers, *et al.* described the first laboratory prototype μGC capable of determining the components of VOC mixtures at ppb concentrations [10]. That μGC included a microfabricated preconcentrator/focuser (PCF), a 3-m microfabricated separation column, and a

detector consisting of an integrated array of four chemiresistor microsensors that employed thiolate-monolayer-protected gold nanoparticles (MPN) as the interface layers. Since then, they have continued to improve the performance and expand the capabilities of the μGC components and recently, we reported on the first field-deployable μGC, capable of multiple VOC determination at sub-ppb concentration [3-5]. Recent reports have also shown progress towards μGC×μGC systems with microfabricated thermal modulation [96-98].

The μGC systems developed for this dissertation are a step forward in the development of portable systems for the analysis of explosive vapors. These MEMS-based microsystem provide various capabilities not found in other instruments used for explosive analysis, such as stand-off detection, low limits of detection, high sensitivity and selectivity, and fast analysis times.

1.2.3. Preconcentration and focusing (sampler/focuser)

Since most detector technologies are not sensitive enough to detect low concentrations (i.e., parts-per-billion to parts-per-trillion) of VOCs often encountered in indoor and ambient environments, it is necessary to employ a preconcentration step, in which a large volume of ambient air is captured onto a bed of adsorbent material and then thermally desorbed into a much smaller volume. The preconcentrator may also serve as the injector of the captured VOCs by focusing the vapor-mixture plug onto the separation column after desorption from the sorbent bed. This is a critical role in separation, because chromatographic resolution is improved by narrower injection bands at the head of the column.

The two most common approaches to preconcentration for field portable systems are the collection of discrete air samples via solid-phase microextraction (SPME) [39, 41, 123, 124] or conventional sampling tubes containing a granular adsorbent material [66, 125-133]. In the latter,

a large volume of ambient air is captured by physisorption onto a bed of the adsorbent material and then desorbed into a smaller volume. The extent of adsorption at a given vapor-phase concentration of the analyte is determined by the volatility of the vapor, intermolecular forces of attraction between adsorbate and adsorbent, the surface area available on the solid adsorbent, temperature, flow rate and mass of adsorbent [134,135]. One of the most common adsorbent materials used for preconcentration is graphitized carbon, which is available in a range of particle sizes and surfaces areas. Among the advantages of graphitized carbon is its low affinity for water vapor and high thermal stability [136-142].

A modified version of the Wheeler-Jonas equation, often call the reaction kinetic equation, is widely used to predict breakthrough of volatile organic compounds on granular activated carbon. The breakthrough curve, a plot of the concentration of the compound exiting a packed carbon beds vs. time at a fix flow rate, is described by this equation [133, 135]:

$$t_b = \frac{W_b W_e}{C_o Q} - \frac{\rho_B W_e}{C_o k_v} \ln \frac{C_o}{C_x} \quad (1)$$

where t_b is breakthrough time, W_e, the adsorption capacity (g/g carbon), which is a gas/carbon interaction parameter, Q, the air flow rate (mL/min), C_o, the initial concentration of the compound (g/cm^3), C_o/C_x, the fraction at t_b, ρ_B, the packed density (g/mL), and k_v, the adsorption rate coefficient (min^{-1}), which is another gas/carbon interaction parameter. This equation can also be re-organized around the breakthrough volume, V_b, a performance parameter of a more general interest, which is more easily related to operating variables.

$$V_b = \frac{W_e W_b}{C_o} - \frac{Q W_e \rho_B}{k_v C_o} \ln \frac{C_o}{C_x} \quad (2)$$

With eq. 2 some tradeoffs in performance can be established, and it is clear that V_b will have a dependency on variables such as Q (flow rate), W_b (mass of adsorbent), and C_o (concentration of the compound). Chapter 2 will focus on the practical implications of the influence of those variables on the breakthrough volume; however, the Wheeler model will not be used as a framework for those tests.

Most of the commercial direct-reading instruments that include a preconcentration step use an adsorbent material packed in a tube, a pump for collecting the sample and a heater for thermal desorption of the trapped samples. For example, the Inficon Hapsite® portable GC/MS which uses a glass fritted tube packed with Tenax® and carbon adsorbents inserted into a proprietary thermal desorber [40]. Other popular commercial field-portable instruments, such as TRIDION-9 from Torion, use SPME technique [41].

In the literature, there are several articles related to adsorbent-based preconcentration for field instruments [126-133]. In most cases, these preconcentrators consist of a glass or metal tube filled with adsorbent and wrapped with nichrome, Ta, or Pt wire for heating and thermal desorption. For example, Sacks *et. al.* [126, 129, 130] reported studies of multi-bed sorption preconcentrators for bench-scale gas chromatography applications, Zellers et. al. [132-133] developed multi-bed preconcentrators for portable gas chromatography and microsensor array systems. Rapp *et al.*[131] used a preconcentrator made of glass tube and packed with Tenax for a surface acoustic wave (SAW) micro sensor array system. Cho *et al.* used a dual-stage preconcentrator to trap VOCs from exhaled human breath and inject them into an electronic nose [127], and Song et al. reported a novel method to heat the adsorbent material, consisting of a ceramic heating material instead of the conventional glass or metal tubes, which allows for direct heating of the adsorbent material [125].

Despite their major advantages and wide use, tubular preconcentrators also present some disadvantages. They are often long and packed with significantly amounts of adsorbent material, which leads to large dead volumes and low heating efficiency due to their large thermal mass. These restrictions are very often reflected in the less volatile analytes, which takes longer to be desorbed, producing broader desorbed peaks. [133].

To overcome these issues, miniaturized preconcentrators fabricated in Si using MEMS technology have being developed. These micropreconcentrators (μPC), due to their smaller size, significantly reduce dead volume, thermal mass, and power consumption. A number of microfabricated preconcentrator devices have been reported in recent years. [56-58, 65-77] Manginell *et. al.*, [69, 77] developed a mass-sensitive micropreconcentrator used in the μChemLab system developed by Sandia National Labs [13], and also in Canary-Three, a hand-held chemical detector developed by Defiant Technologies [2]. It consists of a 1.5 x 0.6 mm microhotplate with a proprietary selective adsorbent coating applied to it surface. It can achieve 200 °C in ~ 20 ms with roughly 130 mW of electrical power. Zellers *et. al.* reported on the modeling, development, and characterization of multi-stage micropreconcentrators/focusers (μPCF) loaded with carbon-based adsorbents of different surface areas [73, 75, 76]. This μPCF achieved a preconcentration factor, which is the ratio of the concentration of the analyte in the sample delivered to the detector to the concentration originally presented in the inlet airflow, of > 5600 [76]. This μPCF was successfully integrated into the first all-MEMS μGC [10].

A novel approach was pursued by Agah *et. al.*, [67, 68, 70] who fabricated a high-aspect-ratio μPC with embedded pillars for enhanced air distribution. That device was coated with Tenax TA and an enhancement factor of 1000 was claimed. Lastly, two reports documented the use of μPCs for the collection and thermal desorption of explosive vapors. Voiculescu *et. al.*

demonstrated the use of a CMOS preconcentrator coated with a proprietary sorbent polymer attached to an IMS spectrometer, capable of enhancing the sensitivity and selectivity to TNT vapors by three orders of magnitude [56]. In the other article, Martin et. al. showed a large MEMS preconcentrator (6.65 x 6.65 mm) coated also with a proprietary sorbent polymer [57]. This preconcentrator could only achieve modest desorption temperatures (120 °C in 200 ms), and sensitivity to TNT vapors increased only one order of magnitude, compared to no preconcentration. This report however, addresses a shortcoming of typical μPCs, the inadequate sampling flow rates. This μPC can operate up to 400 mL/min, the highest flow rate published for a μPC to date. In general, microfabricated preconcentrators have not been tested with large sample volumes, due, in part, to the relatively low flow rates that μPCFs can achieve, and to the small amount of adsorbent used in the μPCF, that reduce the adsorption capacity and thus, the breakthrough volume. Another factor that has not been generally considered in the design of microfabricated preconcentrators is the competition among high-boiling point co-contaminants and target vapors for sorption sites that may also change the degree of sorption at a given target-vapor concentration. Zellers et. al. explored the use of multi-stage preconcentrators to overcome this issue, but the problem remains if single-stage preconcentrators are to be used [76].

In this dissertation, we describe the design and analytical performance of a multi-stage preconcentrator-focuser (PCF) module consisting of a conventional tubular sampler and a microfabricated focuser (μF), shown in Figure 1-4. With this module, we address the respective shortcomings of the tubular and microfabricated preconcentrators by using them in tandem. The high-volume sampler is used as a first preconcentrator stage in which large volumes of air can be collected in a short period. The μF is used as a second preconcentrator stage, to which the sample collected in the tubular sampler is transferred by thermal desorption, focused, and injected to a

downstream separation column. This configuration allows us to collect a large sample volume in very short period of time while still being able to inject sharp injection plugs into the column. Similar to the multi-stage PCF module described by Sukaew *et. al.* [66], this module is optimized for the selective capture of explosive markers. Ultimately, the PCF module will be interface with the μGC we are constructing for the high-speed determination of explosives markers.

1.2.4. Separation (microcolumn)

Microfabricated GC columns (microcolumns) have received interest due to their small size, low power requirement for heating and batch manufacturing [78-95]. A typical microcolumn structure consists of a deep-reactive-ion-etched (DRIE) Si channel with rectangular or round-shape cross section that is 0.25 – 3 m in length. An anodically bonded Pyrex cover plate is used to seal the open Si channel. As with most commercially available fused-silica capillary columns, a thin layer of a polymer stationary phase is deposited on the channel walls, using a static or dynamic coating method [82,85,90]. Microcolumns packed with an adsorbent material or gold nanoparticles have also being reported [95]. Separation is based on the partitioning of an analyte between a stationary phase (often a liquid silicone-based polymer) and a mobile phase (i.e., a carrier gas such as air, He, H_2). Several laboratories have reported on the development of microfabricated GC columns, however only Sacks et. al. [85-87], Radadia et. al. [80, 83], Agah et. al. [79, 81] and Zellers et. al. [82, 84] have reported high efficiency microcolumns.

The Golay equation is used for describing the column efficiency, and is the measure of the band broadening phenomenon that is observed for any component eluting in the column [143]. The column efficiency is characterized by the height equivalent to the theoretical plate (H), or the plate number (N, the ratio of the length of the column to the plate height, H). For open tubular columns

(i.e., most microcolumns), there are four additive terms that contribute to the band broadening and that are reflected in the Golay equation. The diffusion in the mobile phase (B), the resistance to mass transfer in the mobile phase due to non-uniform velocity field (C_g), the resistance to mass transfer in the stationary phase (C_l), and extra-column band broadening term. Equation 1 shows the simplified version of the Golay equation with those terms.

$$\boldsymbol{H = \frac{B}{v} + C_g v + C_l v + D v^2} \tag{3}$$

Where v is the cross-sectional linear velocity of the carrier gas. The plate height contribution by the diffusion in the mobile phase (B) can be expressed as:

$$\boldsymbol{H_B = 2\frac{D_m}{v}} \tag{4}$$

Where D_m is the diffusion coefficient of the component in the mobile phase. The plate height contribution by the resistance to mass transfer in the mobile phase (C_g) can be expressed as:

$$\boldsymbol{H_{Cg} = \frac{1+6k+11k^2}{24(k+1)^2} \times \frac{r^2 v}{D_g}} \tag{5}$$

Where k is the retention factor, and r the radius of the column. The plate height contribution by the resistance to mass transfer in the stationary phase (C_l) can be expressed as:

$$\boldsymbol{H_{Cl} = \frac{2k}{3(k+1)^2} \times \frac{d_f^2 v}{D_l}} \tag{6}$$

where d_f and D_l are the film thickness of the stationary phase and the diffusion coefficient of the

component in the stationary phase, respectively.

Experimental parameters need to be properly selected and optimized to minimize band broadening from these factors. A model has also been developed for rectangular cross-section channels, as used in microfabricated columns [144]. This model, which is a modified version of the Golay equation, takes into account the aspect ratio of the rectangular channels to describe band dispersion. This modification only affects the H_{Cg} term, which is dependent on the column cross-section. The proposed expression by Spangler for the H_{Cg} term is:

$$\boldsymbol{H_{Cg} = \frac{0.9+2k+35k^2}{96(k+1)^2} \times \frac{w^2\mu}{D_g}} \quad (7)$$

where w is the width of the rectangular channel, with an aspect ratio (i.e., ratio of depth to width of the column cross-section) approaching infinity. The Golay equation can be used to calculate *H* minimum at a velocity in which the forces leading to peak dispersion are minimized. Minimizing *H* leads to a larger value of N and therefore a more efficient separation. Other metrics developed to measure and compare column efficiency are peak capacity (n_p), which is the number of perfectly spaced peaks that can be fit into a given chromatographic space, and resolution (R_s), a metric that quantifies the degree of separation of two compounds [143].

1.2.5. Detection/Recognition (microsensor array)

Low-power microsensors have been critical to the development of miniaturized VOC monitoring instrumentation [100-118]. Most gas/vapor microsensors rely on partitioning of target molecules into a thin film of ad/absorptive interface material on the surface of a substrate that is probed electrically, mechanically, thermally, or optically.

Recent notable efforts focused on explosives detection include: a single optical detector based on fluorescence quenching of a pentiptycene-based polymer that occurs upon exposure to target vapors with fairly high selectivity [145-147]. Other efforts includes surface acoustic wave (SAW) sensors coated with carbosilane polymers containing fluoro-alcohol side groups [149], and micro-cantilevers with either metal or polymer coatings operated at low or high temperatures whose stress-induced deflection provides a measure of target analyte concentrations [110-113]. Chemiresistors (CR) coated with Au-thiolate monolayer protected nanoparticles (MPN) [102-108, 150-154] whose resistance is a highly sensitive function of sorbed vapors (Figure 1-5), have also been reported to provide low detection limits to TNT vapors, when using a fluoro-alcohol derivate thiolate as a ligand [154]. Although each of these sensor technologies has merit, further work is needed to integrate them into fully autonomous portable explosive detection systems.

In the last decade, there was an increase use of sensors as GC detectors, including surface SAW sensors [2,10,11,13,30], metal oxide sensors [12], and chemiresistors arrays. In particular CR arrays coated with MPNs as a sensing film have been used widely as a detector for portable and micro GC systems [3,9,28,29]. Among the distinguishing features of the MPN-coated CR sensor is the dependence of vapor absorption into the film to create a resistance change, this feature allows for miniaturization of the CR sensor without loss of sensitivity. In addition, the selectivity of the MPN-coated CR can be tuned for a specific target compound through the functional groups of the organic thiolate on the gold nanoparticle. If an array is used, CRs can be coated with several MPNs with different functional groups. The interaction of a VOC with the different MPNs films will create a specific response profile unique for the compound based on the interactions with the several functional groups of the MPNs. This approach, coupled with a pattern-recognition analysis constitutes an effective method to enhance the selectivity of the sensor array as a detector.

The use of CR arrays as GC detectors, however, raise other factors for an optimize sensor response. Kinect factors, for example, must be considered. Since the bands eluting from the separation column have a finite residence time in the detector cell, the flow rate at which the compounds pass through the detector cell is an important factor to optimize for an adequate response. Previous work with CR arrays as GC detector has shown the effect of flow rate on peak width, peak height and peak area for compounds detected using an MPN-coated sensor [28,100]. Temperature is another factor that has an effect on the CR sensor response. As shown in previous work [100], an increase in the CR temperature would result in reduce absorption, decreasing the sensitivity, however, temperature also increases the kinetic energy of the molecules. This behavior has an effect on the diffusion rate of the vapors, which will more easily permeate into the films, decreasing the eluting band of the vapors inside the finite detector cell. These effects reduce the peak width of the eluting compounds, increasing the chromatographic resolution.

1.2.6. Comprehensive two-dimensional gas chromatography

Although the scaling laws related to GC systems generally favor miniaturization, including low dead volume and narrower columns, two factors must be sacrificed due to inherent limitations on the column length: Resolution (R_s), and peak capacity (n_p). Resolution is defined as $2*(t_{R2} - t_{R1})/(w_1 + w_2)$, where t_{R2} and t_{R1} are the retention times of adjacent compounds, and w_1 and w_2 are the base peak widths of the adjacent peaks. Peak capacity (n_p) is defined by the equation $n_p = 1 + N^{1/2}/(4R_s)\ln(t_{Rn}/t_M)$, where N is the number of theoretical plates, t_M is the unretained time of methane, and t_{Rn} is retention time of the last retained peak. One approach to increasing resolution (and sensitivity) entails the use of comprehensive two-dimensional gas chromatography

(GC×GC), in which two columns having stationary phases with different retention properties are coupled in series through a junction-point modulator [155-157].

In a comprehensive GC×GC instrument, the effluent from a first-dimension GC column (^{1}D) is transferred and re-injected using a modulator with a series of repetitive, fast separations in the second dimension column (^{2}D). The modulator is the key piece that couples the two separation columns. Samples are injected at the inlet of the ^{1}D column, where they undergo separation, then, by means of the modulator, are diverted to the ^{2}D column, where analytes undergo an additional separation. The exhaustive transfer of a primary dimension eluting peak into the secondary column can be achieved with an appropriate modulation time, which is the time employed for sampling (trapping and releasing) ^{1}D peaks. The modulator time, being in the order of a few seconds, is generally not sufficient to transfer an entire peak coming from the 1D column, but slices of it, generating a series of ^{2}D retention times. This separation mechanism, supported by the orthogonality of the separation columns generates the GC×GC chromatogram (Figure 1-6).

The most important attributes of GC×GC are the increases in resolution and sensitivity (only with thermal modulation) afforded by re-injecting at the modulator and compound classification based on the presence of clusters in the GC×GC chromatogram. Peak capacity of GC×GC systems, normally estimated as the product of individual peak capacities of the 1st and 2nd dimension column, can also be more than an order of magnitude larger than that of optimal 1-D GC, but only under ideal conditions, currently not achievable by commercial GC×GC systems [158].

The first GC×GC system was reported over 20 years ago, when Philips *et. al.* developed the first GC×GC modulator [159]. The modulator consisted of a segment of a fused-silica capillary coated with a conductive gold paint coupled to a 21-m long, 0.25-µm i.d. polyethylene glycol

capillary column, and a 0.1-m long, 100-µm i.d. PDMS capillary column. It was resistively heated to temperatures above the GC oven temperature to re-inject analytes from the ^{1}D to the ^{2}D column. This design was only adequate for semi-volatile organic compounds that could be trapped in the modulator at room temperature. Sample loss due to breakthrough was also a problem. When trapped effluent was remobilized, any analyte entering the modulator would not be trapped. A more efficient dual-stage modulator was subsequently designed to minimize sample loss [160-161]. In a two-stage modulator, components that are trapped in the primary stage are released into the second stage by a heating pulse sent to the primary stage. The second stage is not heated until the primary stage has cooled to a temperature sufficient for trapping upcoming components. This alternating heating and cooling of each stage results in a more efficient quantitative performance. Full-widths-at-half-maximum (fwhm) on the order of 140 ms were obtained for the modulated peaks, with this modulator [161].

An improvement in resistively-heated modulators came with the development of the rotating thermal modulator [162]. This modulator operates similarly to the direct resistive heating modulators, but uses a rotating heater block instead of conductive gold paint to heat the fused-silica capillary. This design proved to be more robust and efficient than previous thermal modulators. An important breakthrough in the development of thermal modulators came with cryogenic cooling modulators. Using cryogenics, such as liquid nitrogen, allowed analyte bands to be trapped at temperatures below the oven temperature, reaching temperatures as low as -196 °C [163]. With the use of cryogenics, more volatile compounds could be analyzed. The first cryogenic modulator was designed by Marriot *et. al.* [164-165]. Their longitudinally modulated cryogenic system (LCMS), consisted of a liquid CO_2-cooled chamber that moved back and forth between two positions along the end of the ^{1}D column. The columns used in the LCMS GC×GC system

were a non-polar 25-m long, 250-µm i.d. 5% phenylmethylsiloxane capillary column for the ^{1}D, and a semi-polar 0.6-m long, 100-µm i.d. 14% cyanopropylmethylsiloxane capillary column for the ^{2}D. A complex mixture was analyzed in 150 min with this GC×GC system, but only 29 compounds were identified. Linear velocities were 20.6 cm/s and 200 cm/s for the 1st and 2nd dimensions respectively, and the modulation period, the time between successive first-stage heating events, was 7.2 s. Later on, Ledford *et. al.*, designed a two-stage cryogenic modulator that consists of two cold CO_2 jets and two hot air jets [166]. This design was made commercially available through the LECO Corporation, which replaced the CO_2 jets with liquid nitrogen-cooled gas jets [163]. In the last past decade, several other single- and dual- stage cryogenic modulators were developed, and most commercial GC×GC systems today rely upon cryogenic modulation [167-175].

In an attempt to develop consumable-free thermal modulators, Sacks *et. al.* developed air-cooled thermal modulators that use a conventional refrigeration unit to provide cold air to the modulator [176-178]. The capillaries are resistively heat for remobilization of the analytes. This GC×GC system greatly reduces resource requirements relative to systems requiring cryogenic materials; however, the refrigeration unit cools the modulator to only about – 20 °C, limiting the number of high boiling compounds that can be effectively trapped in the modulator.

In recent years, new types of modulators, based on valve operation have received significant attention. In this type of modulation, the transferred band is not compressed. Instead sample is injected to the second column at a relatively high frequency, with bandwidth as small as 10 ms [179]. The main advantages of valve-base modulators are the low cost of operation (no use of consumables) and ease of adapting to conventional GC instruments. The first valve-based modulator was developed by Synovec *et. al.* [179]. It consisted of a 6-port diaphragm valve with

two set positions, sampling and venting mode. In sampling mode, the sample from the primary column enters the secondary column; during venting, the sample is split into the secondary column and a venting port. An auxiliary make-up gas is supplied to the secondary column increasing the linear velocity. This procedure would unfortunately vent 80-90% of the sample, which ultimately decreased sensitivity. In addition, the upper operational temperature limit of the valve was rather low, which made the analysis of semi-volatile compounds practically impossible. Seeley *et. al.* [180] later developed a pneumatic modulation technique, called differential flow modulation, which adds a sample loop to the 6-port valve, modifying the configuration previously designed by Synovec *et. al.*. The sample coming from the primary column fills the sample loop, then, upon switching the valve, an auxiliary make-up gas compresses the sample collected in the loop before injecting it into the second column. With this valve system, approximately 80% of the primary column effluent would enter the seconday column. The key to this method is the relative flow rates of carrier gas in each column (e.g., 0.75 and 15 mL/min, respectively). Recently, Seeley *et. al.* also developed a pneumatic modulator based on a Dean's switch [181]. This modulator solved the problem of the low temperature limit of the diaphragm valves by using two sample loops and a pneumatic switch operated outside the GC oven. The main disadvantage of this modulator is its low duty cycle which only permits a small portion of the primary column effluent to be re-injected. Despite this, the modulator is used in many commercial GC×GC chromatographs [182-183].

Although not yet available as a portable direct-reading instrument, the increases in sensitivity afforded by focusing at the midpoint and the increase in peak capacity and resolution afforded by use of two complementary stationary phases for separation, make GC×GC an attractive technique for the analysis of complex (S)VOC mixtures. Barriers to portability include the need for cryogenic fluids and high power for heating the thermal modulator, or the need of

multiple bulky valves to create a pneumatic modulator. Recently Kurabayashi *et. al.* described the fabrication, design and performance of a low-power two-stage microfabricated thermal modulator (μTM, Figure 1-7) [97,98]. The μTM measures 13 mm (l) × 6 mm (w) × 0.5 mm (h) and consists of two interconnected serpentine etched-Si microchannels suspended from a thin Pyrex cap and wall-coated with PDMS. The μTM is mounted within a few microns of a thermoelectric cooler that can cool the stages up to – 35 °C to focus eluting analytes from the primary column. It was heated to 210 °C with a rate as high as 2400 °C/s and cooled at rates as high as -168 °C/s. The μTM was tested for performance, connected to a primary column and the outlet connected directly to an FID. Under those conditions, the μTM was able to generate fwhm as low as low as 70 ms, and peak amplitude enhancement (PAE) of up to 50, for a set of n-alkanes with vapor pressures spanning a ~ 100-fold range [98]. This dissertation will take this work a step further, and GC×GC chromatograms will be generated by coupling the μTM to short capillary columns in anticipation of using microfabricated columns to assemble a μGC×μGC system, which result in fast separations even for the moderately complex mixtures tested.

As described in this introduction, several efforts have been mounted describing the characterization, testing and fundamental aspects of MEMS analytical components and μGC subsystems, with only a few efforts reporting fully assembled MEMS-based μGCs. This dissertation discusses the results of the development of such a μGC for a specific application: the fast analysis of explosive markers at trace concentrations. The development of the μGC includes some component-level characterization (Chapters 2 and 3), as well as sub-system and system characterization (Chapters 3 and 4). In addition, Chapter 5 discusses the efforts towards the fabrication of the first μGC×μGC system with a μTM, by assembling a sub-system consisting of the μTM connected to fused-silica capillary columns. This research comprises significant progress

towards the development of MEMS analytical systems for use as portable direct-reading air monitoring instrumentation.

1.3. References

1. S.C. Terry, J.H. Jerman, J.B. Angell, *IEEE Trans. Electron Devices*., 1979, 26, 1880-1886.
2. Canary-Three, Defiant Technologies, available at http://www.defiant-tech.com/ canarythree.php, accessed August 2012.
3. S. K. Kim, D. R. Burris, H. Chang, J. Bryant-Genevier, E. T. Zellers, *Environ. Sci. Technol.*, 2012, 46, 6065-6072.
4. S. K. Kim, D. R. Burris, H. Chang, J. Bryant-Genevier, K. A. Gorder, E. M. Dettenmaier, E. T. Zellers, *Environ. Sci. Technol.*, 2012, 46, 6073-6080.
5. S. K. Kim, H. Chang, E. T. Zellers, *Anal. Chem.*, 2011, 83, 7198-7206.
6. S. K. Kim, H. Chang, J. G. Bryant, D. R. Burris, and E. T. Zellers, *Proc. Transducers 11'*, Beijing, China, June 5-9, pp. 799-802.
7. E. T. Zellers, G. Serrano, H. Chang, and L. K. Amos, *Proc. Transducers 11'*, Beijing, China, June 5-9, pp. 2082-2085.
8. H. Chang, S. K. Kim, T. Sukaew, F. Bohrer, E. T. *Zellers, Solid-State Sens. Actuators and Microsyst. Workshop*: Hilton Head, SC, June 6-10 2010, pp 278-281.
9. E. T. Zellers, S. Reidy, R. A. Veeneman, R. Gordenker, W. H. Steinecker, G. R. Lambertus, H. Kim, J. A. Potkay, M. P. Rowe, Q. Zhong, C. Avery, H. K. L. Chan, R. D. Sacks, K. Najafi, K. D. Wise. *Proc. Transducers 07'*, Lyon, France, June 10-14 2007, pp. 1491-1491.
10. C. J. Lu, W. Steineker, W. C. Tian, M. Oborny, J. Nichols, M. Agah, J. Potkay, H. Chang, J. Driscoll, R. Sacks, K. Wise, S. Pang, E. T. Zellers, *Lab Chip*, 2005, 5, 1123-1131.
11. R. P. Manginell, J. M. Bauer, M. W. Moorman, L. J. Sanchez, J. M. Anderson, J. J. Whiting, D. A. Porter, D. Copic, K. E. Achyuthan, *Sensors*, 2011, 11, 6517-6532.
12. S. Zampolli, I. Elmi, F. Mancarella, P. Betti, E. Dalcanale, G. C. Cardinali, M. Severi, *Sens. Actuators B*, 2009, 141, 322-328.
13. P. R. Lewis, R. P. Manginell, D. R. Adkins, R. J. Kottenstette, D. Wheeler, S. Sokolowski, D. E. Trudell, J. Bymes, M. Okandan, J. M. Bauer, R. G. Manley, G. C. Frye-Mason, *IEEE Sensors J.*, 2006, 6, 784-795.
14. C2V-200 Micro-GC, Thermo Scientific, http://www. thermo scientific .com / ecomm/servlet/ productsdetail_11152_L11169_80571_13474379_-1, accessed August 2012.
15. EnCal 3000 Micro-GC,Elster GmbH, www.elster-instromet.com/en/micro GC technology .html, accessed August 2012.
16. WIMSS Center, available at www.wimserc.org, accessed August 2012.

17. G. Serrano, D. Paul, S- J. Kim, K. Kurabayashi, E. T. Zellers, *Anal. Chem*., 2012, 84, 6973-6980.
18. C. Coffey, T. Pearce, R. Lawrence, J. Hudnall, J. Slaven, S. Martin, *JOEH*, 2009, 6, 1-8
19. T. Tarumi, G. W. Small, R. J. Combs, R. T. Kroutil. *Vib. Spectrosc.*, 2005, 37, 39-52.
20. L. Gao, A. Sugiarto, J. D. Harper, R. G. Cooks, Z. Ouyang. *Anal. Chem.*, 2008, 80, 7198-7205.
21. Keil, H. Hernandez-Soto, R.J. Noll, M. Fico, L. Gao, Z. Ouyang, and R.G. Cooks, *Anal. Chem.*, 2008, 80, 734-741.
22. C. C. Mulligan, D. R. Justes, R. J. Noll, N. L. Sanders, B. C. Laughlin, R. G. Cooks, *Analyst*, 2006, 131, 556-567.
23. I. Cotte-Rodriguez, R. G. Cooks, *Chem. Comm*., 2006, 2006, 2968-2970.
24. G. M. Huang, W. Xu, M. A. Visbal-Onufrak, Z. Ouyang, R. G. Cooks, *Analyst*, 2010, 135, 705-711.
25. J. Syage, *J. Am. Soc. Mass. Spectrom*, 2001, 12, 648-655.
26. W. Schröoder, G. Matz, J. Kubler, *Field Anal. Chem. Tech.*, 1998, 2, 287-297.
27. L. K. Whalley, A. C. Lewis, J. B. McQuaid, R. M. Purvis, J. D. Lee, K. Stemmler, C. Zellweger, P. Ridgeon, *J. Environ. Monit*., 2004, 6, 234-241.
28. Q. Zhong, W. H. Steinecker, E. T. Zellers, *Analyst*, 2009, 134, 283-293.
29. Q. Zhong, R. A. Veeneman, W. H. Steinecker, C. Jia, S. A. Batterman, E. T. Zellers, *J. Environ. Monit.*, 2007, 9, 440-448.
30. C. -J. Lu, C. Jin, E. T. Zellers, *J. Environ. Monit.*, 2006, 8, 270-278.
31. C.-J. Lu, J. Whiting, R. D. Sacks, E. T. Zellers, *Anal. Chem*., 2003, 75, 1400-1409.
32. J. Stapes, S. Viswanathan, *IEEE Sensors Journal*, 2005, 5, 622-630.
33. MIRAN SapphIRe, Thermo Scientific, http://www.thermoscientific.com/ ecomm/servlet/productsdetail_11152___11961316_-1, accessed November 2012.
34. DX 4015, Gasmet, http://www.gasmet-usa.com/images/Dx4015.pdf, accessed April 2012.
35. HazMatID360, Smiths Detection, http://www.smithsdetection.com/hazmatid360.php, accessed April 2012.
36. SABRE 4000, Smiths Detection, http://www.smithsdetection.com/SABRE_4000.php, accessed April 2012.
37. IMS-Mini 200, GmbH, http://www.iut-berlin.info/7.0.html?&L=1, accessed April 2012.
38. MobileTrace Safran, Morpho, http://www.morpho.com/I MG/ pdf/ MDI_Mobile Trace_Explosives_DAT.pdf, accessed April 2012.
39. Griffin 460, FLIR, http://gs.flir.com/ products/ icx-detection/chemical/griffin-460/, accessed April 2012.
40. Hapsite ER, INFICON, http://www.inficon emergency response.com/ en/hapsite_er// index.html, accessed April 2012.
41. TRIDION-9, Torion, http://www.torion.com/products/24, accessed April 2012.
42. Guardion, Smiths Detection, http://www.smithsdetection.com/GUARDION.php, accessed April 2012.
43. 490 Micro-GC, Agilent Technologies, http://www. chem.agilent.com /en-US/Products/ Instruments/gc/microgc/pages/default.aspx, accessed April 2012.

44. DL-102 PID analyzer, HNU, http://www.hnu.com/index.php?view= Portable&cmd= 102, accessed August 2012.
45. VOC-Analyzer 200, GmbH, http://www.iut-berlin.info/181.0.html?&L=1, accessed April 2012.
46. Cyranose 320, Smiths Detection, http://www.smithsdetection.com/history_cyrano.php, accessed April 2012.
47. S. DiNardi, The Occupational Environment: Its Evaluation, Control, and Management, Chapter 15, 2nd edition, AIHA press, 2003.
48. M. D. Hsieh, E. T. Zellers, *Anal. Chem*., 2004, 76, 1885-1895.
49. L. Thiesan, D. Hannum, D. W. Murray, J. E. Parmeter, Survey of commercial available explosives detection technologies and equipment, available at https://ncjrs.gov/pdffiles1/ nij/grants/208, accessed April 2012.
50. D. S. Moore, *Rev. Sci. Instrum.*, 2004, 75, 2499 – 2513.
51. J. Yinon, *Trac-Trends Anal. Chem*., 2002, 21, 292-301.
52. K. L. Linker, F. J. Conrad, C. A. Custer, C. L. Rhykerd Jr., Sandia National Laboratories, Particle Preconcentrator, U.S. Pat. 6,085,601, 2000.
53. R. Ingram, J. Sikes, *Proc. SPIE*, 7664, (2010), 766415-1 – 766415-8.
54. K. Cizek, C. Prior, C. Thammakhet, M. Galik, K. Linker, R. Tsui, A. Cagan, J. Wake, J. La Belle, J. Wang, *Anal. Chim. Acta*, 661, (2010), 117-121.
55. M. Joshi, K. Rigsby, J. R. Almirall, *J. Forensic Sci.*, 208, (2011), 29-36.
56. I. Voiculescu, R. A. McGill, M. E. Zaghloul, J. Stepnowski, S. Stepnowski, H. Summers, V. Nguyen, S. Ross, K. Walsh, M. Marin, *IEEE Sensors*, 6, (2006), 1094-1104.
57. M. Martin, M. Crain, K. Walsh, R. A. McGill, E. Houser, J. Stepnowski, S. Stepnowski, H-D Wu, S. Ross, *Sens. Actuators B*, 126, (2007), 447-454.
58. E. H. M. Camara, P. Breuil, D. Briand, N. F. de Rooij, C. Pijolat, *Anal. Chim. Acta*, 688, (2011), 175-182.
59. E. Wapelhorts, J-P. Hauschild, J. Muller, *Sens. Actuators. A*, 2007, 138, 22-27.
60. R.A. Miller, E.G. Nazarov, G.A. Eiceman, A. T. King, *Sens. Actuators. A,* 2001, 91, 301-312.
61. S. –S. Kim, C. Young, B. Mizaikoff, *Anal. Bioanal. Chem*., 2008, 390, 231-238.
62. T. Sandner, A. Kenda, C. Drabe, H. Schenk, W. Scherf, *Proc. of SPIE*, 2007, 6466, 46602.
63. K. Yu, D. Lee, U. Krishnamoorthy, N. Park, O. Solgaard, *Sens. Actuators A: Physical*, 2006, 130, 523-530.
64. H. Kim, A. Astle, K. Najafi, L. P. Bernal, P. D. Washabaugh, *IEEE MEMS*: Kobe, Japan, January 21-25, 2007; pp. 131-134.
65. J. H. Seo, S. K. Kim, E. T. Zellers, K. Kurabayashi, *Lab Chip*, 2012, 12, 717-724.
66. T. Sukaew, H. Chang, G. Serrano, E. T. Zellers, *Analyst,* 2011, 136, 1664-1674.
67. B. Alfeeli, M. Agah, *IEEE Sensors J*. 2011, 11, 2756-2762.
    B. Alfeeli, L. T. Taylor, M. Agah, *J. Microelectromech S.*, 2010, 95, 259-267.
68. R. P. Manginell, D. R. Akins, M. W. Moorman, R. Hadizadeh, D. Copic, D. A. Porter, J. M. Anderson, V. M. Hietala, J. R. Bryan, D. R. Wheeler, K. B. Pfeifer, A. Rumpf, *J. Microelectromech S*, 2008, 17, 1396-1407.
69. B. Alfeeli, D. Cho, M. Ashraf-Khorassani, L. T. Taylor, M. Agah, MEMS-based multi-inlet/outlet preconcentrator coated by inkjet printing of polymer adsorbents, *Sens. Actuators B*, 2008, 133, 24-32.

70. B. Alfeeli, M. Agah, *7th IEEE Sensors Conference*, Lecce, Italy October 26-29, 2008, pp. 736-739.
71. R. S. Pai, R. A. McGill, S. V. Stepnowski, J. L. Stepnowski, K. P. Williams, H. Summers, R. Furstenberg, M. T. Rake, V. K. Nguyen, D. L. Simonson, B. Higgins, C. Kendziora, E. J. Houser, *Transducers ' 07, Lyon, France*, June 2007, U1154-U1155.
72. W. C. Tian, H. K. L. Chan, C. J. Lu, S. W. Pang, E. T. Zellers, *J. Microelectromech. S.*, 2005, 14, 498-507.
73. M. Kim, S. Mitra, *J. Chromatography A*, 2003, 996, 1-11.
74. W. -C. Tian, S. W. Pang, C.-J. Lu, E. T. Zellers, *J. Microelectromech. S.*, 2003, 12, 264-272.
75. W. C. Tian, H. K. L. Chan, S. W. Pang, C. J. Lu, E. T. Zellers, *Transducers '03*, Boston, MA, June 2003, pp 31-34.
76. R. P. Manginell, G. C. Frye-Mason, R. J. Kottenstette, P. R. Lewis, and C. C. Wong, *Solid State Sensor and Actuator Workshop*: Hilton Head, SC, June 2000, pp. 179-182.
77. A. D. Radadia, A. Salehi-Khokin, R. I. Masel, M. A. Shannon, *Sens. Actuators B*, 2010, 150, 456-464.
78. M. A. Zareian-Jahromi, M. Agah, *J. Microelectromech S.*, 2010, 19, 294-304.
79. A. D. Radadia, R. D. Morgan, R. I. Masel, M. A. Shannon, *Anal. Chem*., 2009, 81, 3471-3477.
80. M. A. Zarejan-Jahromi, M. Ashraf-Khorassani, L. T. Taylor, M. Agah, *J. Microelectromech S.*, 2009, 18, 28-37.
81. G. Serrano, S. M. Reidy, E. T. Zellers, *Sens. Actuators. B*., 2009, 141, 217-226.
82. A.D. Radadia, R.I. Masel, M.A. Shannon, J.P. Jerrell, and K.R. Cadwallader, *Anal. Chem*., 2008, 80, 4087- 4094.
83. G. Serrano, S. Reidy, K. D. Wise, and E. T. Zellers, *Proc. Solid-State Sensor, Actuator, and Microsystems Workshop*; Transducers Research Foundation, Inc., Hilton Head, SC, June 2008, pp. 260–263.
84. S. Reidy, D. George, M. Agah, R. Sacks, *Anal. Chem*., 2007, 79, 2911-2917.
85. J.A. Potkay, G.R. Lambertus, R.D. Sacks, K.D. Wise, *J. Microelectromech S.,* 2007, 16, 1071-1079.
86. S. Reidy, G. Lambertus, J. Reece, R. Sacks, *Anal. Chem*., 2006, 78, 2623-2630.
87. J.B. Sanchez, F. Berger, M. Fromm, M-H. Nadal, *Sens. Actuators B*, 2006, 119, 227-233.
88. M. Agah, J. A. Potkay, G. R. Lambertus, R. D. Sacks, K. D. Wise, *J. Microelectromech S.*, 2005, 14, 1039-1050.
89. G. Lambertus, R. Sacks, *Anal. Chem*., 2005, 77, 2078-2084.
90. S. Zampolli, I. Elmi, J. Sturmann, S. Nicoletti, L. Dori, G.C. Cardinali, *Sens. Actuators B*, 2005, 105, 400-406.
91. G.R. Lambertus, A. Elstro, K. Sensening, J. Potkay, M. Agah, S. Scheuering, K.D. Wise, F. Dorman, R.D. Sacks, *Anal. Chem.,* 2004, 76, 2629-2637.
92. M. Agah, J. Potkay, A. Elstro, G. Lambertus, R. Sacks. K.D. Wise, *Tech. Digest, North American Solid-State Sensors, Actuators, and Microsystems Workshop,* Hilton Head, SC, USA, June 6-10, 2004.
93. M. Agah, J.A. Potkay, J.A. Driscoll, R.D. Sacks, M. Kaviany, K.D. Wise, Thermal behavior of high-performance temperature-programmed microfabricated gas chromatography columns, *Proc. Transducers '03*, USA June 8-12, 2003.
94. G. M. Gross, J. W. Grate, R. E. Synovec, *J. Chrom. A*, 2004, 1060, 225-236.

95. D. Paul, G. Serrano, E. T. Zellers, K. Kurabayashi, *Proc. MEMS '12*, Paris, France, Jan 29 - Feb 2, pp. 96-99.
96. S.-J. Kim, G. Serrano, K. D. Wise, K. Kurabayashi, and E. T. Zellers, *Anal. Chem.*, 2011, 83, 5556-5562.
97. S.-J. Kim, S. M. Reidy, B. P. Block, K. D. Wise, E. T. Zellers, and K. Kurabayashi, *Lab Chip*, 2010, 10, 1647-1654.
98. J. J. Whiting, C. S. Fix, J. M. Anderson, A. W. Staton, R. P. Manginell, D. R. Wheeler, E. B. Myers, M. L. Roukes, R. J. Simonson, *Proc. Transducers '09*, Denver, Colorado, USA, June 21-25, 2009.
99. R. S. Jian, R. X. Huang, C. -J. Lu, *Talanta*, 2012, 88, 160-167.
100. K. Scholten, X. Fan, E. T. Zellers, *Appl. Phy. Letters*, 2011, 99, 141108
101. F. I. Bohrer, E. Covington, C. Kurdak, E. T. Zellers, *Anal. Chem*., 2011, 83, 3687-3695.
102. M. Li, E. B. Myers, H. X. Tang, S. J. Aldridge, H. C. McCaig, J. J. Whiting, R. J. Simonson, N. S. Lewis, M. L. Roukes, *Nano Letters*, 2010, 10, 3899-3903.
103. D. J. Rairigh, G. A. Warnell, C. Xu, E. T. Zellers, A. J. Mason, *IEEE Trans Biomed. Circuits Syst.*, 2009, 3, 267-276.
104. C. Jin, E. T. Zellers, *Sens. Actuators B*, 2009, 139, 548-556.
105. C. Jin, E. T. Zellers, *Anal. Chem*., 2008, 80, 7283-7293.
106. C. Jin, P. Kurzawski, A. Hierlemann, E. T. Zellers, *Anal. Chem*., 2008, 80, 227-236.
107. W. H. Steinecker, M. P. Rowe, E. T. Zellers, *Anal. Chem.*, 2007, 79, 4977-4986.
108. R. Archibald, P. Datskos, G. Devault, V. Lamberti, N. Lavrik, D. Noid, M. Sepaniak, P. Dutta, *Anal. Chim. Acta*, 2007, 584, 101-105.
109. L. A. Pinnaduwage, A. Wig, D. L. Hedden, A. Gehl, D. Yi, T. Thundat, R. T. Lareau, *J. Appl. Phys*., 2004, 95, 5871-5875.
111. L. A. Pinnaduwage, T. Thundat, J. E. Hawk, D. L. Hedden, R. Britt, E. J. Houser, S. Stepnowski, R. A. McGill, D. Bubb, *Sens. Actuators B,* 2004, 99, 223-229.
112. L. A. Pinnaduwage, D. Yi, F. Tian, T. Thundat, R. T. Lareau, *Langmuir*, 2004, 20, 2690-2694.
113. L. A. Pinnaduwage, A. Gehl, D. L. Hedden, Muralidharan G, T. Thundat, R. T. Lareau, T. Sulchek, L. Manning, B. Rogers, M. Jones, J. D. Adams, *Nature*, 2003, 425, 474-474.
114. W. H. Steinecker, M. P. Rowe, A. J. Matzger, E. T. Zellers, Chemiresistor array with nanocluster interfaces as a micro-GC detector, *Transducers '03*, Boston, MA, June 8-12, 2003, IEEE, Boston, pp. 1343-1346.
115. Q. Y. Cai, E. T. Zellers, *Anal. Chem*., 2002, 74, 3533-3539.
116. A. W. Snow, H. Wohltjen, U.S. Patent 6, 221, 673, April 24, 2001.
117. H. Wohltjen, A. W. Snow, *Anal. Chem*., 1998, 70, 2856-2859.
118. A. W. Snow, H. Wohltjen, *Chem. Matls*., 1998, 10, 947-949.
119. E.T. Zellers, S.K. Kim, G. Serrano, H. Chang, F. Bohrer, R. Veeneman, E. Covington, C. Kurdak, *Tech. Digest, 215th Electrochemical Society Meeting*, San Francisco, California, USA, May 24-29, 2009.
120. G. Serrano, H. Chang, E. T. Zellers, *Proc. Transducers 09'*, Denver, Co, USA, June 2009, pp. 1654-1657.
121. S.K. Kim, H. Chang, E.T. Zellers, *Proc. Transducers 09'*, Denver, Colorado, USA, June 21-25, 2009, pp. 719-723.
122. G.R. Lambertus, C.S. Fix, S.M. Reidy, R. Miller, D. Wheeler, E. Nazarov, R.D. Sacks, *Anal. Chem*., 2005, 77, 7563-7571.

123. G. L. Hook, C. J. Lepage, S. I. Miller, P. A. Smith, *J. Sep. Sci.*, 2004, 27, 1017-1022.
124. M. Joshi, K. Rigsby, J. R. Almirall, *J. Forensic Sci.*, 2011, 208, 29-36.
125. K. Song, S-K. Lee, *Sensors Actuators B*, 2007, 125, 173-179.
126. J. J. Whiting, R. D. Sacks, *J. Sep. Sci.*, 2006, 29, 218-227.
127. S. M. Cho, Y. J. Kim, G. S. Heo, S-M. Shin, *Sens. Actuators B*, 2006, 117, 50-57.
128. S. Kendler, A. Zifman, N. Gratziany, A. Zaltsman, G. Frishman, *Anal. Chim. Acta*, 2005, 548, 58-65.
129. J. M. Sanchez, R. D. Sacks, *J. Sep. Sci.*, 2005, 28, 22-30.
130. J. M. Sanchez, R. D. Sacks, *Anal. Chem.*, 2003, 75, 978-985.
131. F. Bender, N. Barie, G. Romoudis, A. Voigt, M. Rapp, *Sens. Actuators B*, 2003, 93, 135-141.
132. C. J. Lu, E. T. Zellers, *Analyst*, 2002, 127, 1061-1068.
133. C. J. Lu, E. T. Zellers, *Anal. Chem.*, 2001, 73, 3449-3457.
134. A. R. Mastrogiacomo, E. Pierini, L. Sampaolo, *Chromatographia*, 1995, 41, 599-604.
135. A. Wheeler, A. J. Robell, *J. Catalyst*, 1969, 13, 299-305.
136. G. Berton, F. Bruner, A. Liberti, C. Perrino, *J. Chrom.*, 1981, 203, 263-270.
137. J. E. Bunch, E. D. Pellizzari, *J. Chrom.,* 1979, 186, 811-829.
138. X-L Cao, C. N. Hewitt, *Chemosphere*, 1993, 27, 695-705.
139. T. Knobloch, W. Engewald, *J. High Res. Chromatog.*, 1995, 18, 635-642.
140. H. Rothweiler, P. A. Wager, C. Schlatter, *Atmospheric Env.*, 1991, 25B, 231-253.
141. J. Namiesnik, E. Kozlowski, *Analytische Chemie*, 1982, 311, 581-584.
142. E. Matisova, S. Skrabakova, *J. Chrom. A*, 1995, 707, 145-179.
143. R. L. Grob, Modern practice of gas chromatography, 3rd Ed., Wiley-Interscience, New York, 2005 (Chapter 2).
144. G. E. Spangler, *J. Microcol. Sep.*, 2001, 13, 285-292.
145. J. S. Yang, T. M. Swager, *J. Am. Chem. Soc*., 1998, 120, 11864-11873.
146. K. J. Albert, D. R. Walt, *Anal. Chem*., 2000, 72, 1947-1955.
147. K. J. Albert, M. L. Myrick, S. B. Brown, D. L. James, F. P. Milanovich, D. R. Walt, *Environ. Sci. Technol*., 2001, 35, 3193-3200.
148. Fido XT, ICx, available at www.icxt.com/uploads/file/products/ brochures/ Fido_XT.pdf, accessed April 2012.
149. G. K. Kannan, A. T. Nimal, U. Mittal, R. D. S. Yadawa, J. C. Kappor, *Sens. Actuators B*, 2004, 101, 328-334.
150. S. D. Evans, S. R. Johnson, Y. L. L. Cheng, T. H. Shen, *J. Mater. Chem*., 2002, 10, 183-188.
151. H. L. Zhang, S. D. Evans, J. R. Henderson, R. E. Miles, T. H. Shen, *Nanotechnology*, 2002, 13, 439-444.
152. L. Han, D. R. Daniel, M. M. Maye, C. J. Zhong, *Anal. Chem*., 2001, 73, 4441-4449.
153. L. Han, X. J. Shi, W. Wu, F. L. Kirk, J. Luo, L. Y. Wang, D. Mott, L. Cousineau, S. Lim, S. Lu, C. J. Zhong, *Sens. Actuators B*, 2005, 106, 431-441.
154. E. J. Houser, T. E. Misna, V. K. Nguyen, R. Chung, R. L. Mowery, R. A. McGill, *Talanta*, 2001, 54, 469-485.
155. J. M. Dimandja, *Anal. Chem.*, 2004, 1004, 167-174.
156. H. J. Cortes, B. Winniford, J. Luong, and M. Pursch, *J.Sep. Sci.*, 2009, 32, 883-904.
157. J. Dalluge, J. Beens, and U. T. Brinkman, *J. Chrom. A*, 2003, 1000, 69-108.
158. L.M. Blumberg, F. David, M. S. Klee, and P. Sandra, *J. Chrom. A*, 2008, 1188, 2-16.

159. Z. Y. Liu, J. B. Philips, *J. Chrom. Sci.*, 1991, 29, 227-231.
160. C. J. Venkatramani, J. B. Philips, *J. Microcol. Sep.*, 1993, 5, 511-516.
161. Z. Y. Liu, S. R. Sirimanne, D. G. Patterson, L. L. Needham, J. B. Phillips, *Anal. Chem.*, 1994, 66, 3086-3092.
162. J. B. Philips, R. B. Gaines, J. Blomberg, F. W. M. Van der Wielen, J. M. Dimandja, V. Green, J. Granger, D. Patterson, L. Racovalis, H. J. de Geus, J. de Boer, P. Haglund, J. Lipsky, V. Sinha, E. B. Ledford, *J. High Res. Chromatogr.*, 1999, 22, 3-10.
163. Pegasus 4D, LECO Corporation, available at http://www.leco.com/products/ sep_sci/ pegasus_4d/Pegasus4D.html, accessed August 2012.
164. R. M. Kinghorn, P. J. Marriott, *J. High Res. Chromatogr.*, 1998, 21, 620-622.
165. R. M. Kinghorn, P. J. Marriott, P. A. Dawes, *J. High Res. Chromatogr.*, 2000, 23, 245-252.
166. E. B. Ledford, C. Billesbach, , *J. High Res. Chromatogr.*, 2000, 23, 202-204.
167. J. Beens, M. Adahchour, R. J. J. Vreuls, K. van Altena, U. A. T. Brinkman, *J. Chrom. A*, 2001, 919, 127-132.
168. M. Adahchour, J. Beens, U. A. T. Brinkman, *Analyst*, 2003, 128, 213-216.
169. R. B. Gaines, G. S. Frysinger, *J. Sep. Sci.*, 2004, 27, 380-388.
170. T. Hyotylainen, M. Kallio, K. Hartonen, M. Jussila, S. Palonen, M. L. Riekkola, *Anal. Chem.*, 2002, 74, 4441-4446.
171. M. Kallio, T. Hyotylainen, M. Jussila, K. Hartonen, S. Palonen, M. Shimmo, M. L. Riekkola, *Anal. Bioanal. Chem.*, 2003, 375, 725-731.
172. M. Kallio, M. Jussila, P. Raimi, T. Hyotylainen, *Anal. Bioanal. Chem.*, 2008, 391, 2357-2363.
173. J. Harynuk, T. Gorecki, *J. Chrom. A*, 2003, 1019, 53-63.
174. M. Moeder, C. Martin, D. Schlosser, J. Harynuk, T. Gorecki, *J. Chrom. A*, 2006, 1107, 233-239.
175. M. Pursch, P. Eckerle, J. Biel, R. Streck, H. Cortes, K. Sun, B. Winniford, *J. Chrom. A*, 2003, 1019, 43-51.
176. M. Libardoni, J. H. Waite, and R. Sacks, *Anal. Chem.*, 2005, 77, 2786-2794.
177. M. Libardoni, P. T. Stevens, J. H. Waite, and R. Sacks, *J. Chrom. B*, 2006, 842, 13-21.
178. M. Libardoni, C. Fix, J. H. Waite, and R. Sacks, *Analytical methods*, 2010, 2, 936-943.
179. C. A. Bruckner, B. J. Prazen, and R. E. Synovec, *Anal. Chem.*, 1998, 70, 2796-2804.
180. J. V. Seeley, F. Kramp, C. Hicks, *Anal. Chem.*, 2000, 72, 4346-4352.
181. J. V. Seeley, N. J. Micyus, S. V. Bandurski, S. K. Seeley, J. D. McCurry, *Anal. Chem.*, 2007, 79, 1840-1847.
182. TRACE GC×GC, Thermo Scientific, available at http://thermoscientific.com/ecomm/ servlet/productsdetail_11152_L10785_80571_11961809_-1, accessed April 2012.
183. Capillary flow technology GC×GC flow modulator, Agilent Technologies, available at http://chem.agilent.com, accessed April 2012.

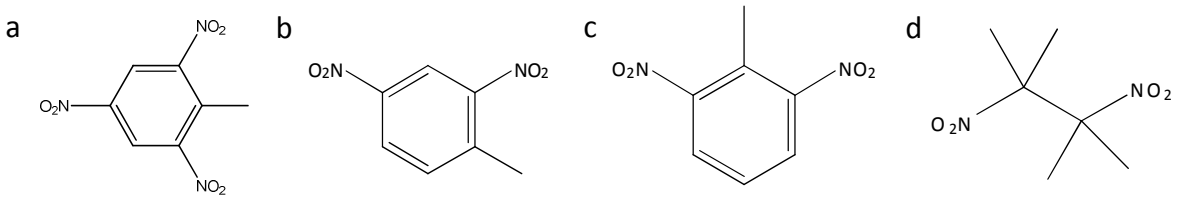

Figure 1-1. (a) 2,3,6-trinitrotoluene (TNT, p_v = 0.006 mtorr), (b) 2,4-dinitrotoluene (2,4-DNT, p_v = 0.5 mtorr), (c) 2,6-dinitrotoluene (2,6-DNT, p_v = 1 mtorr), (d), 2,3-dimethyl,2,3-dinitrobutane (DMNB, p_v = 2 mtorr).

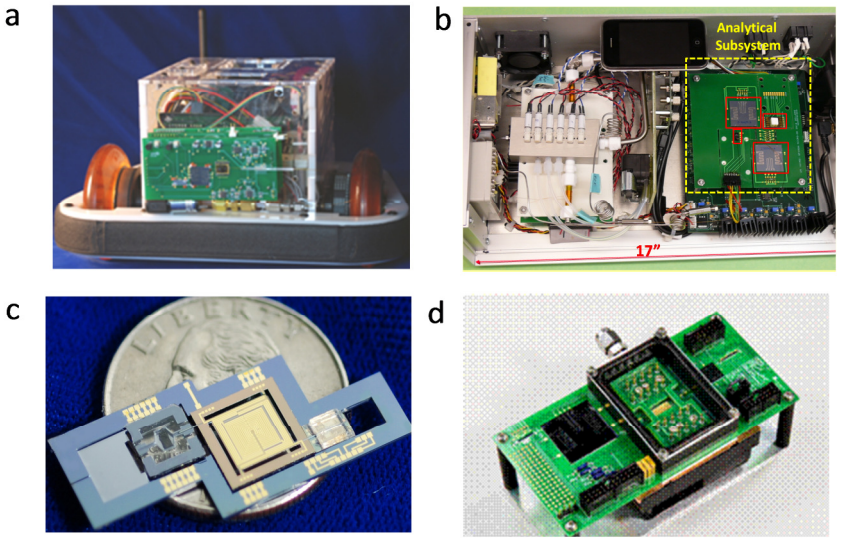

Figure 1-2. WIMS^2 GC prototypes: (a) MERCURY, designed for robot-mounted military surveillance, (b) SPIRON, designed for multiple VOC analysis, (c) ORION (concept), ultra small, low power μGC, (d) MARS, μGC×μGC.

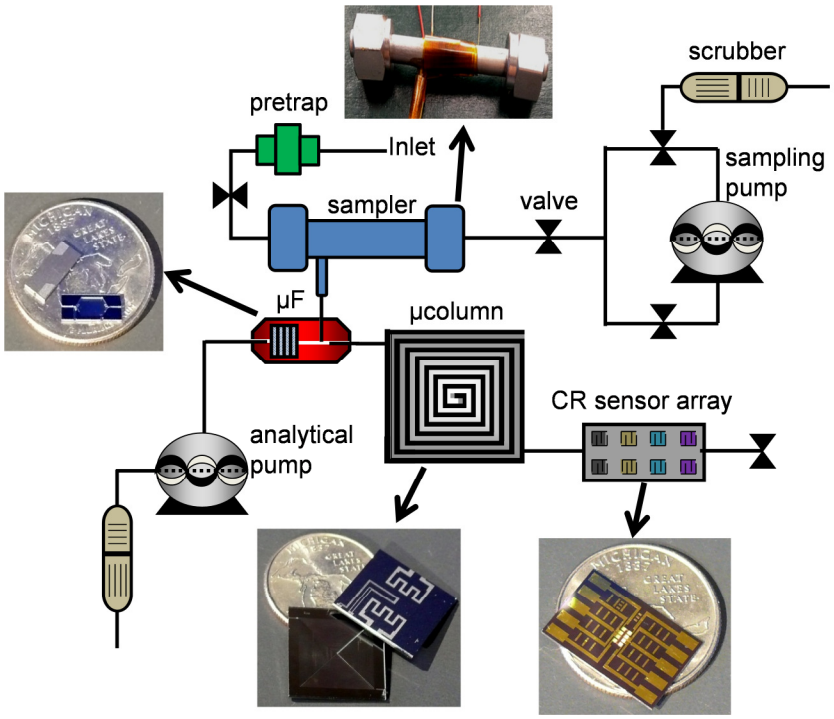

Figure 1-3. Fluidic pathway diagram of the INTREPID-II µGC prototype and photograph of the µGC main components

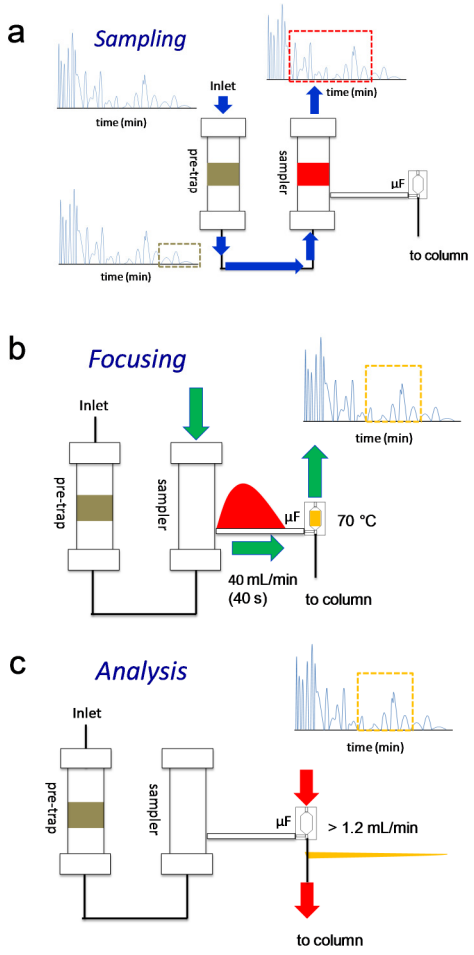

Figure 1-4. The preconcentrator/focuser (PCF) module consists of pre-trap, sampler and microfocuser (µF), and operates in three modes: (a) Sampling, (b) Focusing, and (c) Analysis. In (a) Sampling Mode, the analytes pass through the pre-trap and sampler. As shown in the figure, ideally only certain compounds are trapped on each device, according to the adsorbent material which is retained inside them. In (b) Focusing Mode, sampler is heated and compounds trapped in the sampler are transferred to the µF. Based on the adsorbent material packed in the µF, and operating conditions, selectivity towards the target compounds can be achieved. In (c) Analysis Mode, µF is heated, and compounds are injected into separation column.

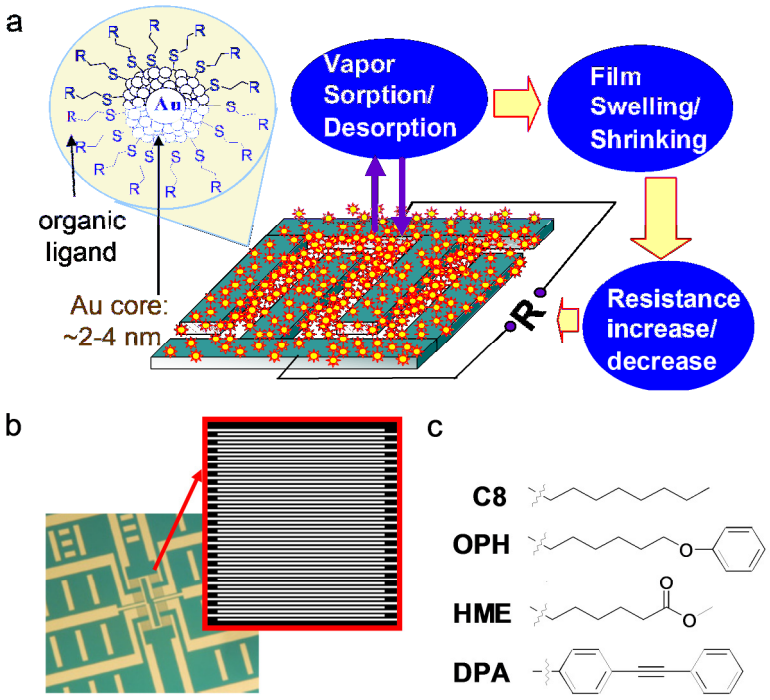

Figure 1-5. (a) Cartoon showing the vapor absorption swelling/shrinking on the MPN film that creates the signal response, (b) picture of an eight chemiresistor sensor array, (c) monolayer protected gold nanoparticles with the different functional groups, used in this dissertation.

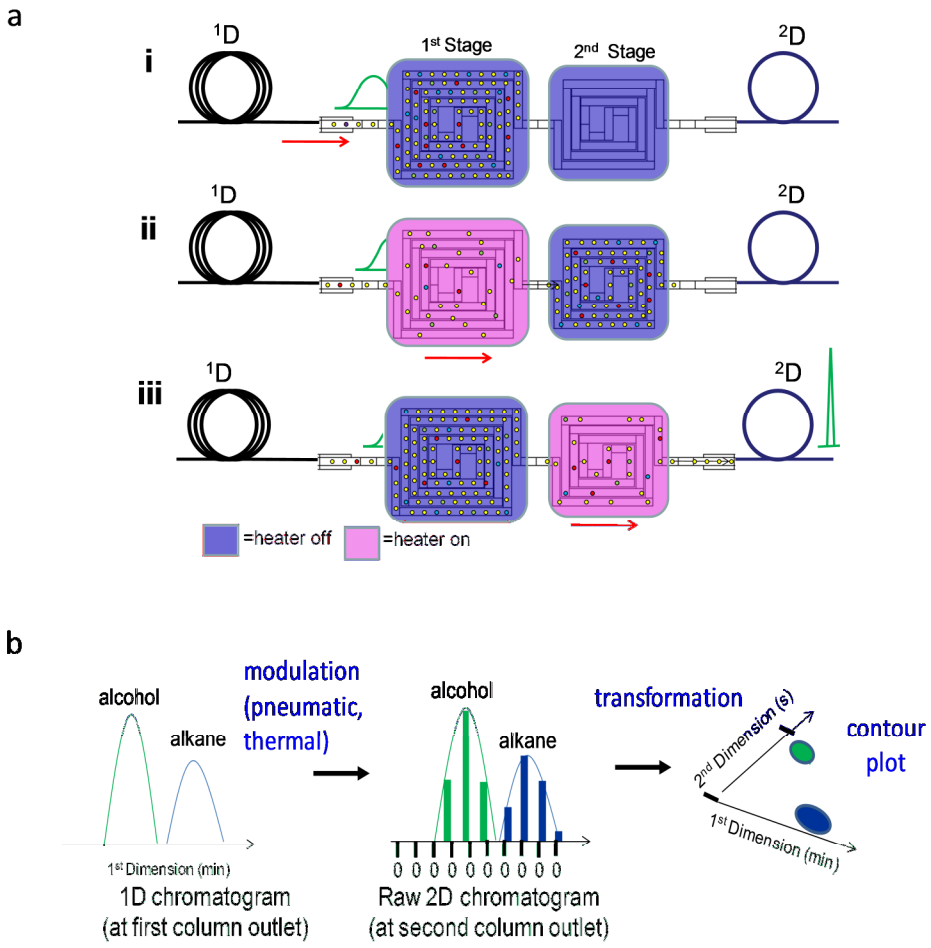

Figure 1-6. Cartoons showing the (a) dual-stage thermal modulator used in this dissertation and (b) the GC×GC separation concept [96].

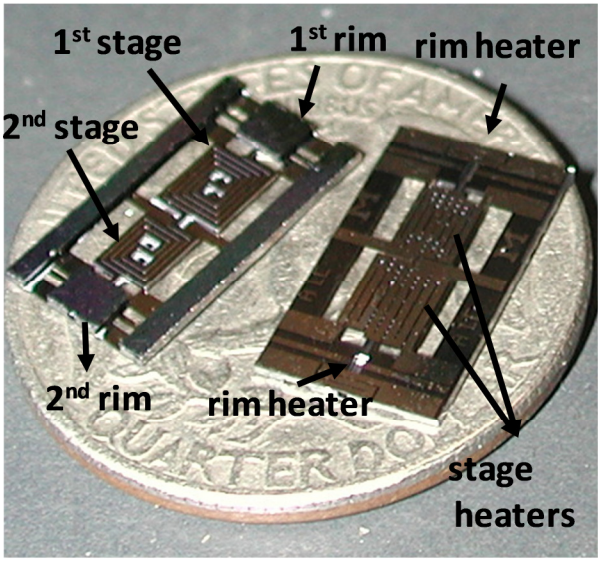

Figure 1-7. Photograph of both sides of the microfabricated two-stage thermal modulator (μTM). Labels identify the essential structural features [17].

CHAPTER II

HYBRID PRECONCENTRATOR/FOCUSER MODULE FOR DETERMINATIONS OF EXPLOSIVE MARKER COMPOUNDS WITH A MICRO-SCALE GAS CHROMATOGRAPH

2.1. Introduction

The need to rapidly and selectively measure trace levels of explosives is a critical component of security measures taken to screen baggage and personnel in airports. The repertoire of detection systems developed or adapted to this application has been reviewed [1,2] and includes a small number of instruments configured for measuring air concentrations of explosives or their marker compounds directly [3-12]. In the absence of specialized inlets, use of these instruments is limited to those explosives with vapor pressures high enough to yield detectable quantities of airborne material.

One common explosive, 2,4,6-trinitrotoluene (TNT), is detectable in the gas phase but its low vapor pressure ($p_v = 8.9 \times 10^{-7}$ kPa) produces a saturation concentration of only ~7 ppb at room temperature. Natural byproducts of TNT production include 2,4- and 2,6-dinitrotoluene (2,4-DNT and 2,6-DNT, respectively), and smaller amounts of other TNT and DNT isomers, which are found as impurities in TNT-containing explosive devices [13]. The vapor concentrations of the two major TNT impurities, 2,4-DNT ($p_v = 5.3 \times 10^{-5}$ kPa) and 2,6-DNT ($p_v = 1.2 \times 10^{-4}$ kPa)

comprise 35% and 4%, respectively, of that of TNT in the headspace of commercial TNT at room temperature [14]. The more volatile 2,3-dimethyl-2,3-dinitrobutane (DMNB, $p_v = 2.7\times 10^{-4}$ kPa) has been designated by the International Civil Aviation Organization (ICAO) as an explosive taggant, and a small quantity of DMNB is added to formulations of many legally manufactured explosive products [15].

Portable instruments employing gas chromatography with mass spectrometric (GC-MS) and ion mobility spectrometric (GC-IMS) detection can provide reliable speciation and low-level detection of explosive marker vapors [11,12], owing largely to the combination of separation and spectral detection. However, GC-MS systems are very expensive and require highly trained operators, and IMS systems are reportedly prone to false positive responses [1]. Thus, there remains a need for portable instrumentation capable of fast and accurate analysis of explosives in the vapor phase, yet small, simple, and inexpensive enough to be used for routine monitoring.

Over the past decade, there have been a few reports on microfabricated gas chromatographic systems (μGC) made from micromachined-Si devices [16-24], and numerous reports on the individual components of such systems [25-37]. The low power requirements, small size, and eventual low production cost of μGC systems favor their use in field settings. For those systems employing arrays of microsensors for detection, advantage can be taken of the crude spectrum they provide in a manner analogous to that in GC-MS systems. However, the microsensors used in such systems generally lack sufficient sensitivity to achieve the low limits of detection (LOD) required for many applications [17,19-24], including the security applications considered here.

Preconcentration devices for vapors of explosives and their markers have been developed in parallel with portable instrumentation developed for their detection [2], and include large,

high-volume samplers with partially selective filters or low-surface-area adsorbent materials for trapping particles and vapors, respectively [2,38-40]. No data could be found on preconcentration factors or sample capacities for such devices. Solid-phase microextraction (SPME) has also been used for explosive vapor sampling [41], but the long sampling time required to passively collect sufficient analyte mass is a limiting factor.

Microfabricated preconcentrators have also been reported for facilitating the detection of explosives with portable instruments; some with sorbent materials designed to interact preferentially with nitroaromatic compounds [27] and others with commercial porous polymers [26, 28]. Their small size reduces the dead volume and their low mass improves the efficiency of thermal desorption, but the preconcentration factors achievable and minimum sampling times required are constrained by inherent limitations on the maximum sorbent mass that can be loaded into the devices and the maximum flow rate that can be drawn through them, respectively. Thus, it is not possible to sample sufficiently large volumes of air and/or trap sufficient analyte mass in a short enough period of time with micro-scale preconcentrators to meet the demands of security screening for explosives [42].

As part of an effort to construct a μGC prototype for the analysis of explosive marker compounds, the work described here concerns the development of a hybrid preconcentrator-focuser (PCF) module that combines conventional and microfabricated devices in a manner that uses the attributes of each to best advantage while minimizing their shortcomings. The approach taken is modeled after that for another PCF module we developed recently for a different μGC prototype [42], which was designed for monitoring vapors of trichloroethylene in complex mixtures [19-21]. Figure 2-1 shows a block/fluidic diagram of the PCF module and the other analytical components of the current μGC prototype. In operation, a finite volume of

contaminated air would be passed through the pre-trap and sampler, both of conventional designs and dimensions, at a high flow rate, quantitatively capturing the marker compounds along with some fraction of other vapors of similar volatility on the sampler adsorbent bed. These compounds would then be thermally desorbed and transferred to the microfocuser (μF) at a lower flow rate of scrubbed ambient air, and then thermally desorbed again and injected to the microfabricated column (1-m length) at yet a lower flow rate of scrubbed air that is compatible with efficient chromatographic separation. The combination of separation and microsensor array detection increases the reliability of the marker determinations in the presence of interferences.

Selective preconcentration is desirable to exclude potential interferences. Since physical adsorption of moderately polar organic compounds is primarily a function of their vapor pressures, this was used as the basis for a crude selectivity scheme. By use of a pre-trap to remove particle-adsorbed low-volatility interferences, and by use of a hydrophobic, medium-surface-area adsorbent material in the sampler and μF that would not retain water or higher-volatility interferences, the PCF module could simplify the downstream separation and response-pattern discrimination problems, while also reducing power requirements and the duration of each sampling/analytical cycle.

In this article we describe the design, development, and characterization of this hybrid PCF module. The criteria used to guide the selection of adsorbent materials, the duration of each step in the overall analytical cycle, minimum sample masses, and a set of relevant interferences are presented first, followed by results of experiments aimed at optimizing the performance of the sampler, μF, and pre-trap individually. Results obtained with the integrated PCF module connected to a microfabricated GC column and a flame-ionization detector (FID) are then presented.

2.2. Experimental

2.2.1. Materials

The explosive markers DMNB, 2,6-DNT, and 2,4-DNT, as well as the n-alkanes and other volatile organic compounds (VOCs) used as interferences (Table 1) were purchased from Sigma-Aldrich/Fluka (Milwaukee, WI) or Acros/Fisher (Pittsburgh, PA) in > 99% purity and were used as received. Standard solutions of the markers were obtained from AccuStandard (New Haven, CT) in 1 mg/L concentrations in methanol/acetonitrile. The graphitized carbons, Carbopack B, Y, and F (C-B, C-Y, C-F, 60/80 mesh; specific surface areas of 100, 25, and 5 m^2/g, respectively) were obtained from Supelco (Bellefonte, PA). Samples were sieved and the fractions with nominal diameters in the range of 212 – 250 μm were isolated, preconditioned at 350 °C for 6 hours under helium, and packed in the appropriate device. Glass beads (< 1 m^2/g, 212 – 250 μm diam.) were obtained from Sigma-Aldrich and were similarly preconditioned prior to use.

2.2.2. Sampler and μF construction

The high-volume sampler (Figure 1b) is a 6-cm long, 0.64 cm i.d., stainless-steel tube with a welded side-port tube (6 cm long, 0.16 cm i.d.) located 1.5 cm from one end. A thin layer of polyimide tape (McMaster-Carr, Elmhurst, IL) was wrapped around the primary and side-port tubes for electrical insulation. A lacquered Cu wire coil provided heating and a fine-wire thermocouple (Omega, Stamford, CT) held snugly against the tube wall monitored the temperature. Stainless-steel Swagelok® fittings (H.E. Lennon, Farmington Hills, MI) were used to connect the sampler to other system components (note: Teflon fittings were used initially, but were

prone to leakage after repeated thermal cycling). The adsorbent material was retained in the primary tube between plugs of silanized glass wool and micromesh stainless steel screening (Product # 42-6110, Ted Pella, Inc., Redding, CA), and a thin strip of stainless steel was bent and inserted in each end to prevent the bed from shifting over time.

Three μF devices were tested. The overall chip dimensions were 4.2 (w) × 7.3 (l) × 0.6 (h) mm for the small and medium sized device, and 4.2 (w) × 9.8 (l) × 0.6 mm (h) for the large device (Figure 1c). Each μF chip contains a DRIE-Si cavity with tapered inlet/outlet, DRIE-Si pillars (0.15 mm widths and spaces, 0.38 mm height) near the inlet and outlet ports for retaining the adsorbent granules, a side port for filling with adsorbent, and inlet and outlet flow channels. An additional etched channel with a tee connection to one of the two main flow channels facilitates loading and backflushing of vapor samples. All three fluidic ports on the μF chips have expansion sections that accept 250 μm i.d. fused-silica capillaries used for interconnections. Evaporated Cr/Au heater contacts and a Ti/Pt RTD are used for controlled thermal desorption/injection by bulk heating. The device is sealed with an anodically bonded Pyrex plate (0.1 mm thick). Deactivated fused-silica capillaries (0.250-mm i.d., 10 cm long, Supelco, Bellefonte, PA) were inserted in the fluidic ports and secured with silicone adhesive (Duraseal® 1531, Cotronics, Brooklyn, N.Y). Electrical connections to a custom printed circuit board were made using gold wire-bonds. The μF was packed with the adsorbent by applying gentle suction to the outlet port through the fill port at the side of the cavity. After packing, the filling port was sealed with Duraseal®. Approximately 0.5, 0.9 and 2.0 mg of C-B were packed in the small, medium and large μF device cavities, respectively, as determined gravimetrically. The inlet capillary of the μF was connected to the side-port tube of the sampler by means of a 0.16 cm i.d. stainless steel union (Valco, Houston, TX) also wrapped with a Cu wire coil.

2.2.3 Test atmosphere generation

Saturated test atmospheres of the marker compounds were prepared in seasoned (i.e., pre-exposed and purged multiple times) 3-L Tedlar bags (SKC, Eighty-four, PA) filled with clean dry air. Blank samples collected from these bags did not show detectable amounts of phenol or dimethylacetamide or other impurities normally found at low levels in samples taken from such bags [43]. Aliquots were then transferred by gas-tight syringe to a series of other seasoned bags prefilled with clean dry air to achieve the desired concentrations. Test atmospheres of the less volatile alkanes (i.e., C_{14}-C_{16} n-alkanes) were prepared in a similar way. Due to the very low volatility of the markers, some loss is expected from condensation and adsorption to the bag walls. Therefore, a bench-scale GC with FID and ECD detectors (Model HP6890, Agilent Technologies, Palo Alto, Ca), calibrated with standard solutions of the markers, was used to confirm vapor concentrations. Mixed atmospheres of the markers and the compounds listed in Table 2-1 were prepared by taking samples of saturated atmospheres of the markers and C_{14}-C_{16} n-alkanes, and liquid samples of the other VOCs and combining them in one 20-L Tedlar bag. All test atmospheres were kept at ambient temperature.

2.2.4. Capacity and desorption efficiency of sampler

Sampler breakthrough tests were performed using the heater coil to maintain the device at a baseline temperature of 40 °C, which is the anticipated maximum ambient temperature inside the μGC prototype. With the side-port temporarily capped, air samples were drawn from the test atmosphere through the sampler at 3 L/min with a diaphragm pump (D737B, Parker, Cleveland, OH). Stainless-steel tubing (0.64 cm i.d., Siltek®, Restek, Bellefonte, PA) was used for all the

connections. A tee connector with a septum-sealed side-port was inserted downstream and a gas-tight syringe was used to collect samples roughly every 30 sec and inject them into the bench-scale GC for separation on a short capillary column and detection with the ECD. The dynamic adsorption capacity was evaluated in terms of the 10% breakthrough volume, $V_{b\text{-}10}$, which is the sample volume required for the concentration downstream from the adsorbent tube to reach 10% of the challenge concentration. This was determined for each marker by direct injection of the marker from the test atmosphere into the GC. All breakthrough tests were performed in duplicate using a mixed atmosphere containing 25 ppb of each marker and each interference in Table 2-1. DMNB was used as the sentinel vapor, because it is expected to break through more rapidly than the other less-volatile markers.

Desorption tests entailed spiking the sampler and monitoring the downstream concentration profile as a function of the heating rate and desorption (air) flow rate. The primary purpose was to determine the time required to transfer the sample to the μF. Tests were performed with spikes of each marker individually, mixtures of all three markers, and mixtures of the markers and 22 interferences. The presence of any residual material on the adsorbent following the initial desorption was also determined by collecting follow-up blank samples and desorbing again under the same conditions as in the first sample.

The sampler was mounted on top of the GC with the side-port extending into the GC oven through a small hole. A 15-cm section of deactivated fused-silica capillary connected the side-port directly to the FID through a press-fit Y-connector, which was used to split the desorption flow stream (i.e., no separation column was used for these tests). The sampler was loaded by drawing the sample from the test atmosphere using a pump, with the side-port temporarily blocked. By switching the appropriate valves, clean, dry air was passed in the opposite direction under positive

pressure while the sampler was heated to desorb the vapors with backflushing. A section of deactivated capillary inserted in one branch of the Y-connector served as a flow restrictor so that only ~15% of the total desorption flow stream passed to the FID, while the remainder was vented. Flow rates through both paths were measured with an electronic flow meter (Drycal, Bios International, Butler, NJ). The GC oven temperature was set to 75 °C to reduce wall adsorption. A needle valve located upstream from the sampler was used to set the desorption flow rate at each of four values ranging from 10 to 60 mL min^{-1}. After each analysis, two subsequent 1-L samples of purified dry air were desorbed to check for residue in the sampler.

The sampler was heated closed-loop, with control provided by a laptop running a routine written in LabVIEW (Ver. 8.5, National Instruments, Austin, TX). A pair of digital outputs from a data acquisition board (DAQ, USB-6501, National Instruments, Austin, TX) switched on/off two voltages, one to provide rapid heating rate, and the other to maintain the final temperature. Three heating rates were tested: 15, 22, and 44 °C/sec. The voltages applied to reach a final temperature of 250 °C, were 17, 19, and 22 VDC, respectively. A bias of 9 VDC was applied to maintain the final temperature in all three cases. Chromatograms from breakthrough tests (ECD) or composite peak areas from desorption tests (FID) were collected and processed using Chemstation software (Rev.B.01.01, Agilent Technologies, Santa Clara, CA) and GRAMS32 (version 6.0 Thermoscientific, Pittsburgh, PA).

2.2.5. Capacity and desorption efficiency of μF

Preliminary capacity testing employed test atmospheres of DMNB drawn continuously through the μF at different flow rates and bed masses. As above, aliquots were taken from a downstream tee connector and injected into the GC with a short capillary column and an ECD to

measure fractional breakthrough volumes. In subsequent experiments, the μF was mounted inside the GC oven and connected with deactivated capillary to the side-port of the sampler and to the Y-connector leading to an FID. The effluent from the μF was monitored at different sampler desorption flow rates, baseline (oven) temperatures, and spiked quantities of the markers and interferences on the sampler. The area of the FID peak measured downstream from the μF, which is an unresolved composite of the markers and interferences, was determined and expressed as a (mass) fraction, M_x, of the (previously measured) thermal desorption peak area generated by the sampler, M_o.

The thermal desorption profile of the μF was determined at desorption flow rates ranging from 1.8 to 12 mL/min and maximum desorption temperatures of 175 to 280 ºC, achieved at a rate of ~ 375 °C/sec. In these experiments, the μF was placed in line between a GC inlet and the FID in the GC oven held at 70 °C. A 10-cm segment of fused-silica capillary wrapped with a Cu heating coil wire was used to connect the μF and FID and was maintained at ~100 °C by applying 6 VDC across the wire. Under these conditions, the μF-FID hold-up time was less than 1 sec for all flow rates, band broadening in the tubing was negligible, and the injection band width could be ascertained. Purified air was used as carrier gas. Using an auto-sampler (HP7673, Agilent, Palo Alto, CA), 0.5-μL samples of acetone solutions containing 0.1 mg/mL of the individual marker compounds were injected through the GC inlet (4 psi inlet pressure) and a short section of capillary into the μF via one branch of the on-chip tee connection using a low flow of air as the carrier gas. The 50-ng injection is equivalent to ~7 ppb of the markers in a 1-L air sample, which exceeds the expected concentrations to be encountered in practice (tests were performed to confirm that there is no breakthrough with such injections). In a subsequent step, the port on the opposite end of the μF chip was manually connected to the GC inlet and the other port was connected to the FID using

press-fit connectors, while keeping the tee branch port sealed. The μF was then heated to the desired desorption temperature. Desorption flow rates were adjusted by varying the GC inlet pressure and were measured downstream from the connecting capillary with a bubble meter.

The maximum μF desorption temperature was adjusted and monitored via a laptop computer running a custom LabVIEW program. Using a 16-bit DAQ card (USB-6218) 36 VDC was applied to the integrated heater using pulse-width modulation to adjust the heating rate, and then 9 VDC was applied to maintain the final temperature. Data were collected and processed as described above, and the full width at half maximum (fwhm) of each desorbed peak (FID) was used to assess performance.

2.2.6. Pretrap construction and testing

The initial pre-trap design consisted of a stainless steel tube similar to that used for the sampler, but packed with different adsorbent materials (i.e., 5-mg beds of either glass beads or C-F). A test atmosphere of 2,4-DNT was drawn continuously through to the device and aliquots collected by gas-tight syringe from a downstream tee connection with a septum-port were injected into the GC (ECD) to monitor for breakthrough. The goal was to assess the extent of retention of the least volatile marker.

Subsequently, a 37-mm mixed cellulose ester (MCE) particulate filter housed in a styrene acrylonitrile cassette (SKC, Eighty-four, PA) was tested as a pre-trap. The cassette was connected upstream from the sampler, 1-L samples of a test atmosphere containing 10 ppb of 2,4-DNT were drawn at 3 L/min, and the captured mass was put through a normal analytical sequence, including separation and FID detection. Results were compared to those obtained without the pre-trap installed to assess the extent of loss of 2,4-DNT to the filter.

2.2.7. Performance of PCF module

To test the transfer efficiency and performance of the assembled PCF module, the setup and procedure previously described for the μF capacity test were used with the addition of a microcolumn between the μF and FID. The microcolumn chip was 3 × 3 cm and consisted of a 1-m-long square-spiral channel having a cross section of 150 μm (w) × 240 μm (d) etched in Si and an anodically bonded Pyrex cover plate to seal the top. Tapered inlet/outlet ports at opposing edges accepted 250-μm i.d fused-silica interconnection capillaries, which were epoxied in place. The stationary phase was polydimethylsiloxane (PDMS, 0.15 μm thick), deposited by a static coating method described previously [32].

The sampler was loaded by drawing the sample from the test atmosphere using a pump, with the side-port temporarily blocked. Valves were switched and the sampler was heated to desorb the vapors with backflushing through the side-port and into the μF. The μF port that was downstream during the focusing step was then manually connected to the GC inlet. Capping the tee branch port and connecting the other port to the microcolumn, the μF was heated to desorb the vapors with backflushing into the microcolumn and FID. For the transfer efficiency tests, individual atmospheres of DMNB and 2,4-DNT at two concentrations each were analyzed five times each. Finally, a test atmosphere containing the three markers and 22 interferences was connected upstream from the sampler (without pre-trap), and a complete analysis, including chromatographic separation, was performed.

2.3. Results and discussion

The primary performance criteria dictating the design and operating parameters of the ultimate μGC system into which the PCF module is to be incorporated are the speed of analysis, limits of detection (LOD), and the selectivity/reliability of the marker determinations. The first two of these relate directly to the PCF module performance. With respect to the trade-off between sensitivity and analysis time for explosive markers in the vapor phase, there was little guidance found in the literature, so we adopted provisional goals of < 2 min per analysis (including sampling, focusing, separation and detection) and 1 ng as the LOD for each marker. Given these criteria and preliminary data collected on the sensitivities of the sensors in the chemiresistor (CR) array used in the μGC prototype, we then decided on a target sample volume of 1 L. This, in turn, leads to a minimum detectable air concentration of ~0.14 ppb for 2,4-DNT, 2,6-DNT, and DMNB. In order to meet the 2-min analysis time criterion, the duration of each mode in the analytical sequence was set as follows: 20 sec for sampling, 40-sec for focusing, and 1 min for separation/detection.

Defining the nature and number of interferences was also necessary for developing the PCF module because this factor influences the types and amounts of adsorbent materials employed. Two sets of potential interferences were included. The first set (Set 1) consisted of 15 common indoor VOC air contaminants, chosen because they would also likely be in the background of air samples collected at potential security check points. These VOCs are more volatile than the markers and were expected to be removed by selective preconcentration in the sampler (and μF) prior to injection. The second set (Set 2) consisted of C_{10}-C_{16} n-alkanes, which have vapor pressures comparable to those of the explosive marker compounds, and also serve as model jet fuel compounds. They were expected to be transferred along with the markers through

the entire analytical system and would need to be separated/discriminated from the markers. Lower volatility compounds, including TNT, and airborne particulates were expected to be trapped in the pre-trap filter.

2.3.1. Sampler optimization

The sampler required a sufficient quantity of the appropriate adsorbent to capture the marker compounds quantitatively at 3 L/min with a breakthrough volume > 1 L in the presence of interferences competing for adsorption sites (including water vapor). At the same time, the adsorbent must permit rapid and complete release of the entire mass of captured markers (and Set 2 interferences) without decomposition upon heating in air. C-B was chosen for use in the sampler (and μF), following previous work from our group [42,44] and guidelines from technical reports [45] that suggested its suitability for adsorbing and thermally desorbing compounds with vapor pressures comparable to those of the markers.

Samplers packed with either 25 mg or 50 mg of C-B were challenged initially with test atmospheres containing 50 ppb of DMNB, at a baseline temperature of 40 °C. Both samplers provided more than enough capacity: the 25-mg and 50-mg beds of C-B gave a $V_{b\text{-}10}$ values of ~12 L and > 23 L, respectively. In subsequent tests, the samplers were challenged with test atmospheres containing 25 ppb of the three markers (DMNB, 2,6-DNT and 2,4-DNT) and 25 ppb each of the 22 interferences listed in Table 2-1. The 50-mg bed of C-B gave a $V_{b\text{-}10}$ > 23 L (Figure 2-2), indicating more than enough capacity, while the 25-mg bed of C-B gave a $V_{b\text{-}10}$ of < 0.5 L, indicating insufficient capacity.

Desorption profiles were then generated in duplicate with the 50-mg bed of C-B at desorption flow rates of 10, 20, 40, and 60 mL/min for each marker compound individually and

then as a ternary mixture at marker loadings corresponding to 25 ppb-L. The sampler was heated from 40 to 250 °C at 15 °C/sec and maintained at that temperature for 45 sec (note: faster heating rates of 22 and 45 °C/sec produced only minor changes in desorption peak width and were not pursued further because of the higher power dissipation). Figure 2-3a summarizes the results. At 60 mL/min, which was the maximum flow rate achievable with the diaphragm pump with the upstream flow resistance presented by the sampler and interconnects, the base peak width of 2,4-DNT was 32 sec, while those of DMNB and 2,6-DNT were both ~26 sec. At 40 mL/min the peak widths increased to 36 sec and ~30 sec, respectively, and at 10 mL/min they increased to 58 sec and ~48 sec, respectively. The desorption band width of the ternary mixture was identical to that of 2,4-DNT at 40 and 60 mL/min and just slightly larger at 10 and 20 mL/min. In light of these results and those from initial tests of the μF capacity showing a significant reduction in the capacity for DMNB between 40 and 60 mL/min for a continuous challenge (Figure 2-A.1, supplemental information), a 40 mL/min sampler desorption flow rate was adopted for subsequent experiments.

Unfortunately, analyte residues as high as 10% were evident upon a second thermal desorption of the mixture of the three markers from the 50 mg C-B sampler bed desorbed at 40 mL/min. Therefore, a portion of the C-B was replaced with the lower-surface-area C-Y, and a tandem bed with 30 mg of C-B and 15 mg of C-Y was tested. The lower surface-area C-Y bed was placed last in the flow order during sampling (and first during desorption). The sampler was then challenged with a mixture of 10 ppb of each marker and 25 ppb of each interference. Duplicate tests with PCF module connected to a short column and ECD detector gave $V_{b\text{-}10}$ values of ~ 1.5 L for DMNB, the sentinel compound, in the mixture. There was ~7% DMNB breakthrough for a 1-L sample, indicating that this dual-adsorbent bed should provide sufficient capacity at the lower

concentrations expected in actual environments. Note that since an ECD was used, none of the interferences were detected and the extent of their retention on the sampler is not known from these tests.

To characterize the dynamics of desorption from the dual-adsorbent bed, a test atmosphere containing 10 ppb of each marker and 25 ppb of each interference in Table 2-1 was first drawn through the sampler at 3 L/min for 20 sec. The flow was reversed, the sampler was heated to 250 °C at 15 °C/sec, and the peak profile was monitored with an FID connected through a vented capillary. Figure 2-3a shows the desorbed peak widths as a function of flow rate. In all cases, the desorption bands were slightly narrower than those obtained for the mixture of the markers with the 50 mg C-B bed (also shown in Figure 2-3a). The fractional carry over determined upon the second desorption was low in all cases, ranging from 1.7-1.1% for flow rates of 10-60 mL/min, respectively. It is important to note that many of the more volatile interferences will not be present in the desorbed sample, and that its composition will be dominated by the marker compounds and the Set-2 interferences.

Figure 2-3b shows the desorption profile from the dual-bed sampler at 40 mL/min after collecting a 1-L sample of the same mixture of markers and interferences. It required 32 sec to completely desorbed the mixture. The first of two subsequent clean-air blank runs gave a peak area that was only 1.7% of that from the first desorption, and the second gave no detectable peak. This corresponds to a desorption efficiency of 98.3%.

2.3.2. Quantitative transfer from sampler to μF

Prior to testing the μF in conjunction with the sampler, several experiments were performed to determine the proper size of the μF adsorbent cavity and associated mass of C-B, and

the effect of flow rate on capacity. Devices with different cavity volumes and associated packed-bed masses of C-B were challenged continuously at room temperature with 100 ppb of DMNB. Figure 2-A.1a in the Appendix shows that $V_{b\text{-}10}$ increased roughly linearly with the bed mass, ranging from ~ 50 mL for the 0.5-mg bed (smallest cavity) to 600 mL for the 2-mg bed mass (largest cavity). Figure A.1b (Appendix) shows the effect of flow rate on the largest device, with $V_{b\text{-}10}$ (100 ppb DMNB) decreasing linearly from 600 mL to 150 mL as the flow rate was increased from at 10 mL/min to 70 mL/min. On the basis of these results, the larger μF device was selected for use in the PCF module.

Subsequent testing explored the capacity of this μF as a function of flow rate, baseline μF temperature, and sampled mass with the device connected downstream from the dual-bed sampler. In this case, the mass fraction (M_x/M_o) of the desorbed peak from the sampler was used to quantify breakthrough. The μF was placed between sampler and FID inside the GC oven, which was held at an elevated temperature to avoid wall adsorption losses in the fused-silica capillary connectors and to impart additional selectivity against interfering VOCs. Figure 2-A.2a (Appendix) shows that the capacity of the μF at 70 °C did not vary significantly over focusing flow rates of 10-40 mL/min when challenged with the mixture of markers and interferences: M_x/M_o values were all in the range of 5-7%. Figure 2-A.2b (Appendix) shows the temperature dependence of the capacity at a focusing flow rate of 40 mL/min: the M_x/M_o values were 4, 7, and 26%, for 60, 70, and 80 °C, respectively. Although the nature of the compounds breaking through the μF is unknown, it is reasonable to assume that most of the interferences in Set 1 are not trapped by the sampler, and that the peak consists primarily of the markers and Set-2 interferences. Figure 2-A.2c (Appendix) shows that M_x/M_o for the μF was ~9% for mass loadings onto the sampler up to 110 ng (i.e., 15 ppb·L) of each marker (40 mL/min, 70 °C). Thus, focusing for 40 sec at 40 mL/min with the μF

held at 70 °C seems to be adequate to transfer the markers from the sampler to the μF with acceptably low transfer losses (i.e., < 10%).

2.3.3. μF desorption profile

The μF desorption profile was then characterized as a function of flow rate and maximum desorption temperature (T_{max}) using air as the carrier gas and 50-ng spikes of the markers. Figure 2-4a shows the full-width-at-half-maximum (*FWHM*) of the profiles for three markers from 1.2 to 12.5 mL/min (T_{max} = 250 °C) on the basis of individual-marker tests. The 2,4-DNT is affected the most, with the *FWHM* value decreasing from 9.6 to 1.5 sec over this range of flow rates. For 2,6-DNT, the *FWHM* reaches a minimum of 1.6 sec at 6.5 mL/min with no further decrease at the higher flow rates, and for DMNB the *FWHM* shows relatively little dependence, decreasing from 2.1 to 1.4 sec over the full range of flow rates. These results are consistent with those reported by Lu et al. [44] and by Whiting et al. [46] and indicate that flow rate has a significant influence on desorption dynamics. However, since the desorption flow rate is also used for separation, the flow rate dependence of the latter must be considered.

A previous study of similar 1-m μcolumns showed that the minimum plate height is achieved at ~0.2 mL/min using air as carrier gas and at ~0.8 mL/min using helium [32]. As shown in Figure 2-4a, desorption flow rates in this range produced peaks with large *FWHM* values that would seriously compromise chromatographic resolution. A trade-off between injection band width and chromatographic efficiency was necessary. On the basis of empirical data collected separately with the μGC prototype, a flow rate as high as 3 mL/min still permitted reasonable resolution of the two primary marker compounds, DMNB and 2,4-DNT, from the Set-2

interferences, and yielded relatively low LODs using a sensor array detector. Therefore, this flow rate was adopted for system-level testing.

Figure 2-4b shows the effect of T_{max} on *FWHM* at 3 mL/min. Both 2,6-DNT and 2,4-DNT show a dramatic ~4-fold decrease in *FWHM* between 175 and 250 °C, with a relatively small additional decrease up to 275 °C. DMNB shows a ~2-fold decrease in *FWHM* up to 250 °C, with no further narrowing at 275 °C. Since the improvement was small above 250 °C, and the adhesive used to seal the capillary interconnects in the μF inlet/outlet ports has a maximum recommended operating temperature of 285 °C, the former was adopted as the maximum μF desorption temperature. The *FWHM* values for DMNB, 2,6-DNT, and 2,4-DNT were 1.2, 3,5, and 3.8 sec (note: on-column focusing was ultimately used to mitigate further the width of the these injection bands for the DNT isomers, even at a baseline temperature of 70 °C).

2.3.4. Pre-trap characterization

Although the markers have relatively low vapor pressures, it is necessary to exclude interfering compounds with even lower vapor pressures that might adsorb irreversibly to internal surfaces in the flow path or to the sampler adsorbents, or that would require excessively high temperatures and long elution times to analyze. In devising a pre-trap for such compounds, a primary emphasis was placed on avoiding significant retention of the marker compounds. This factor, then, was used as the basis for screening different approaches to pre-trap design and operation.

Separate tests were performed with 5-mg beds of C-F and glass beads at room temperature using 2,4-DNT as the sentinel test marker because it is the least volatile marker. The breakthrough curves in Figure 2-A.3 (Appendix) show that 2,4-DNT (10 ppb) is retained at unacceptably high

levels; in a 1-L sample volume, the C-F and glass bead pre-traps, retained 92 and 54% of the 2,4-DNT, respectively.

As an alternative that recognized that many less-volatile interferences will adsorb to particles in the air and to most surfaces at ambient temperature, a mixed-cellulose-ester (MCE) membrane (37-mm diameter, 0.8 μm pore size) housed in a polystyrene cassette was tested. The cassette was attached upstream from the sampler. Duplicate 10-ppb samples of 2,4-DNT were collected on the sampler at 3 L/min with and without the MCE filter installed upstream. Collected samples were then desorbed and analyzed using a 1-m microcolumn and an FID. The reduction in the peak area of 2,4-DNT with the MCE filter was only 5 and 8% compared to tests without the filter. Although no interference retention/breakthrough tests were performed, it is reasonable to expect that a significant fraction of compounds less volatile that 2,4-DNT, if present, would be adsorbed onto particle surfaces and trapped on the MCE membrane.

2.3.5. Performance of hybrid PCF module

At this point, 2,6-DNT was removed from the set of markers because it was realized that its vapor concentration would be so much lower than those of the other two markers and that it would contribute relatively little to the problem of explosive detection. The transfer efficiencies of DMNB and 2,4-DNT through the assembled PCF module were evaluated individually at two concentrations. A sample drawn by gas-tight syringe from a Tedlar bag saturated with the marker was injected slowly into a N_2 sample stream being drawn at 3 L/min through the sampler for 20 sec at room temperature. The amounts injected, determined by comparison to calibration curves generated with solution-phase samples, were 6.4 and 19.2 ng for DMNB, and 1.5 and 3.6 ng for 2,4-DNT. Assuming a 1-L sample volume, the corresponding concentrations would be 0.9 and 2.6

ppb for DMNB, and 0.2 and 0.5 ppb for 2,4-DNT. Five replicates were analyzed at the low concentration and single samples were analyzed at the high concentration of each marker. With the PCF module connected to the 1-m microcolumn and ECD, the recovered peak areas corresponded to transfer efficiencies of 86 ±5% and 94 % for DMNB, respectively, and 80±5% and 83 % for 2,4-DNT, respectively. For DMNB, the sample loss can be attributed to breakthrough during sampling and focusing. For 2,4-DNT, sample loss is more likely due to incomplete desorption from the sampler or μF, or to wall adsorption.

A preconcentration factor (PF) can be determined for each marker by taking the ratio of sample volume (i.e., 1 L) to the volume of the peak generated by the μF and then multiplying by the average fractional transfer efficiency [47]. This assumes that the mass contained in the air sample and in the injected peak differs only by the transfer losses. For the lower concentration samples above, the volume of the peak was estimated as the product of the base peak width and the injection/separation flow rate (3 mL/min). Values were 0.2 and 0.45 mL for DMNB (0.9 ppb) and 2,4-DNT (0.2 ppb), respectively. Using the average transfer efficiency values from above, this leads to PF values of ~ 4,500 and ~ 1,800, respectively.

Finally, a test mixture was analyzed using the PCF module connected to the 1-m microcolumn and FID. A test atmosphere containing 10 ppb each of DMNB and 2,4-DNT, and the set of 22 interferences (25-50 ppb each) was drawn through the dual-adsorbent sampler at 3 L/min for 20 sec with the sampler held at 40 °C. The markers and the fraction of the interferences retained on the sampler were thermally desorbed with backflushing and transferred to the μF at 40 mL/min for 40 sec while holding the μF at 70 °C. The μF was then heated to 250 °C and maintained at this temperature for 45 sec as the mixture was backflushed and injected onto the μcolumn at 3 mL/min.

Figure 2-5a shows the reference chromatogram of the 24 component test mixture obtained from injecting 0.5 μL of a dichloromethane solution of the analytes (0.2-2.5 mg/L) onto a 15-m PDMS capillary column with FID. Figure 2-5b shows the chromatogram for the same mixture, generated with the PCF assembly, connected to a 1-m microcolumn and FID. Peak assignments for both traces are based on retention times verified by individual injections of each component in solution. The entire mixture elutes in ~ 72 sec and, as expected, compounds less volatile than n-decane, as well as 1-hexanol, do not appear in the latter chromatogram (Figure 2-5b) because most of them are not retained and transferred to the separation module. In addition, the quantities of the C_{10}-C_{16} alkanes, which were higher than those of the markers in the test atmosphere, appear to be lower than expected as reflected in the areas of their peaks in Figure 2-5b. This suggests that they are breaking through the sampler or μF during sampling and focusing.

The two markers are partially resolved from n-dodecane and n-hexadecane. The values of chromatographic resolution, R_s, were determined using Fourier peak deconvolution, and are 0.9 (DMNB/*n*-C_{12}), and 0.4 (2,4-DNT/*n*-C_{16}). Assuming similar resolution was obtained with the CR array to be used in the prototype μGC, the degree of separation between DMNB and *n*-C_{12} is sufficient for determining the marker directly with little error. For 2,4-DNT and *n*-C_{16}, chemometric analysis of the response patterns from the CR array would be required for the marker determination [48].

2.4. Conclusions

We conclude that the hybrid preconcentrator/focuser module described herein is suitable for use in a μGC system for fast determinations of vapors of explosive markers at low concentrations using air as the carrier gas. The systematic approach taken to designing and

developing the module should be generally applicable. The masses and types of adsorbents, component baseline and maximum temperatures, sampling and desorption flow rates, and heating profiles were carefully adjusted to optimize the trapping capacity, desorption efficiency, selectivity towards the explosive marker compounds, and transfer efficiency, while minimizing the analysis time.

Selective preconcentration is a critical aspect of module performance because of limitations on peak capacity inherent to μGC systems with relatively short separation columns. The use of a pair of medium-surface-area adsorbent materials in the sampler permits quantitative capture of the marker compounds at a high flow rate (and quantitative desorption), while allowing most co-contaminants of higher volatility to pass through unretained. This avoids crowding in the early part of the chromatograms and allows faster temperature programming of separations. Rejection of water vapor is also achieved by use of hydrophobic adsorbents of limited surface area.

Remarkably high preconcentration factors are achievable in a short time period by collecting a relatively large air-sample volume at a high flow rate with the macro-scale sampler and then focusing the trapped analyte mass into a small injection volume via the micro-scale device. The ability to rapidly heat and efficiently sweep the μF device at the low flow rates required for efficient microcolumn separations helps to minimize injection bandwidths. The net preconcentration factors achieved from the 1-L samples collected (in just 20 sec) with the PCF module ranged from 1,800–4,500, which should permit sufficiently rapid detection of sub-ppb concentrations of the markers to facilitate routine personnel and luggage screening in airport facilities. Achieving such levels of preconcentration in such a short time period would not be possible using only microfabricated components due to inherent constraints on maximum flow rates that can be passed through such devices [49].

The μGC prototypes that incorporate the PCF module described here are described in Chapter 3 and 4.

2.5. References

1. L. Thiesan, D. Hannum, D. W. Murray, J. E. Parmeter, Survey of commercial available explosives detection technologies and equipment, available at https://ncjrs.gov/pdffiles1/nij/grants/208, accessed April 2012
2. D. S. Moore, Rev. Sci. Instrum., 75, (2004), 2499.
3. Sabre 5000, Smiths Detection, available at http://www.smithsdetection.com/sabre5000.php, accessed December, 2012.
4. H. Riris, C. B. Carlisle, D. F. McMillen, D. E. Cooper, Appl. Optics, 35, (1996), 4694.
5. M. Wu, M. Ray, K. H. Fung, M. W. Ruckman, D. Harder, A. J. Sedlacek, Appl. Spectroscopy, 54, (2000), 800.
6. Z. G. Wu, C. L. Hendrickson, R. P. Rodgers, A. G. Marshall, Anal. Chem., 74, (2002), 1879.
7. N. L. Sanders, S. Kothari, G. M. Huang, G. Salazar, R. G. Cooks, Anal. Chem., 82, (2006), 5313.
8. R. G. Ewing, D. A. Atkinson, G. A. Eiceman, G. J. Ewing, Talanta, 54, (2001), 515.
9. Fido XT, ICx, available at www.icxt.com/uploads/file/products/ brochures/ Fido_XT.pdf, accessed April 2012.
10. Y. Xin, G. He, Q. Wang, F. Yang, Rev. Sci. Instrum, 82, (2011), 103102.
11. HAPSITE ER, Inficon, available at http://www.inficonemergencyresponse.com/en/hapsite_er//index.html, accessed May 2012.
12. A. P. Synder, C. S. Harden, A. H. Brittain, M. G. Kim, N. S. Arnold, H. L. C. Meuzelaar, Anal. Chem., 65, (1993), 299-306.
13. T. F. Jenkins, D. C. Leggett, T. A. Ranney, CREEL, special report 99-21, available at http://www.dtic.mil/cgi-bin/GetTRDoc?AD=ADA373402, accessed October, 2012.
14. R. P. Murrmann, T. F. Jenkins, D. C. Leggett, CREEL, special report 158, available at http://www.dtic.mil/cgi-bin/GetTRDoc?AD=ADA040632, accessed October, 2012.
15. Convention on the marking of plastic explosives for the purpose of detection, available at http://www.ciaonet.org/cbr/cbr00/video/cbr_ctd/cbr_ctd_33.html, accessed August 2012.
16. Canary Three, Defiant Technologies, available at http://www.defiant-tech.com/canarythree.php, accessed August 2012.
17. P. R. Lewis, R. P. Manginell, D. R. Adkins, R. J. Kottenstette, D. R. Wheeler, S. S. Sokolowski, D. E. Trudell, J. E. Byrnes, M. Okandan, J. M. Bauer, R. G. Manley, G. C. Frye-Mason, IEEE Sensors J, 6, (2006), 784.
18. S. Zampolli, L. Elmi, F. Mancarella, P. Betti, E. Dalcanale, G. C. Cardinali, M. Severi, Sens. Actuator B, 141, (2009), 322.
19. S. K. Kim, D. R. Burris, H. Chang, J. Bryant-Genevier, E. T. Zellers, Environ. Sci. Technol., 46, (2012), 6065.
20. S. K. Kim, D. R. Burris, H. Chang, J. Bryant-Genevier, K. A. Gorder, E. M. Dettenmaier, E. T. Zellers, Environ. Sci. Technol., 46, (2012), 6073.
21. S. K. Kim, H. Chang, E. T. Zellers, Anal. Chem., 83, (2011), 7198.

22. E. T. Zellers, G. Serrano, H. Chang, and L. K. Amos, Proc. Transducers 11', Beijing, China, June 5-9, 2082.
23. C. J. Lu, W. Steinecker, W. C. Tian, M. Oborny, J. Nichols, M. Agah, J. Potkay, H. Chang, J. Driscoll, R. Sacks, K. Wise, S. Pang, E. T. Zellers, Lab Chip, 5, (2005), 1123.
24. J. Liu, N. K. Gupta, K. D. Wise, Y. B. Gianchandani, X. D. Fan, Lab Chip, 11, (2011), 3487.
25. W. C. Tian, H. K. L. Chan, C. J. Lu, S. W. Pang, E. T. Zellers, J. Microelectromech S., 14, (2005), 498.
26. I. Voiculescu, R. A. McGill, M. E. Zaghloul, J. Stepnowski, S. Stepnowski, H. Summers, V. Nguyen, S. Ross, K. Walsh, M. Marin, IEEE Sensors J, 6, (2006), 1094.
27. M. Martin, M. Crain, K. Walsh, R. A. McGill, E. Houser, J. Stepnowski, S. Stepnowski, H-D Wu, S. Ross, Sens. Actuators B, 126, (2007), 447.
28. E. H. M. Camara, P. Breuil, D. Briand, N. F. de Rooij, C. Pijolat, Anal. Chim. Acta, 688, (2011), 175.
29. R. P. Manginell, D. R. Akins, M. W. Moorman, R. Hadizadeh, D. Copic, D. A. Porter, J. M. Anderson, V. M. Hietala, J. R. Bryan, D. R. Wheeler, K. B. Pfeifer, J. Microelectromech. S., 17, (2008), 1396.
30. B. Alfeeli, D. Cho, M. Ashraf-Khorassani, L. T. Taylor, M. Agah, Sens. Actuators B, 133, (2008), 24.
31. M. Kim, S. Mitra, J. Chromatogr. A, 996, (2003), 1.
32. G. Serrano, S. M. Reidy, E. T. Zellers, Sens. Actuators B., 141, (2009), 217.
33. S. Reidy, G. Lambertus, J. Reece, R.D. Sacks, Anal. Chem., 78, (2006), 2623.
34. A. D. Radadia, R. D. Morgan, R. I. Masel, M. A. Shannon, Anal. Chem., 81, (2009), 3471.
35. S. Ali, M. Ashraf-Khorassani, L. T. Taylor, M. Agah, Sens. Actuators B, 141, (2009), 309.
36. R. S. Jian, R. X. Huang, C-J. Lu, Talanta, 88, (2012), 160.
37. S.-J. Kim, G. Serrano, K. D. Wise, K. Kurabayashi, E. T. Zellers, Anal. Chem., 83, (2011), 5556.
38. K. L. Linker, F. J. Conrad, C. A. Custer, C. L. Rhykerd Jr., U.S. Pat. 6,085,601, 2000.
39. R. Ingram, J. Sikes, Proc. SPIE, 7664, (2010), 766415-1.
40. K. Cizek, C. Prior, C. Thammakhet, M. Galik, K. Linker, R. Tsui, A. Cagan, J. Wake, J. La Belle, J. Wang, Anal. Chim. Acta, 661, (2010), 117.
41. M. Joshi, K. Rigsby, J. R. Almirall, J. Forensic Sci., 208, (2011), 29.
42. T. Sukaew, H. Chang, G. Serrano, E. T. Zellers, Analyst, 136, (2011), 1664.
43. The Stability of Sulfur Compounds, Low Molecular Weight Gases, and VOCs in Five Air Sample Bag Materials, SKC Inc, available at www.skcinc.com/instructions/1805.pdf, accessed August 2012.
44. C. J. Lu, E. T. Zellers, Analyst, 127, (2002), 1061.
45. Thermal desorption guide, Supelco, available at www.sigmaaldrich.com /etc/medialib/docs/ Supelco/General_Information/t402025.Par.0001.File.tmp/t402025.pdf, accessed April 2012.
46. J. J. Whiting, R. D. Sacks, J. Sep. Science, 29, (2006), 218.
47. J. Namiesnik, Talanta, 35, (1988), 567.
48. C. Jin, E. T. Zellers, Anal. Chem., 80, (2008), 7283.
49. E. T. Zellers and T. Sukaew, Sensors and Actuators B, submitted.

Table 2-1. Interfering compounds and their corresponding vapor pressures, p_v, at 25 °C.

No.	Compound	p_v/kPa	No.	Compound	p_v/kPa
1.	benzene	12.6	12.	heptanal	0.31
2.	n-heptane	6.1	13.	2-methyl-2-hexanol	0.29
3.	1-propanol	2.8	14.	octanal	0.28
4.	n-octane	1.5	15.	**n-decane**[a]	0.19
5.	hexanal	1.1	16.	1-hexanol	0.14
6.	m-xylene	1.0	17.	**n-undecane**	0.055
7.	2-heptanone	0.63	18.	**n-dodecane**	0.040
8.	n-nonane	0.61	19.	**n-tridecane**	0.0073
9.	cumene	0.60	20.	**n-tetradecane**	0.0016
10.	2-hexanone	0.51	21.	**n-pentadecane**	0.0045
11.	isoamyl alcohol	0.32	22.	**n-hexadecane**	0.00013

[a] Compounds in bold type face belong to Set 2; other compounds belong to Set 1.

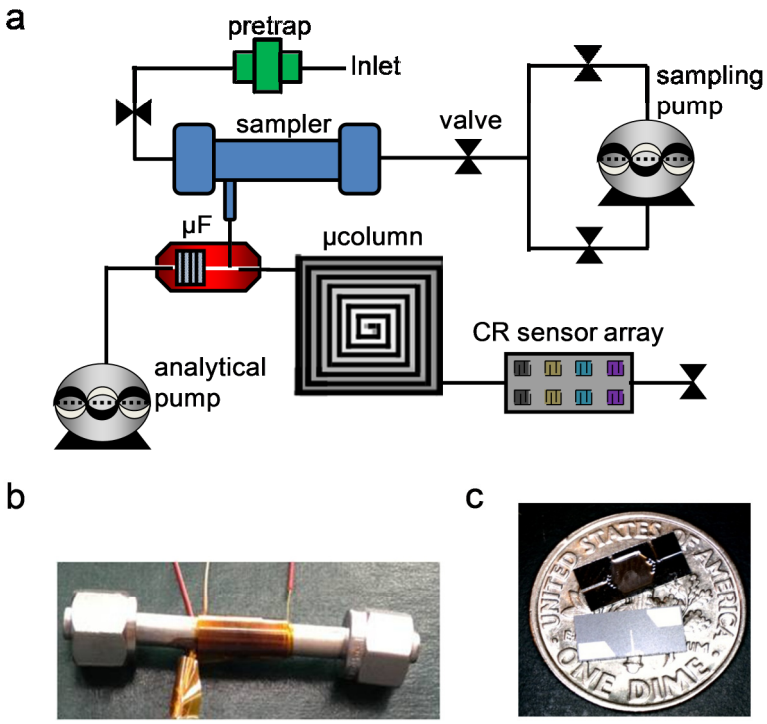

Figure 2-1. (a) Layout showing the key components of the hybrid PCF module and other components of the µGC prototype being designed for analysis of vapors of explosive markers; (b) photograph of the high-volume sampler wrapped with Cu wire; (c) photograph of the front and back sides of the µF on a U.S. dime.

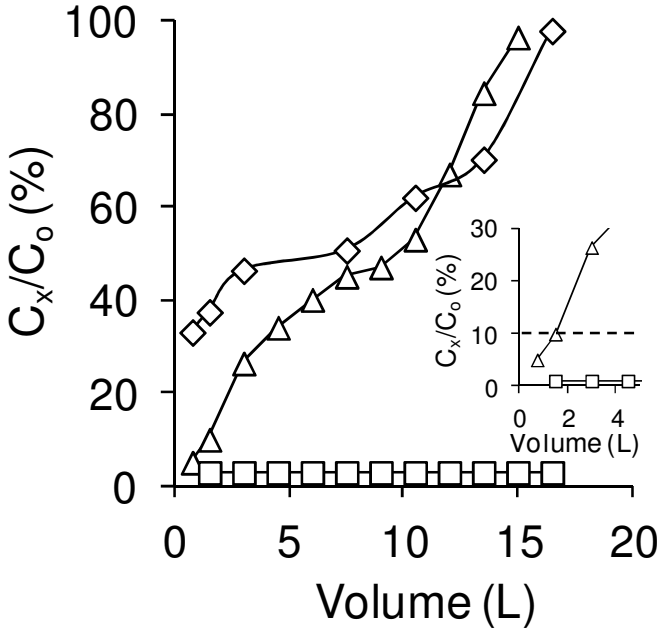

Figure 2-2. Breakthrough curves for samplers packed with 25 mg of C-B (diamonds), 50 mg of C-B (squares), and 15 mg of C-Y + 30 mg of C-B (triangles) exposed continuously to a test atmosphere containing the three marker compounds and the 22 interferences listed in Table 1 (C_o = 10 ppb for markers and 25 ppb for interferences). The sampling flow rate was 3 L/min and the sampler temperature was 40 °C. DMNB was used as sentinel breakthrough compound and analysis was by GC-ECD.

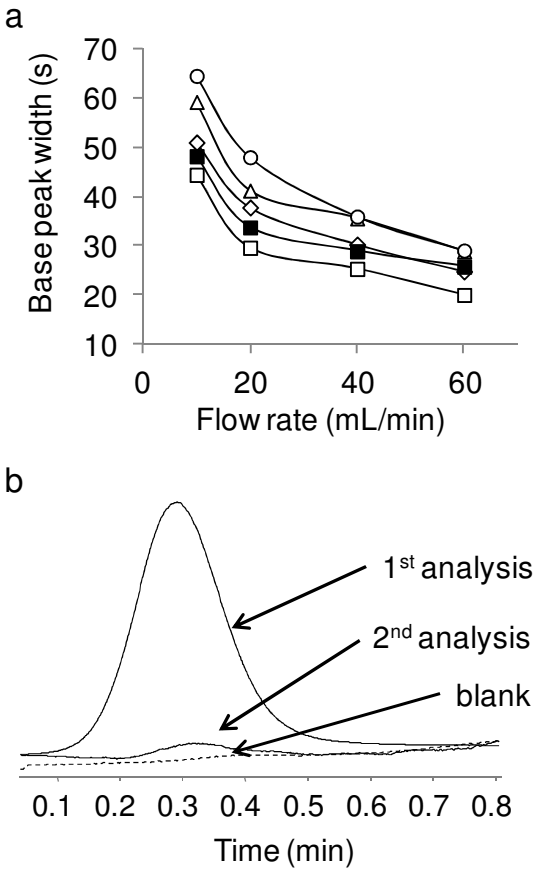

Figure 2-3. (a) Thermal desorption peak widths measured at the base as a function of flow rate through a sampler packed with 50 mg of C-B for DMNB (unfilled diamonds, 180 ng), 2,6-DNT (unfilled squares, 180 ng), 2,4-DNT (unfilled triangles, 180 ng), and the ternary mixture (unfilled circles, 180 ng each); and for a mixture of the marker compounds (~ 75 ng each) and a set of interferences (filled squares, 35-170 ng each), using the dual-adsorbent sampler packed with 30 mg of C-B and 15 mg of C-Y (1-L sample volume in all cases); (b) Chromatograms showing the thermal desorption profile of a mixture of the marker and those interferences from Table 1 that are trapped in the sampler using the dual-adsorbent sampler at 40 mL/min. The post-run analysis shows minimum carry over. The dashed line is from the blank run before the analysis. Sampler desorption temp.: 250 °C (15 °C/s), detector: FID, carrier gas: purified air.

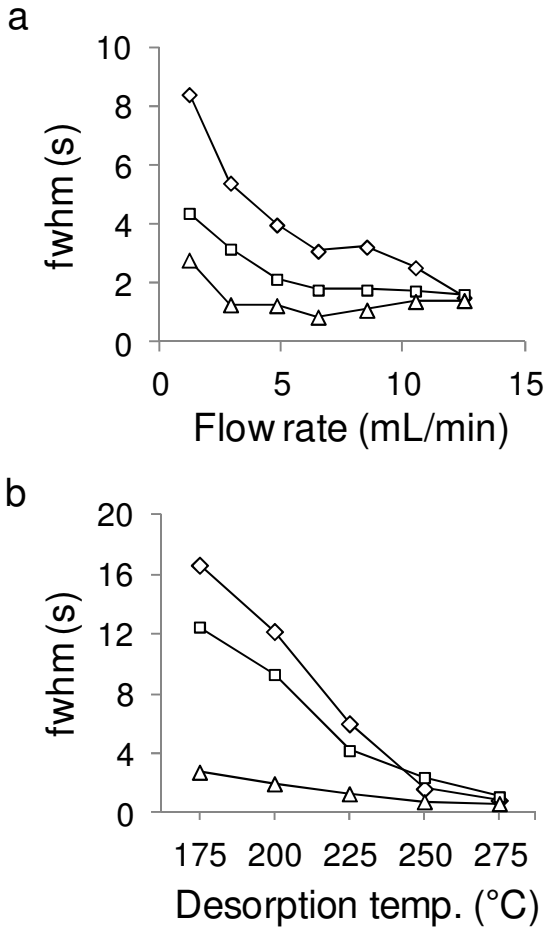

Figure 2-4. µF desorption band widths as a function of (a) flow rate (Tmax = 225 °C); and (b) Tmax (flow rate = 3 mL/min). Compounds: DMNB (triangles); 2,6-DNT (squares); 2,4-DNT (diamonds). µF initial temperature = 70 °C; mass injected = 50 ng of each compound; carrier gas = purified air; detector: FID.

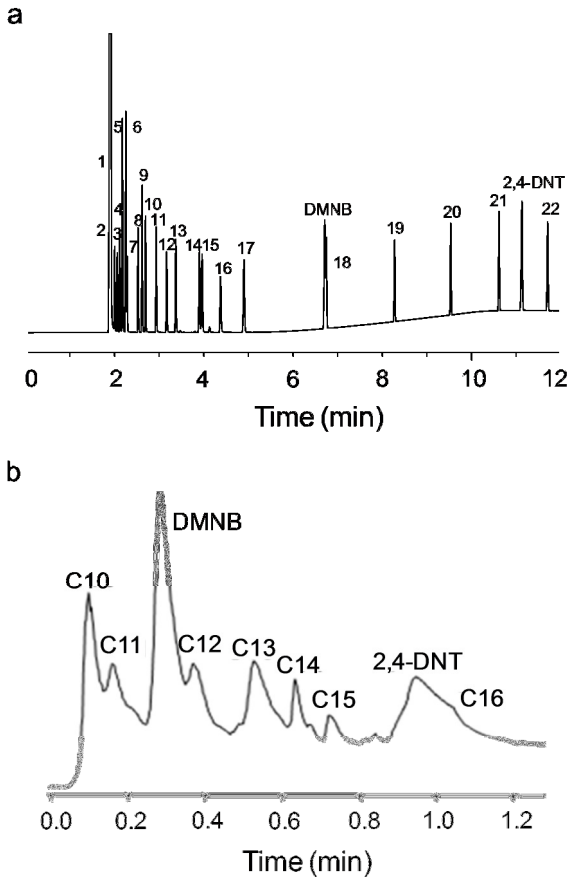

Figure 2-5. (a) Chromatogram of the 24 component mixture (i.e., DMNB, 2,4-DNT and the interferences listed in Table 1) using a 15-m PDMS capillary column and FID. Carrier gas: Helium, flow rate: 1.0 mL/min, column temp. ramp: 120 °C (initial) for 5 min, 18 °C/min to 180 °C, hold for 2 min. (b) Chromatogram obtained from a test atmosphere containing the same 24 compounds with the integrated subsystem: PCF module, 1-m microcolumn, FID. Compounds 1-14 (Table 1) passed unretained through the PCF module. Conditions: sampling at 3 L/min for 20 sec; focusing at 40 mL/min for 40 sec; analysis at 3 mL/min for 75 sec; microcolumn temperature program was 70 °C (initial) for 30 sec, 16 °C/s to 150 °C, hold 30 sec. Carrier gas: purified dry air; μF initial temp.: 70 °C.

APPENDIX I

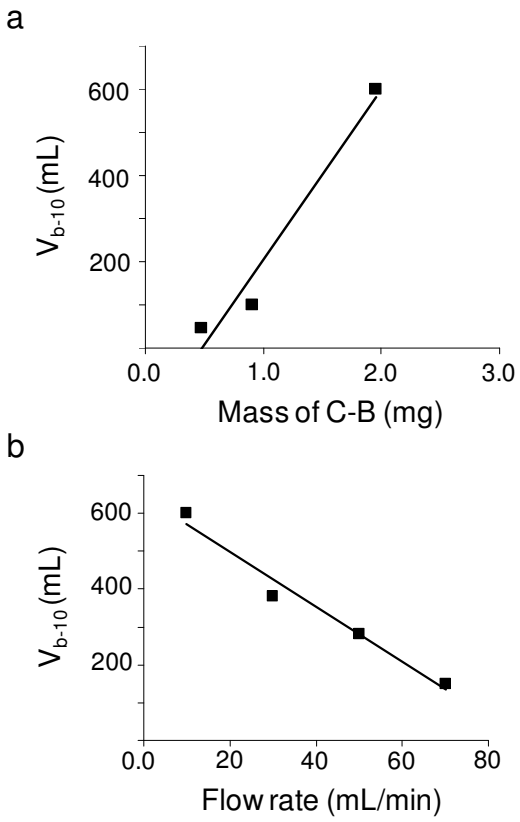

Figure 2-A.1. Dependence of the μF breakthrough volume, $V_{b\text{-}10}$, on (a) the μF cavity volume and associated packed-bed mass (C-B adsorbent) at 10 mL/min; and (b) flow rate for the μF packed with 2 mg of C-B. The vapor probe was DMNB at 10 ppb. The μF was at room temperature. Detector: FID.

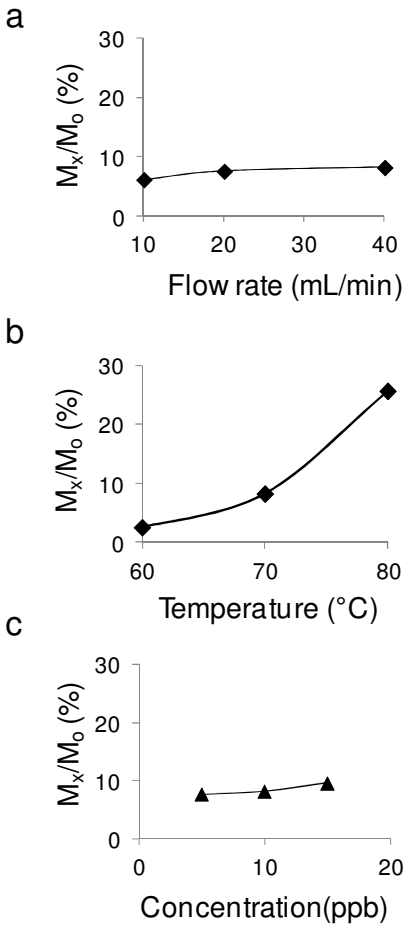

Figure 2-A.2. Dependence of μF breakthrough on (a) sampler desorption flow rate; (b) μF baseline temperature; and (c) vapor concentration. For these tests, the sampler was pre-loaded with a 1-L sample of a test atmosphere containing the three marker compounds (10 ppb each) and 22 interferences (25 ppb each) and thermally desorbed with backflushing at 250 °C. The entire desorbed sample was passed through the μF. Baseline temperatures of the μF for a) and c) were 70 °C. Detector: FID.

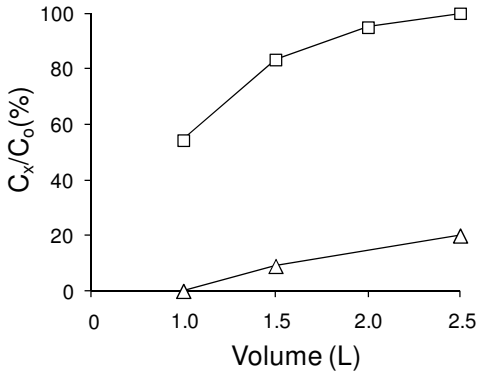

Figure 2-A.3. Breakthrough volume of 2,4-DNT through pre-traps consisting of a 5-mg bed of glass beads (unfilled squares) and a 5-mg bed of C-F (unfilled triangles) at a challenge flow rate of 3 L/min, showing significant retention of this marker compound. Challenge concentration = 10 ppb.

CHAPTER III

A LABORATORY PROTOTYPE MICRO GAS CHROMATOGRAPH FOR HIGH-SPEED DETERMINATIONS OF EXPLOSIVE MARKERS COMPOUNDS

3.1. Introduction

There is a current need for a field deployable explosives detection system for use in the screening of passengers, luggage, cargo containers and other potential targets for terrorist activity. Due to the nature of explosive threats, on-site explosive systems must provide a fast response, a very low rate of false alarms, and sensitivity and selectivity for adequate identification of the explosive material. Several common analytical methods have been tested for analysis of explosives, but only few have been successfully deployed for on-site detection [1-3]. The most popular techniques that have been adapted for field deployment include ion detection methods, mass spectrometry (MS) [4], and ion mobility spectrometry (IMS) [5]. Spectrometric methods, including infrared absorption spectroscopy (IR) [6] and Raman scattering [7], and UV/Visible methods, including fluorescent polymers [8, 9], have also been used in explosives detection.

IMS is currently, the most successful method for on-site explosive detection systems [2]. Among the features of IMS are the very low limits of detection (LOD, pg level), adequate selectivity, and portability. The rate of false positives can be a disadvantage due to ion suppression

by co-contaminants [1]; coupling detection with a separation method, such as GC, can greatly improve the accuracy and selectivity towards the target analytes [10, 11]. However, despite the advantages and commercial success of IMS systems, trained dogs are still the most common method to detect traces of explosives [1, 12]. This situation is the result of the main limitation of current technologies until recently, the lack of a stand-off detection mode, which requires the handling of the potential threat. Stand-off detection can be achieved by several ways, including the use of imaging techniques that can detect explosive residues at a distance [13] or by analyzing the vapor profile of the air surrounding the potential threat, in a similar way to how dogs identify the explosives [2, 3].

Detecting explosives such as TNT, HME, RDX, and C4 in vapor phase, however, is a complex challenge due to the very low volatility of these compounds at room temperature that often results in low vapor phase concentrations [1]. One approach to the detection of explosives in the vapor phase is analyzing explosive markers with higher vapor pressures, such as explosive by-products [14, 15] or explosive taggants [16]. The identification of these markers can be used to determine the presence of an explosive.

Another approach is to make use of preconcentration devices. In the last decade, several current instrumentation platforms have implemented sampling and preconcentration systems to adapt their technology to vapor analysis [1, 17-19], including samplers with different adsorbent materials [17, 18], solid-phase-microextraction (SPME) [19], and micropreconcentrators packed or coated with adsorbent materials [20-22]. Preconcentration allows the capture of sufficient mass to reach detectable limits in air. Despite the significant improvement in vapor-phase detection with preconcentration, there are still some limitations, such as prolonged analysis time and lack of adequate portability. Thus, there remains the need for a portable instrument that is capable of fast

and accurate analysis of explosives in the vapor phase, yet small, simple, and inexpensive enough to be used for routine monitoring. To address this situation, the use of a field-deployable gas chromatographic microsystem (μGC) suitable for vapor analysis is demonstrated. The advantage of using a μGC system is separation capabilities for a proper identification of the analytes, relatively low-power requirement, small size, simplicity, and high sensitivity. A typical μGC system consists of three essential microfabricated components: a preconcentrator or other injector, a separation column, and a detector. Numerous reports have appeared over the past decade on μGC components [20-34], subsystems [35-37] and systems [38-46].

Here we describe the design, development, assembly, and laboratory characterization of a fully integrated μGC field prototype, dubbed INTREPID, adapted specifically for determinations of explosive markers at very low concentrations in the vapor phase. The description of the main components of the μGC and the application-specific variables that determined the design, configuration, and operating conditions are provided in the next sections. Results demonstrating the performance of the assembled prototype, in terms of analysis time, selectivity and vapor recognition, for the analysis of two explosives markers in vapor-phase: 2,3-dimethyl,2,3-dinitrobutane (DMNB), and 2,4-dinitrotoluene (2,4-DNT) are presented.

3.2. Experimental

3.2.1. Materials

The explosive markers DMNB, 2,6-DNT, and 2,4-DNT were obtained from Sigma-Aldrich (Milwaukee, WI) in > 99 % purity and used as received. Standard solutions of these compounds and TNT were obtained from AccuStandard (New Haven, CT) in 1 mg/L concentrations in methanol/acetonitrile. Alkanes and other organic compounds used as test compounds or

interferences were purchased from Sigma-Aldrich/Fluka or Acros/Fisher (Pittsburgh, PA) in > 99% purity and were also used as received. The graphitized carbons, Carbopack B, Y, and F (C-B, C-Y, C-F, 60/80 mesh, with specific surface areas of 100, 25, and 5 m^2/g, respectively) were obtained from Supelco (Bellefonte, PA). Samples were sieved and the fractions with nominal diameters in the range of 212 – 250 μm were isolated, preconditioned at 350 °C for 6 hours under helium, and packed in the appropriate device.

Thiolate-monolayer-protected gold nanoparticle (MPN) films derived from the following thiolates were used are used as interface layers: octane thiolate (C8), mercapto-6-phenoxyhexane (OPH), 4-mercapto-diphenylacetylene (DPA), and methyl 6-mercapto-hexanoate (HME). Samples were taken from existing stocks of these materials.

3.2.2 Fluidic/analytical components, subsystems, and full system

The layout diagram of the analytical subsystem of the final INTREPID-I lab prototype is shown in Figure 3-1a along with photographs of the key analytical/fluidic components. These include the high-volume sampler (not micro-fabricated), μfocuser (μF), microcolumn, and chemiresistor (CR) array detector that uses nanoparticle interface layers. The high-volume sampler simultaneously reduces analysis time and detection limits. It is a stainless-steel tube (6 cm long, 0.54 cm i.d) with a fine-wire thermocouple and Cu resistive heater coil wrapped around it. It was packed with 50 mg of C-B and was tested to show that it has sufficient capacity for quantitative trapping of the markers while allowing more-volatile interferences to pass through unretained (see Chapter 2; note that this was subsequently replaced with a dual-adsorbent bed of C-B and C-Y upon discovery of residual carryover in the C-B-packed sampler).

Figure 3-2 shows the three different μF devices tested. The larger μF chip has a deep-reactive-ion-etched (DRIE)-Si/glass cavity (3.2 × 3.5 mm) with tapered inlet/outlet, a side port for filling with adsorbent, and DRIE-Si pillars (0.15 mm widths and spaces, 0.38 mm height) near the inlet and outlet ports for retaining the adsorbent granules. An additional flow channel is etched into the chip, forming a tee connection with one of the two main flow channels, to facilitate loading and backflushing of the samples. Evaporated Cr/Au heater contacts and a Ti/Pt RTD are used for controlled thermal desorption/injection by bulk heating (225 °C in 0.6 sec). The μF is packed with a graphitized carbon adsorbent, Carbopack B (C-B, Supelco, Bellefonte, PA) by applying gentle suction to the outlet port through the side port at the side of the cavity. After packing, the filling port is sealed with Duraseal®. Approximately 2 mg of C-B can be packed into the largest μF, as determined gravimetrically. Devices with smaller cavities were filled similarly.

Figure 3-3 shows images of several microcolumns. The 1-cm^2 DRIE-Si/glass microcolumn chip has a 1-m-long channel and integrated heaters and temperature sensors for rapid temperature programming. The design and fabrication have been described previously. Briefly, rectangular channels, 150 × 240 μm are formed by DRIE. Sections of the inlet and outlet ports extending 1 mm in from the edge of the chip are expanded to 350 μm × 250 μm by a second etching step to accommodate the capillary interconnectors. After etching, a Pyrex glass wafer is anodically bonded to the top surface and the microcolumns are then diced from the wafer. Deactivated fused silica capillaries were connected to the inlet and outlet ports with epoxy (Hysol Epoxy patch 1C, Rocky Hill, CT). Microcolumns of similar design were created with channel lengths of 25 cm, 50 cm, and 3 m. Some preliminary testing was performed with the 25-cm-long microcolumns as part of this project.

The PDMS stationary phase was deposited and cross-linked in the column using a static coating method described previously [29]. Briefly, a microcolumn was first filled with a polymeric solution of 0.25% (w/v) of PDMS in a 1:1 mixture of n-pentane and dichloromethane. Dicumyl peroxide (1% by weight relative to PDMS) was added to the solution as a cross-linking agent. The coating solution was added from a reservoir connected to the microcolumn by means of a segment of 250 µm i.d. deactivated fused-silica capillary. The reservoir was pressurized with N_2 gas to force the solution to flow through the column. After filling, the distal capillary was sealed by insertion into a silicone-rubber injection-port septum and the microcolumn was placed in a water bath at 40 ºC. The proximal capillary was connected to a vacuum pump (Model UN 85.3 KTI, KNF, Neuberger, Inc, Trenton, NJ), providing a suction pressure of 20.7 kPa (absolute) to evaporate the solvent. To cross-link the wall-coated film, the microcolumns was filled with H_2 gas, sealed with a septum, heated from 160 to 180 ºC at 0.2 ºC/min, and then held at 180 ºC for 60 min. This results in a nominal film thickness of 0.15 µm, calculated from the concentration of the polymeric solution. Deactivation (capping) of surface silanol groups on the walls of the channel was achieved by passing vapors of hexamethyldisilazane (HMDS) through the column after PDMS deposition at 120 ºC for 6 hr.

The detector is an 8-element chemiresistor (CR) array, having individual interdigital electrodes with 24 finger pairs (0.5 mm length; 5 µm widths and spaces). Design and fabrication have been previously described [47]. Solutions of the MPNs (~5 mg/mL) were dissolved in appropriate solvents and deposited by microliter syringe. Films of each type of MPN were coated on two CRs but only one of each was used in this study. Post-coating baseline resistances were in the range of 0.5–10 MΩ. The array was capped with a Macor® lid sealed with VHB tape (volume ~3 µL) and fitted with capillary interconnections.

Figure 3-1b shows a top view of the core components of the final INTREPID I lab prototype. The assembled prototype has dimensions of 37 (w) × 22 (d) × 20 cm (h) and weighs 4 kg. The MEMS components are mounted and wire-bonded on separate custom printed circuit boards (PCBs) suspended from the (heated) chamber floor by standoffs and interconnected with deactivated fused-silica capillaries (0.25-mm i.d.,0.32-mm o.d.) via press-fit connectors. Leads from the PCBs are fed through the chamber wall to a wire harness mounted on the underlying electronic control board. The 8-L chamber has resistor-embedded polymer-film heaters (SRFR-5/5-P, Omega, Stamford, CT) on its walls and it is heated so that the components are maintained at 70-80 °C to reduce adsorptive losses on interconnection surfaces and to increase the rate of sorption/desorption in the MPN films on the CR array. A double-header diaphragm pump (D737B, Parker, Cleveland, OH) is used for sample collection. Scrubbed ambient is used as the carrier gas and is drawn through the system via a second mini-diaphragm (analysis) pump (E155, Parker, Cleveland, OH) during analysis. A scrubber, packed with charcoal and molecular sieves, is connected to the analysis pump to remove VOCs and water vapor. Four solenoid valves (NResearch, West Caldwell, NJ) and two latching valves (Lee Co., Westbrook, CT) are used to direct flow. Custom electronic control PCBs and DAQ boards are mounted beneath the microsystem and connected to the laptop via a USB port.

The system functions are controlled automatically by a laptop computer running routines written in-house in LabVIEW 8.6 (National Instruments, Austin, TX). The instrument proceeds through a sequence of three modes: sampling, focusing and analysis. The flow paths are depicted in Figure 3-4 for each mode. In Sample Mode, air is drawn by the sample pump through the sampler at 3 L/min for 30 sec (1-L target sample volume; ultimately changed to 3 L/min for 20 sec). In Focus Mode, vapors collected in the sampler are pushed by the sample pump at 55 mL/min and thermally

released at 250 °C to the μF for 60 sec (ultimately changed to 40 mL/min for 40 sec). In Analysis Mode, scrubbed ambient air is drawn in by the analysis pump, the μF is heated, and the analytes are backflushed at 1.2 mL/min onto the microcolumn for separation and detection by the CR array (ultimately increased to 3 mL/min).

3.2.3. Testing

For most tests, saturated test atmospheres of the marker compounds were prepared in a 3-L FlexFilm bag (SKC, Eighty-Four, PA) in N_2 and then aliquots were transferred by gas-tight syringe to a series of other bags to span a range of concentrations. A bench-scale GC with ECD or FID was used to confirm masses injected. For other tests, standard solutions were prepared in a volatile solvent and injected manually or by auto-injector through the injection port of a bench scale GC (Model 6890, Agilent Technologies, Palo Alto, CA).

Preliminary μF capacity testing employed test atmospheres of DMNB drawn continuously through the μF at different flow rates and bed masses. Aliquots were taken from a downstream tee connector and injected into the GC with a short capillary column and an ECD to measure fractional breakthrough. In subsequent experiments, the μF was mounted inside the GC oven and connected with deactivated capillary to the side-port of the sampler and to the Y-connector leading to an FID. The effluent from the μF was monitored at different sampler desorption flow rates, baseline (oven) temperatures, and spiked quantities of the markers and interferences on the sampler.

3.2.4. Control hardware and software

Custom PID algorithms, incorporated into the LabVIEW code, were used in conjunction with pulse-width-modulation (PWM) of DC voltages applied to the integrated device heaters for controlling the μF and microcolumn temperatures during thermal desorption and temperature-programmed separations, respectively. A DC bias of 3 V was applied to each sensor from either a power supply or a battery. A suitable amplifier circuit, designed in-house, was used to convert the CR resistance change into a DC voltage, which was measured by a USB-interfaced DAQ via an in-house written LabVIEW control sub-routine

Figure 3-5 shows a photograph of the initial μF control/heating setup, including a programmable DC power supply and two digital multimeters. The DC power supply applies a constant voltage to device for heating, and multimeters measure heater voltage and current to calculate the power value. A similar set-up was used for initial testing of microcolumn temperature programming control functions.

3.3 Results and Discussion

3.3.1. Microfocuser test

Most of the capacity and thermal desorption μF testing was described in Chapter 2. In this chapter, a more in-depth characterization of the μF controller is presented. Figure 3-6 shows μF temperature and resistance variations when biased with a DC voltage. Initially, the resistance of the integrated heater increased as the Si substrate temperature increased. When the temperature reached 140 ^{o}C, in this case, the heater resistance began to dramatically decrease from 1.43 kohm to 40 ohm as the silicon went “intrinsic” (transition from semiconductor to conductor). Figure 3-7

shows the temperature profile of the μF under PID control. Initially, the voltage applied to the heater was set at 60 V and the current limit was set at 500 mA. When the μF temperature is higher than semiconductor-to-conductor transition temperature, the resistance of the heater decreases dramatically, and the DC power supply converts to constant current mode and current was set at 290 mA. With this method, the temperature of μF rises to 300 °C in 7 sec and can be maintained at 300 ^{o}C indefinitely. Subsequently, the heating rate was increased dramatically so that the device could be heated to 225 °C in 0.6 sec (i.e., at 375 °C/s). Figure 3-8 shows the power dissipation profile when heating the μF. Before the transition temperature, the power dissipation is < 4 W. When the μF temperature rises to the transition temperature, this increases to 15 W but then decreases back to 4 W because the programmable DC power supply is switched from constant voltage mode to constant current mode. To keep μF at 300 ^{o}C requires only 2.5 W.

3.3.2 Chemiresistor testing and signal processing options

Figure 3-9 shows the circuit used to acquire signals from the CR sensors. Through the operational amplifier, the circuit is designed to convert the CR resistance value to a voltage and then to amplify the difference between voltage signals with and without low pass filter. Figure 3-10 shows the voltage shift obtained from a C8-coated CR sensor mounted at the outlet of a 5-m long commercial capillary column in a bench-scale GC upon injection of 0.01 μL neat-liquid n-octane sample with a 100:1 split ratio at a He flow rate of 1 mL/min. The peak height is about 0.55 V. Compared with the signal without amplifier, the gain of amplifier is about 100. To avoid manual tuning before every measurement, an alternate amplification scheme was considered, whereby the CR voltage signal from a half-Wheatstone bridge circuit was amplified by an instrument amplifier. As above, to create a dynamic reference voltage, the CR voltage signal was

connected to a low pass filter. With this circuitry, the ratio of resistance change due to vapor exposure to the baseline CR resistance is obtained by: $\Delta R/R=3*(V_2/G)/(2-V_1)$, where G is the gain of instrument amplifier.

To establish an estimate of the sensitivity of the CR sensors to the marker compounds, a calibration of the C8-coated CR was performed for 2,6-DNT by serial injection of increasing masses of 2,6-DNT. Figure 3-11 shows that the response is a linear function of injected mass over the range tested. By assuming a sample volume of 1 L, it is possible to convert the injected mass into an equivalent air concentration or, more generally, to an equivalent injection volume in units of ppb-L. In anticipation of operating the CR array at elevated temperature, this calibration was performed by maintaining the sensor at 70 °C. As shown, it is possible to measure 1 ng and the projected limit of detection (LOD) is 0.26 ng, corresponding to 35 parts-per-trillion (ppt) in 1 L. This result established that a 1-L sample volume would be sufficient to detect the markers at sufficiently low air concentrations with the INTREPID I prototype even when heating the sensors to as high as 70 °C.

3.3.3. Microcolumn evaluation and optimization

The PDMS-coated microcolumn was evaluated using n-octane (retention factor, k' = 2.5) as the probe vapor at 30 ºC with air as carrier gas. A split-mode injector was used to inject 2.5 µL headspace samples with a split ratio of 1000:1. Chromatograms were generated over a range of linear velocities by adjusting the inlet pressure. To assess efficiency, values of *N* (number of theoretical plates) were calculated at each linear velocity by the well-known expression, $N = 5.54(t_R/W_{0.5})^2$, where t_R is the adjusted (i.e., methane-normalized) retention time and $W_{0.5}$ is the full width at half-maximum (*fwhm*) of the peak. From these *N* values, the corresponding values of

H (minimal plate height) were calculated. A plot of linear velocity versus *H* (i.e., a Golay plot) was generated and the values of H_{min} and the corresponding optimal linear velocity, u_{opt}, were determined using a polynomial model.

Figure 3-12a presents the Golay plot for the 1-m PDMS-coated column with air as carrier gas. The N value evaluated at the minimum of the Golay plot is 4400 plates/m. This result demonstrates the efficiency of the static coating method to coat DRIE/Si microcolumns (typical commercial fused-silica capillary columns generate 4800-5000 plates/m). The optimal volumetric flow rate (*F*) was 0.2 mL/min under these conditions. Although wall deactivation is not necessary for achieving good separations of non-polar compounds, polar compounds such as nitro-aromatics interact with the untreated wall surface, leading to significant peak tailing. Treatment with HMDS is an effective remedy. As shown in Figure 3-12b, the peak obtained from injecting the same quantity of TNT (CS_2 solution) into the column after HMDS treatment is ~3 times higher than that obtained prior to treatment. The HMDS treatment had no effect on the peak shapes of non-polar compounds or on the total number of plates. Figure 3-13 shows results of early tests designed to establish conditions for separating 2,4-DNT from n-alkanes that elute in the vicinity of the 2,4-DNT using 25-cm-long and 1-m-long microcolumns connected to a benchscale GC injector and FID. As shown, reasonably good resolution can be obtained with the 25-m microcolumn and the separation is completed much more rapidly than with the 1-m microcolumn at the same (isothermal) temperature. Regardless of the column length, partial co-elutions appear to be inevitable. However, by use of pattern recognition methods such as multivariate curve resolution, it should be possible to deconvolute such composite peaks and to determine the presence and quantity of the 2,4-DNT.

The LabVIEW temperature control program repeats the following three steps in sequence: (a) calculate the average of 100 temperature readings in 100 ms; (b) calculate the peak-width modulation (PWM) amount for heater output using PID algorithm; (c) heat the microcolumn controlled by PWM in 256 msec. By iterating these three steps the microcolumn temperature can be set to a specified temperature (i.e., isothermal separation) or stepped through a series of temperatures (i.e., temperature programmed separation).

Table 3-1 shows the reliability of the temperature ramped microcolumn using retention time as the indicator. In five serial injections with the same temperature ramp, 120 ^{o}C, 2^{o}C/sec to 140^{o}C, 1.5^{o}C/sec to 170 ^{o}C (30sec), the standard deviations of the retention times were < 0.5 sec for all 7 compounds: CS_2, C_{14}, 2,6-DNT, C_{15}, 2,4-DNT, C_{16}, and TNT. Figure 3-14 shows chromatograms demonstrating the separation of 2,4-DNT, 2,6-DNT and TNT from C_{14}-C_{16} alkanes, used as models of potentially interfering fuel compounds. The analysis was performed at 160 ºC using a conventional GC oven, and then with the on-board (integrated) heaters and temperature sensors controlled by two different temperature control circuits. The LabVIEW controller provided excellent performance. Figure 3-15a shows two sequential linear temperature ramps at 30 °C/min and 60 °C/min with three isothermal intervals at 70 °C, 90 °C and 120 °C generated by the controller, illustrating the capabilities for precise temperature control of the microcolumn. The chromatogram in Figure 3-15b shows a temperature-programmed separation of a mixture of 2,4-DNT, 2,6-DNT, TNT and 6 n-alkanes of comparable volatility in < 40s. A 100:1 split injection of a 0.1-µL sample of the mixture in solution was used. The sharpness, symmetry, and resolution of the peaks in the chromatograms shown in Figures 3-15 and 3-16b demonstrate the efficiency of the microcolumn, which results from deposition of a uniform stationary phase layer and deactivation of the channel walls.

3.3.4. Microcolumn and CR array integration

Along with the advantage of using MPN-coated CR-array detector to generate response patterns for each target analyte and discriminate one from another, is the challenge of generating sharp peaks; the finite dead volume of the detector and the kinetics of reversible sorption into the MPN films lead to peak broadening. Figure 3-16 shows the separation of 2-nitrotoluene and 2,6-DNT from n-tridecane (C13), n-tetradecane (C14) and n-pentadecane (C15), using the 1-m microcolumn and a single CR sensor coated with a film of C8-MPN as the detector. The sensor and the column were both heated to 100 °C in the GC oven. Although the peaks are rather broad and somewhat distorted, the separation is effective and is achieved in ~75 sec. Notably, the MPN films are responsive (in air) even at this elevated temperature, although subsequent testing revealed that the sensor suffers losses in sensitivity over time at this temperature due to film decomposition.

3.3.5. Preliminary system integration efforts

Figure 3-17 is the printed circuit layout diagram for the early INTREPID I microfluidic subsystem depicted in Figure 3-18. Additional modifications were made, ultimately, but this illustrates the different layers and routings of the printed circuits as well as the locations of all components used. Based on this diagram, the PCB was fabricated and populated with all necessary components. Figure 3-19 shows the board with the mounted devices. Testing performed with this early prototype revealed that the 2-way valves were unreliable that wall adsorption was significant along the flow paths, and that it would be necessary to mount each of the key microsystem components on separate PCBs to facilitate switching components in and out during the development effort. These results led to the conclusion that a different layout would be necessary and that the entire

subsystem should be housed in a heated enclosure to avoid adsorptive losses and band broadening of the marker compounds, and to enhance the rejection of less volatile interferences in the μF, the microcolumn, and the CR array.

Figure 3-20 shows a revised layout diagram with the microanalytical subsystem components on separate PC boards. This design was used in the final version of the INTREPID I prototype (Figure 3-21). One pump is used for sampling and the other for analysis. The entire microanalytical subsystem, as well as the inlet valve, were housed within the mini-oven.

3.3.6. INTREPID I calibration and testing

Figure 3-22 summarizes the LabView control functions and is presented to emphasize the importance of the software development effort in creating a functional semi-autonomous laboratory prototype. The current program is specific to the INTREPID I prototype and provides control of the microfabricated components, and data acquisition and display of the microsensor array output signals. A separate program was used for valve and pump actuation for INTREPID I. Figure 3-23 presents calibration curves (peak height vs. conc.) for the 3 targets generated from the INTREPID lab prototype subsystem (μF, 1-m μcolumn, CR-sensor) with samples spiked onto the μfocuser and analyzed under near-optimal conditions, keeping the desorption/separation flow rate at 1.2 mL/min, and the baseline temperature of the μfocuser and CR sensor at 70 °C, and 1-m μcolumn at 110 °C. The curves are quasi-linear over the concentration ranges tested for all sensor-analyte combinations with zero y-axis intercepts. LODs (calculated via 3σ/sensitivity, where σ is the standard deviation of the baseline noise), were 5.4, 0.22 and 0.27 ppb for DMNB, 2,6-DNT, and 2,4-DNT, respectively, on the basis of the most sensitive sensor in the array. These correspond to 39, 1.6, and 2.0 ng, respectively, for a 1-L sample volume. LODs are somewhat

higher if full response patterns are necessary.

Table 3-2 presents the vapor pressure, retention time (t_R), sensitivity, and LOD for each marker. For a given sensor, the relative sensitivities among the markers follow the trend expected for sorption-dependent sensors, with sensitivity generally increasing with decreasing vapor pressure of the analyte. HME was the most sensitive sensor for 2,6-DNT and 2,4-DNT, consistent with the greater dipolarity of the HME ester functional group. Surprisingly, the C8-coated sensor had the highest sensitivity toward DMNB. LODs generally decrease with increasing sensitivity toward the analyte, but this parameter is also affected by the base line noise level, which differed for each sensor. One of the primary advantages of sensor array detection is the use of the response patterns to aid in identifying analytes and differentiating analytes that might partially co-elute from the separation column. Figure 3-24 shows relative response patterns obtained for the three markers and the n-tridecane (C13) interference from the peak heights measured for the individual components. Response patterns for 2,4- and 2,6-DNT are quite similar but differentiable, while that for DMNB is unique. The pattern for C13 is quite different from those of all of the markers, as expected.

3.3.7. Mixture analysis

The optimal flow rates for desorption (narrowest injection band), separation (best separation efficiency) and sensor response (peak height and peak width) were found to differ, requiring a tradeoff in performance. Reconciling flow rates is one of the challenges for effective microsystem integration. For example, the optimal flow rate for chromatographic efficiency is 0.2 mL/min, and this flow rate also yields large responses from the sensor array. However, this flow rate leads to very broad injection bands from the μF and also to broader peaks in the detector, both

of which degrade resolution. Tests performed over a range of flow rates from 0.2-2 mL/min showed that 1.2 mL/min provided the best compromise among these factors. Subsequent testing led to the decision to increase the analytical flow rate to 3 mL/min (see Chapter 2).

Figure 3-25 shows the chromatograms of a mixture of DMNB, 2,6-DNT, 2,4-DNT, and C13 obtained with the full microsystem for spiked samples of 50-75 ~ng quantities of each target in a mixture with C13, which served as a representative fuel interference. The values of chromatographic resolution are 1.5 (DMNB/C13), 1.9 (C13/2,6-DNT) and 0.82 (2,6-DNT/2,4-DNT), and the separation is complete in 120 sec (90 sec for last analyte peak maximum to elute) despite the rather broad peaks for the DNT isomers. This degree of separation is sufficient for determining the markers, particularly when the response pattern data is considered. Thus, the overall analysis, considering also the sampling and focusing time, requires 3.5 min. In order to demonstrate retention-time stability, two sensor arrays coated with all four MPN films were tested under the same conditions: oven temperature set at 80 °C, column temperature isothermal at 110 °C, and inlet pressure set at 1.4 psi. Figure 3-26 shows the results demonstrating that retention times are highly reproducible.

3.3.8. Redesign electronics board with reduced baseline noise/drift

In the course of these tests of the INTREPID I prototype, a flaw in the amplification method employed was discovered, which resulted in some sensor channels being unusable due to a large sinusoidal drift pattern that swamps out the sensor reading. We determined that this is due to the use of a single-stage amplifier that does not filter extraneous noise. Resolving this problem was relatively straightforward, requiring a board redesign with an alternate approach to sensor

amplification. This issue, as well as a mean for adjusting the dynamic range of each sensor readout circuit, was addressed in the revisions made for the INTREPID II prototype.

Prior to designing the new electronics boards for the improvement of baseline stability and dynamic range, additional testing of the INTREPID boards was performed to analyze better the sinusoidal drift pattern and to track down the source of this noise. We found that the source was in fact a 60 Hz signal that was easily coupled from the power lines to the front-end of the sensors circuit, mainly due to the high impedance of the sensors transmission lines. However, since the frequency of the noise was found too close to the sensors response bandwidth, we thought that the introduction of an additional analog filtering stage could lead to a modification in the sensors response measured by the circuit. Thus, instead of modifying the sensor amplification circuit we decided to address the issue by eliminating the noise from the source by the following means: providing a good connection between signal ground and earth ground to reduce inductive and capacitive coupling, powering the sensors with 60Hz-noise-free batteries, entirely shielding the sensors and sensors transmission lines, and finally isolating the signal ground from the rest of the electronic circuit grounds.

We also further improved the baseline stability, and consequently the dynamic range of the circuit, by modifying certain parameters in the amplification circuits. Since the largest contribution to the baseline noise is localized before the amplification stage, by decreasing the gain of the amplifier stages the high resolution of the digital acquisition board can be exploited. Furthermore, by making the gain setting resistors interchangeable, we will be able to maximize signal strength for each channel independently and according to the amplification requirements of each sensor. Another issue that impacted the limits of detection of the sensors is the voltage output dependence on sensor baseline resistance. According to the transfer function of the amplifier

circuits, we estimate that shifts in the sensor baseline resistances were leading to a decrease in sensitivity of up to 3 fold. We found, however, that we could maximize this sensitivity by matching the reference resistors with the sensors baseline resistance. For this purpose a set of resistor sockets was added to the circuit board for manual replacement of the reference resistor during instrument calibration.

Review of the previous circuitry and components used indicated that some components used needed to be upgraded to more "robust" types (tighter tolerances, etc.). All components in question were upgraded in the INTREPID II prototype. A circuit board for conditioning and amplification of sensor signals was developed in light of the findings described immediately above, as well as the size constraints of the INTREPID II prototype. The signal conditioning stage was tested and debugged using fixed resistors for simulating sensor impedances. With the present circuit configuration a baseline noise of +/- 14 mV was measured on the amplified signal over a time window of 2.5 minutes. In the case of the buffered signals, a baseline noise of +/- 0.5 mV was achieved (see Figure 3-27).

As an additional component part of the development of the electronics circuits of INTREPID II system, the circuit board that controls the fluidic components of the system was redesigned to meet the new power and voltage requirements of pumps, valves and heaters used in the new system. More I/O lines were added for monitoring and controlling the temperature of the oven. To achieve the requirements of sampler heating rate, the applied voltage pulse to the sampler was increased and a second voltage regulator was added for stabilization of the sampler temperature at steady state. Voltage regulators and relays with higher current capacity were chosen, however after testing of the control board, it was found that one of the regulators was suffering of overheating. To solve this problem, the voltage regulator was replaced with one of

higher efficiency and thus capable of handling the required power. Test and debug on the circuit boards were completed for the following functions: Pumps and valves control; μF temperature control and monitoring, including initial temperature function; μcolumn temperature control and monitoring; CR sensors environmental temperature monitoring; CR sensor data acquisition using fixed resistors; Sampler temperature monitoring.

3.4. Conclusions

In summary, a functional μGC laboratory prototype, INTREPID I, has been assembled and tested that consists of the fluidic/analytical and electronic hardware subsystems, software for controlling the key components of the system and acquiring data from the sensor array, and data management approaches for identifying and quantifying the target analytes and differentiating them from typical interferences. This is the first demonstration of a fully integrated μGC lab prototype for rapid determinations of explosive markers. Results show that the explosive marker compounds DMNB, 2,6-DNT and 2,4-DNT can be captured, focused, injected, separated, and detected at concentrations in the low- or sub-ppb range with a 1-L air sample in less than 3.5 minutes. Relative response patterns obtained with the MPN-coated CR array detector are unique for target vapors and can be used with chromatographic retention time to improve the reliability of marker determinations. This MEMS-based microsystem is a step forward in the development of small, inexpensive, instrumentation for homeland security applications.

These promising results are being used to guide several design modifications to be incorporated in the next-generation system, INTREPID II. The sampling time is being reduced by operation at a higher sampling flow rate. The time required for focusing is also being reduced similarly. Reductions in the injection bandwidth, use of on-column focusing, and high-speed

temperature programming are being implemented to improve chromatographic resolution, which will reduce elution time. Use of localized heating mechanisms will reduce the footprint and power dissipation of this system as well.

3.5. References

1. D. S. Moore, *Rev. Sci. Instrum.*, 75, (2004), 2499 - 2513
2. L. Thiesan, D. Hannum, D. W. Murray, J. E. Parmeter, Survey of commercial available explosives detection technologies and equipment, available at https://ncjrs.gov/pdffiles1/nij/grants/208, accessed August 2012
3. J. Yinon, *Trac-Trends Anal. Chem.*, 21, (2002), 292-301.
4. N. L. Sanders, S. Kothari, G. M. Huang, G. Salazar, R. G. Cooks, *Anal. Chem.*, 82, (2006), 5313-5316.
5. R. G. Ewing, D. A. Atkinson, G. A. Eiceman, G. J. Ewing, *Talanta*, 54, (2001), 515-529.
6. C. C. Harb, T. K. Boyson, A. G. Kallapur, I. R. Petersen, M. E. Calzada, T. G. Spence, K. P. Kirkbride, D. S. Moore, *Optic Express*, 20, (2012), 15489-15502
7. B. Zachhuber, G. Gasser, G. Ramer, E. T. H. Chrysostom, B. Lendl, *Applied Spectroscopy*, 66, (2012), 875-881.
8. Fido XT, FLIR ICx, available at www.icxt.com/uploads/file/products/ brochures/ Fido_XT.pdf, accessed August 2012.
9. Y. Xin, G. He, Q. Wang, F. Yang, *Rev. Sci. Instrum*, 82, (2011), 103102.
10. HAPSITE ER, Inficon, available at http://www.inficonemergencyresponse.com/en/hapsite_er//index.html, accessed May 2012.
11. A. P. Synder, C. S. Harden, A. H. Brittain, M. G. Kim, N. S. Arnold, H. L. C. Meuzelaar, *Anal. Chem.*, 65, (1993), 299-306.
12. M. Williams, J. M. Johnston, M. Cicoria, E. Paletz, L. P. Wagoner, C. C. Edge, S. F. Hallowell, *Proc. SPIE*, 3575, (1998), 291-301.
13. S. Wallin, A. Pettersoon, H. Ostmark, A. Hobro, *Anal. Bioanal. Chem.*, 395, (2009), 259-274.
14. T. F. Jenkins, D. C. Leggett, T. A. Ranney, CREEL, special report 99-21, 1977.
15. R. P. Murrmann, T. F. Jenkins, D. C. Leggett, CREEL, special report 158, 1971.
16. Convention on the marking of plastic explosives for the purpose of detection, available at http://www.ciaonet.org/cbr/cbr00/video/cbr_ctd/cbr_ctd_33.html, accessed August 2012.
17. K. L. Linker, F. J. Conrad, C. A. Custer, C. L. Rhykerd Jr., Sandia National Laboratories, Particle Preconcentrator, U.S. Pat. 6,085,601, 2000.
18. R. Ingram, J. Sikes, *Proc. SPIE*, 7664, (2010), 766415-1 – 766415-8
19. H. Lai, A. Leung, M. Magee, J. R. Almirall, *Anal. Bioanal. Chem.*, 396, (2010), 2997-3007.
20. I. Voiculescu, R. A. McGill, M. E. Zaghloul, J. Stepnowski, S. Stepnowski, H. Summers, V. Nguyen, S. Ross, K. Walsh, M. Marin, *IEEE Sensors*, 6, (2006), 1094-1104.
21. M. Martin, M. Crain, K. Walsh, R. A. McGill, E. Houser, J. Stepnowski, S. Stepnowski, H-D Wu, S. Ross, *Sens. Actuators B*, 126, (2007), 447-454.

22. E. H. M. Camara, P. Breuil, D. Briand, N. F. de Rooij, C. Pijolat, *Anal. Chim. Acta*, 688, (2011), 175-182.
23. W. C. Tian, H. K. L. Chan, C. J. Lu, S. W. Pang, E. T. Zellers, *J. Microelectromech. Syst*., 14, (2005), 498-507.
24. R. P. Manginell, D. R. Akins, M. W. Moorman, R. Hadizadeh, D. Copic, D. A. Porter, J. M. Anderson, V. M. Hietala, J. R. Bryan, D. R. Wheeler, K. B. Pfeifer, A. Rumpf, *J. Microelectromech Syst.*, 17, (2008), 1396-1407.
25. B. Alfeeli, D. Cho, M. Ashraf-Khorassani, L. T. Taylor, M. Agah, *Sens. Actuators B*, 133, (2008), 24-32.
26. S. Reidy, G. Lambertus, J. Reece, R. Sacks, *Anal. Chem*., 78, (2006), 2623-2630.
27. A.D. Radadia, R.I. Masel, M.A. Shannon, J.P. Jerrell, and K.R. Cadwallader, *Anal. Chem*., 80, (2008), 4087- 4094.
28. M. A. Zarejan-Jahromi, M. Ashraf-Khorassani, L. T. Taylor, M. Agah, *J. Microelectromech. Systems*, 18, (2009), 28-37.
29. G. Serrano, S. M. Reidy, E. T. Zellers, *Sens. Actuators. B.*, 141, (2009), 217-226.
30. R-S. Jian, R-X. Huang, C-J. Lu, *Talanta*, 88, (2012), 160-167.
31. X. Y. Mu, E. Covington, D. Rairigh, C. Kurdak, E. T. Zellers, A. J. Mason, *J. IEEE Sensors*, 12, (2012), 2444-2452.
32. M. Li, E. B. Myers, H. X. Tang, S. J. Aldridge, H. C. McCaig, J. J. Whiting, R. J. Simonson, N. S. Lewis, M. L. Roukes, *Nano Letters*, 10, (2010), 3899-3903.
33. S.-J. Kim, G. Serrano, K. D. Wise, K. Kurabayashi, E. T. Zellers, *Anal. Chem.*, 83, (2011), 5556-5562.
34. G. Serrano, D. Paul, S-J. Kim, K. Kurabayashi, E. T. Zellers, *Anal. Chem*., 84, (2012), 6973-6980.
35. G.R. Lambertus, C.S. Fix, S.M. Reidy, R. Miller, D. Wheeler, E. Nazarov, R.D. Sacks, *Anal. Chem*., 77, (2005), 7563-7571.
36. G. Serrano, H. Chang, E. T. Zellers. *Proc. Transducers 09'*, Denver, Co, USA, June 2009, pp. 1654-1657.
37. S.K. Kim, H. Chang, E. T. Zellers, *Proc. Transducers 09'*, Denver, Colorado, USA, June 21-25, 2009, pp. 719-723.
38. S. K. Kim, D. R. Burris, H. Chang, J. Bryant-Genevier, E. T. Zellers, *Environ. Sci. Technol.*, 46, (2012), 6065-6072.
39. S. K. Kim, D. R. Burris, H. Chang, J. Bryant-Genevier, K. A. Gorder, E. M. Dettenmaier, E. T. Zellers, *Environ. Sci. Technol.*, 46, (2012), 6073-6080.
40. S. K. Kim, H. Chang, E. T. Zellers, *Anal. Chem.*, 83, (2011), 7198-7206.
41. E. T. Zellers, G. Serrano, H. Chang, and L. K. Amos, *Proc. Transducers 11'*, Beijing, China, June 5-9, 2082-2085.
42. C. J. Lu, W. Steineker, W. C. Tian, M. Oborny, J. Nichols, M. Agah, J. Potkay, H. Chang, J. Driscoll, R. Sacks, K. Wise, S. Pang, E. T. Zellers, *Lab Chip*, 5, (2005), 1123-1131.
43. P. R. Lewis, R. P. Manginell, D. R. Adkins, R. J. Kottenstette, D. R. Wheeler, S. S. Sokolowski, D. E. Trudell, J. E. Byrnes, M. Okandan, J. M. Bauer, R. G. Manley, G. C. Frye-Mason, *IEEE Sensors*, 6, (2006), 784-795.
44. S. Zampolli, L. Elmi, F. Mancarella, P. Betti, E. Dalcanale, G. C. Cardinali, M. Severi, *Sens. Actuator B*, 141, (2009), 322-328.
45. J. Liu, N. K. Gupta, K. D. Wise, Y. B. Gianchandani, X. D. Fan, *Lab Chip*, 11, (2011), 3487-3492.

46. R. P. Manginell, J. M. Bauer, M. W. Moorman, L. J. Sanchez, J. M. Anderson, J. J. Whiting, D. A. Porter, D. Copic, K. E. Achyutan, *Sensors*, 11, (2011), 6517-6532.
47. W. H. Steinecker, M. Rowe, A. Matzger, E. T. Zellers, *Proc. Transducers 03'*, Boston, MA, USA, June 2003, pp. 1343-1346.
48.
49. M. P. Rowe, K. E. Plass, K. Kim, C. Kurdak, E. T. Zellers, A. J. Matzger, Single-phase synthesis of functionalized gold nanoparticles, *Chem. Mater*., 16, (2004), 3513-3517.
50. G. Serrano, T. Sukaew, E. Zellers, Hybrid preconcentrator/focuser module for determinations of TNT marker compounds with a micro-scale gas chromatograph, *J. Chrom. A,* 2012*, accepted*.
51. C-J. Lu, E. T. Zellers, Multi-adsorbent preconcentration/focusing module for portable-GC/microsensor-array analysis of complex vapor mixtures, 127, (2002), 1061-1068.

Table 3-1. Average and standard deviation of the retention time (min, n = 5) for 7 test compounds with the 1-m microcolumn using on-board heaters and temperature sensors (temp. program given in the text).

	CS_2	C_{14}	2,6-DNT	C_{15}	2,4-DNT	C_{16}	TNT
1st	0.1302	0.2583	0.288	0.3110	0.342	0.377	0.5029
2nd	0.1305	0.2597	0.288	0.3107	0.3401	0.3745	0.496
3rd	0.142	0.2667	0.2964	0.3195	0.3482	0.3892	0.50305
4th	0.1392	0.2561	0.2855	0.3114	0.3397	0.3756	0.4943
5th	0.1422	0.2642	0.2945	0.3139	0.3458	0.3794	0.5157
Avg.	0.13682	0.261	0.29048	0.3133	0.34316	0.37914	0.50239
Std.	0.00602	0.00435	0.0047	0.0037	0.0037	0.0059	0.0084

Table 3-2. INTREPID I response data for the marker compounds.

Vapor	p_v (mtorr)	t_R (s)	Sensitivity (LOD)[a]			
			C8	DPA	OPH	HME
DMNB	2.1	15	12 (39)	6 (47)	11 (43)	7 (52)
2,6-DNT	0.96	60	19 (10)	17 (16)	33 (13)	80 (1.5)
2,4-DNT	0.48	90	19 (8.0)	18 (19)	45 (12)	106 (2.0)

[a] sensitivities measured as peak height are in units of mV/ng and LODs are in ng

[b] conditions: μF T_{max} = 225 °C; sensor array temperature: 70 °C; flow rate: 1.2 mL/min, microcolumn temperature 110°C. Data generated with sensor array integrated with μF and 1-m microcolumn. p_v is the vapor pressure, t_R is the retention time.

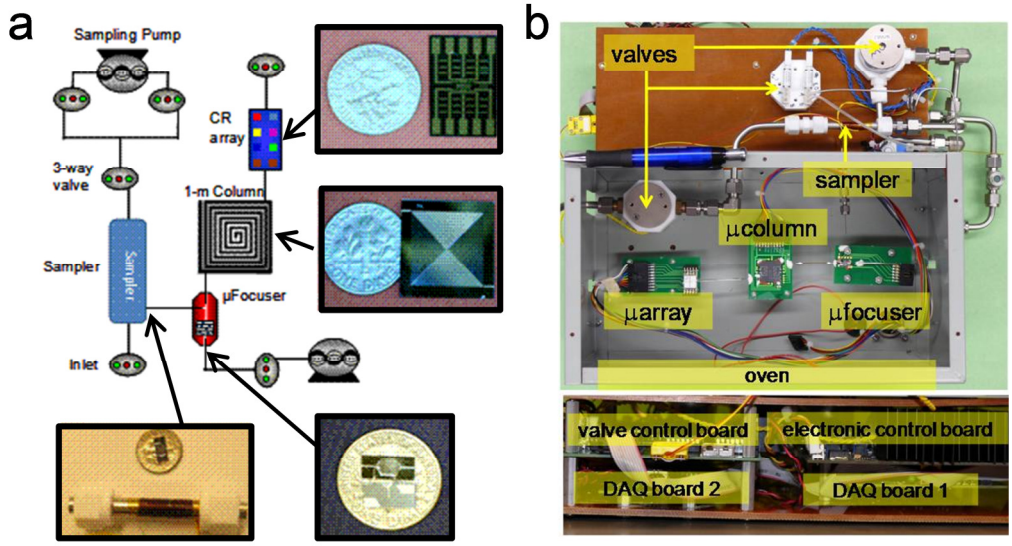

Figure 3-1. (a) Layout of the INTREPID analytical subsystem, showing photographs of the sampler, µfocuser, 1-m µcolumn, and µsensor array; (b) top view of INTREPID prototype micro-analytical subsystem, and side view of electronic data acquisition, control, and DAQ boards lying beneath the analytical subsystem.

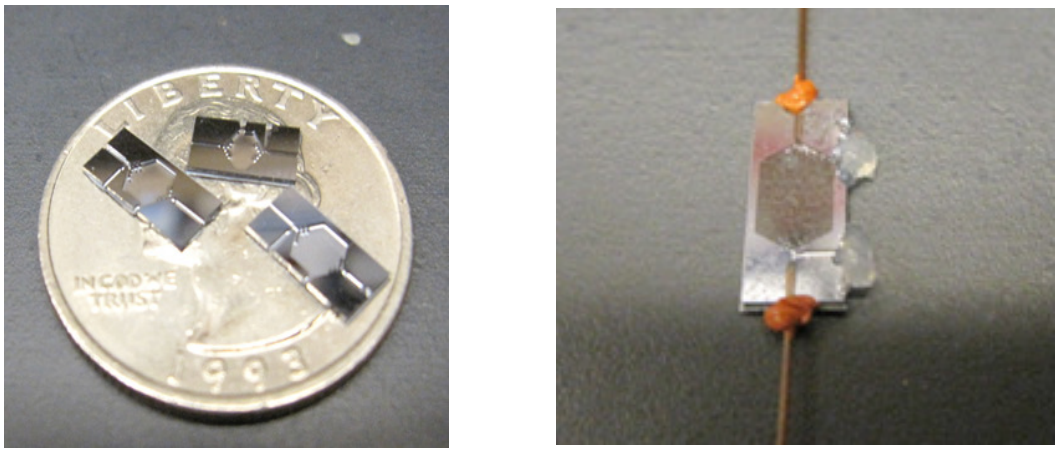

Figure 3-2. (left) DRIE-Si μF devices of three different sizes on a U. S. quarter. The devices all have etched channels for fluidic interconnections and etched cavities with pillars near the inlets and outlets that retain the C-B adsorbent particles. Contacts for bulk heating are on the backside. The largest device (lower right) was used in the INTREPID I prototype; (right) Large μF packed with C-B, fitted with capillary interconnects, and sealed with epoxy.

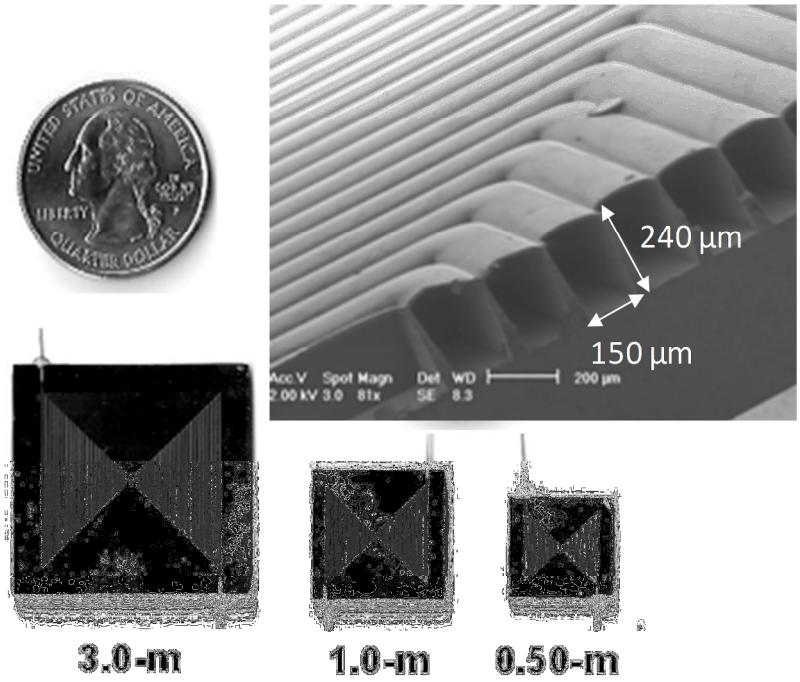

Figure 3-3. Images of several Si/Pyrex microcolumns and a U. S. quarter. The SEM image is a cut-away showing the cross section of the channels (25-cm microcolumn not shown).

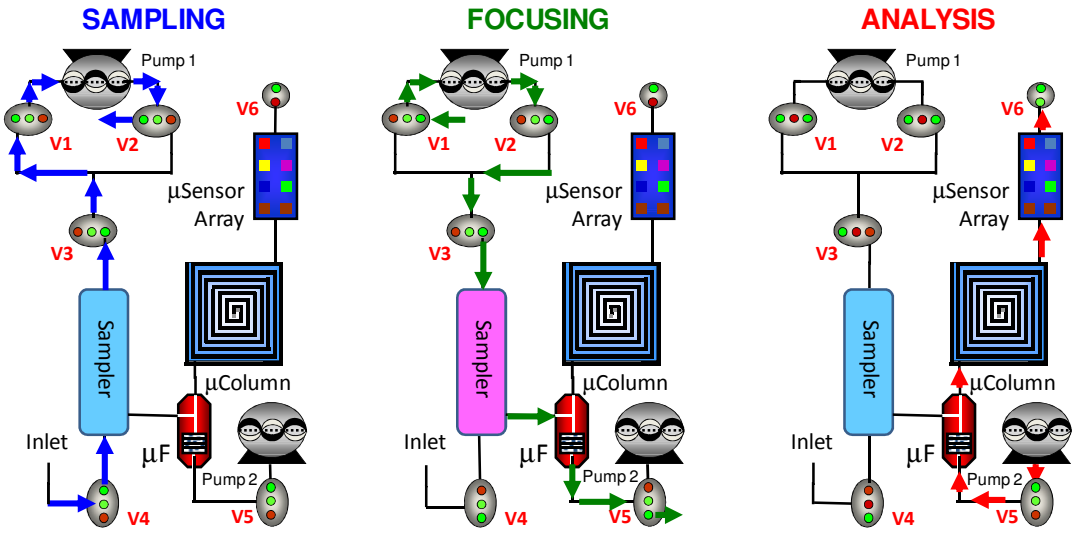

Figure 3-4. Layout diagram of the INTREPID I lab prototype, showing the flow path in each of the three primary operating modes: Sampling, Focusing, and Analysis.

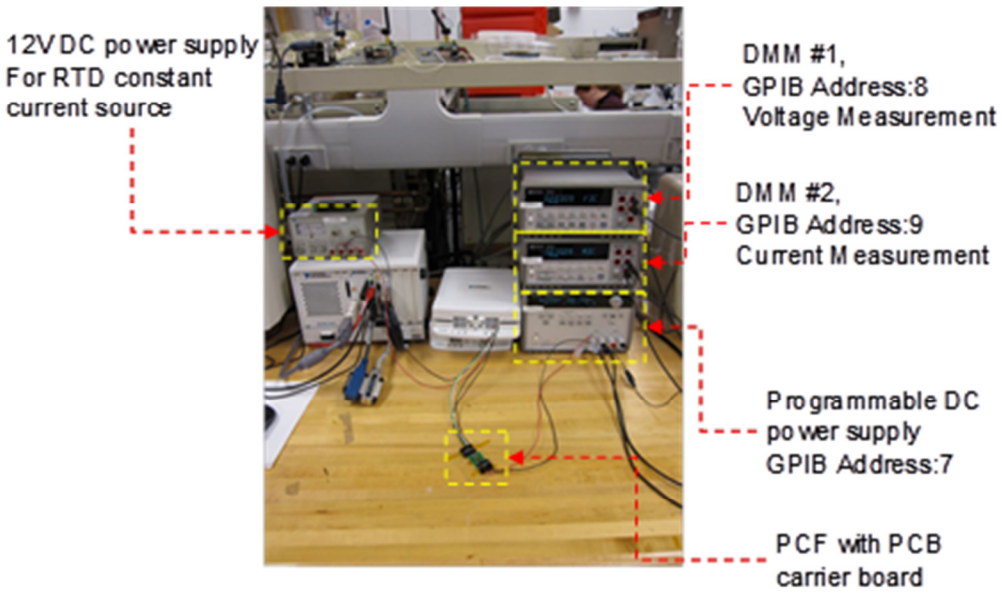

Figure 3-5. Photograph of the initial μF heating test setup, including programmable DC power supply, digital multi-meter, and temperature measurement setup.

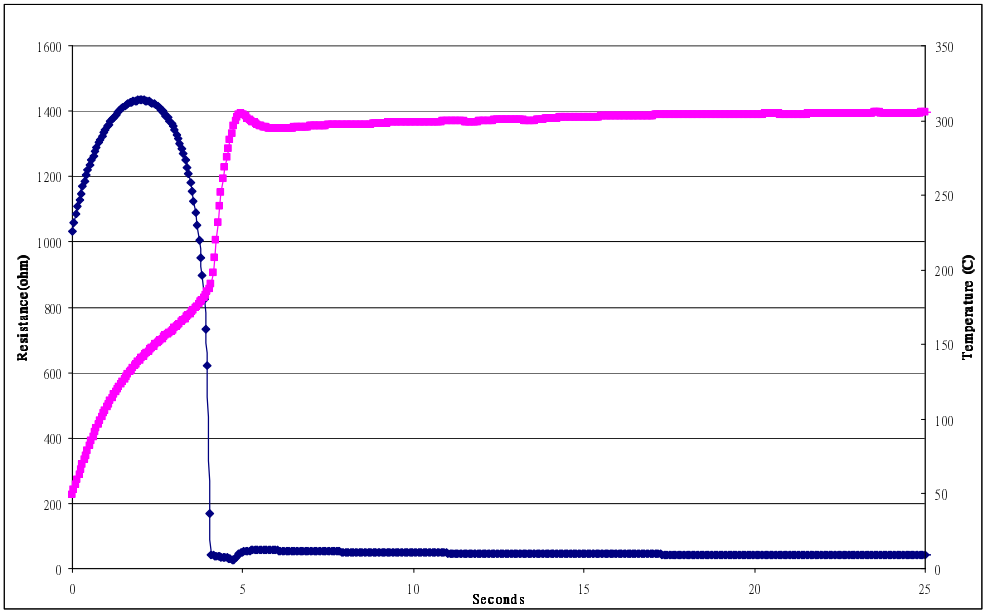

Figure 3-6. The relationship between μF heater resistance and temperature. The heater temperature is shown in pink and resistance is shown in dark blue.

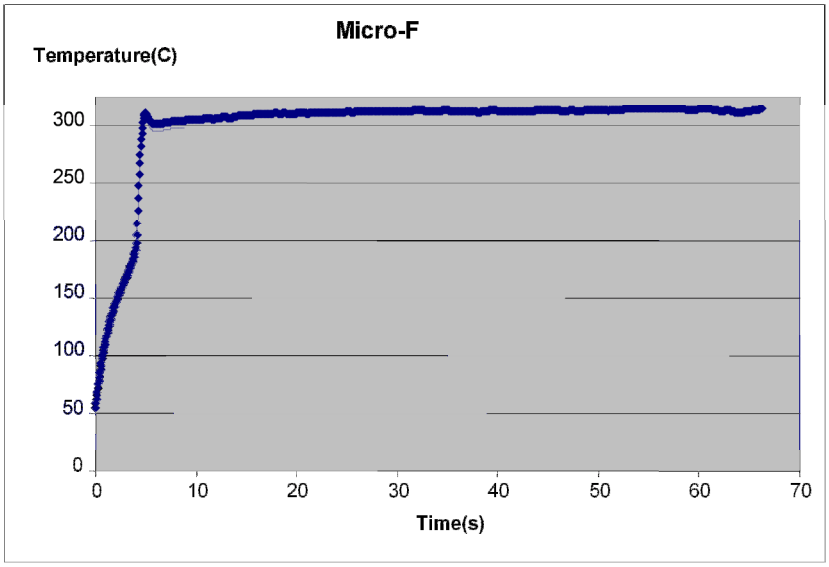

Figure 3-7. The temperature of the μF rises to 300 ^{o}C in 7 sec and is maintained at 300 ^{o}C for 1 min (could be longer) with the programmable DC voltage.

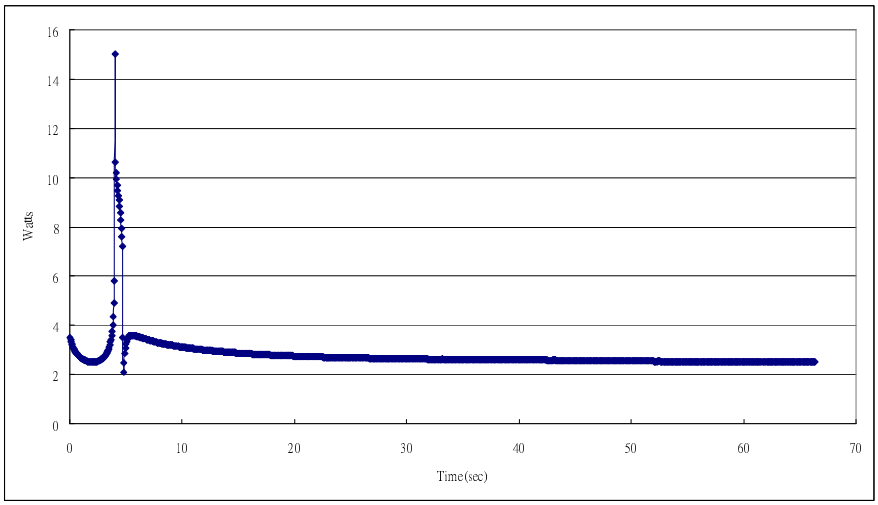

Figure 3-8. The power dissipation of the μF heater when heating from room temperature to 300 ^{o}C and maintaining at 300 ^{o}C.

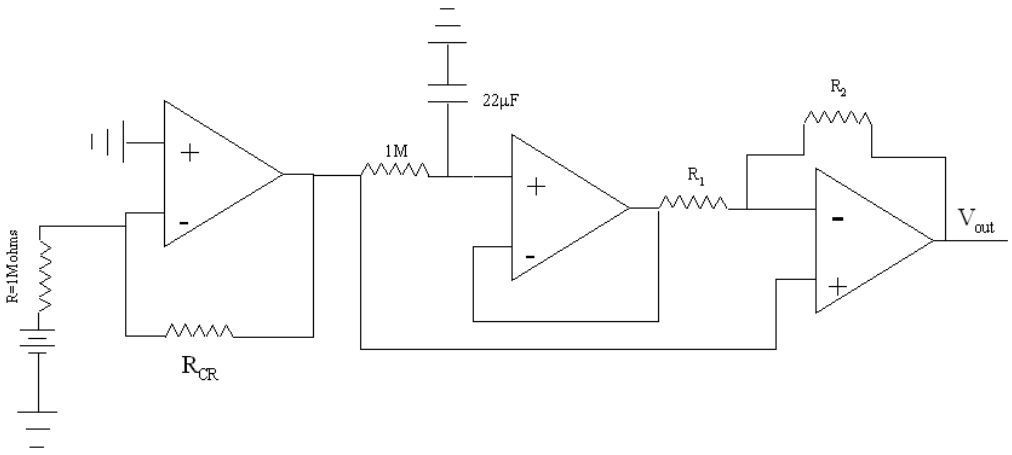

Figure 3-9. The amplifier circuit for chemiresistor signal processing. The operational amplifier converts the CR resistance value to a voltage and amplifies the difference between signals with and without the low pass filter.

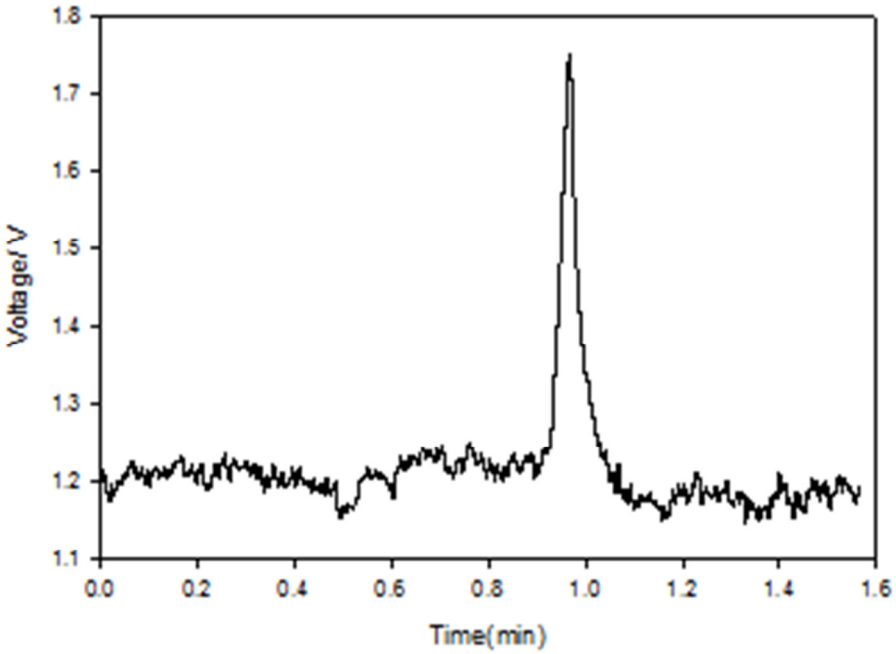

Figure 3-10. The voltage shift for an injected sample of n-octane detected by a C8-coated CR sensor with the amplifier shown in Figure 3-9

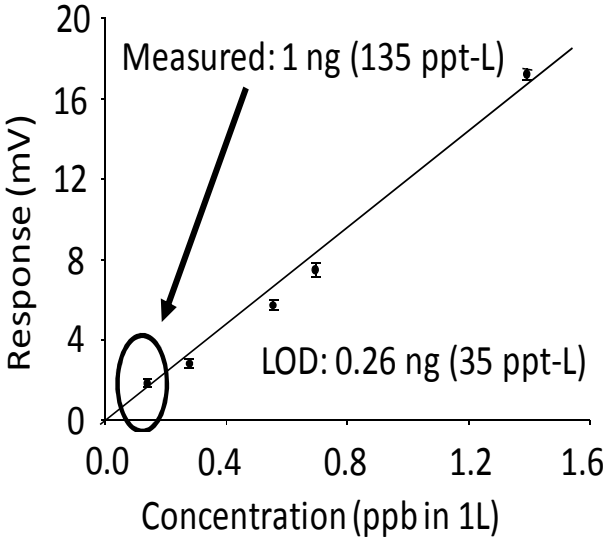

Figure 3-11. Calibration of C8-coated CR sensor response to 2,6-DNT with the sensor connected to a capillary column in a benchscale GC. Sensor was maintained at 70 °C.

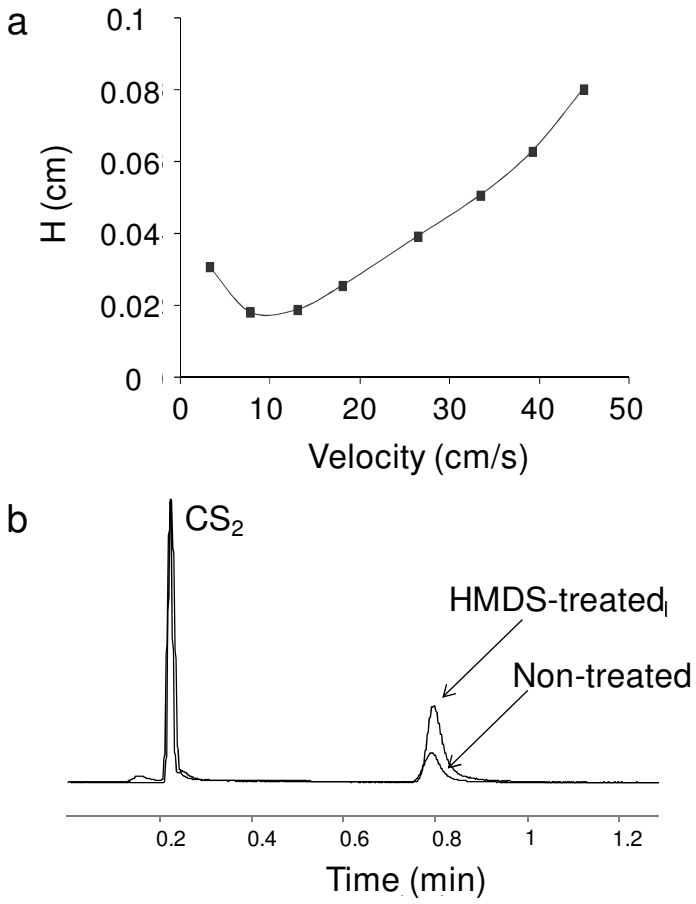

Figure 3-12. (a) Golay plot (n-octane, 30 °C, k = 2.5) for the 1-m PMDS-coated µcolumn using air as carrier gas, (b) Increase in peak height of TNT (in CS_2) after treatment of the µcolumn with HMDS to reduce activity. Detector: FID.

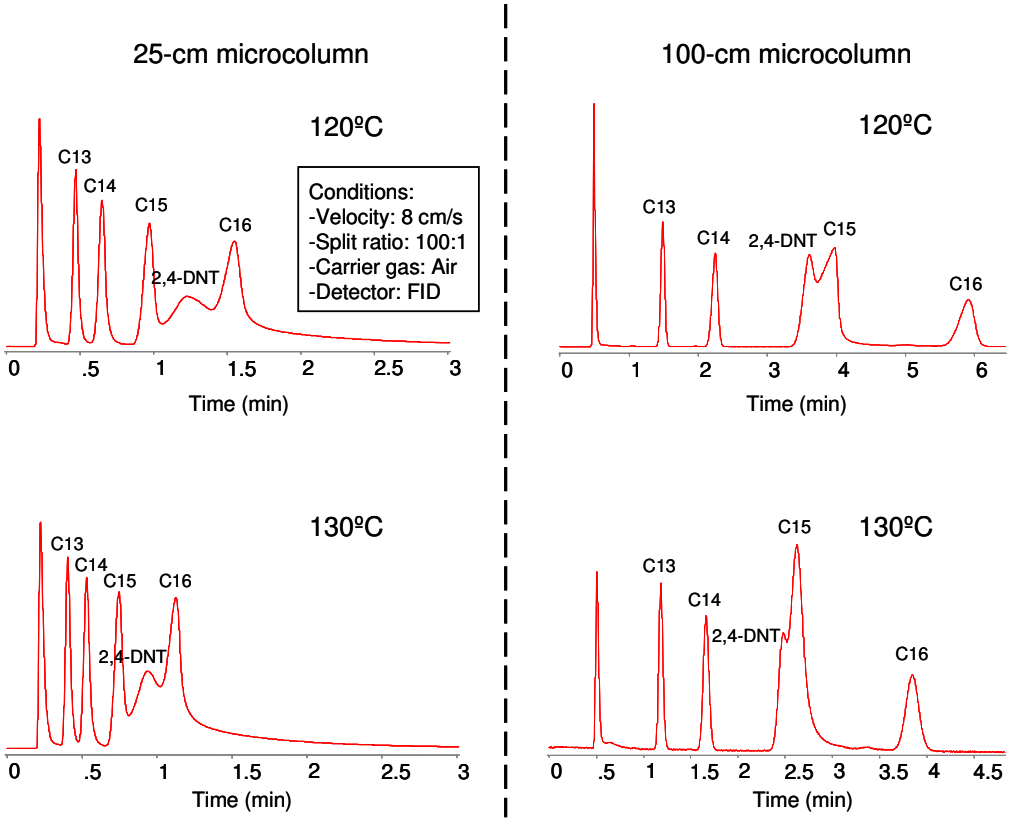

Figure 3-13. Chromatograms from 0.25-m and 1-m microfabricated columns (PDMS stationary phase) of mixture of 2,4-DNT and several n-alkanes illustrating good peak shapes and co-elution of 2,4-DNT with n-C15 alkane. Resolution improves with the longer column, but analysis time increases.

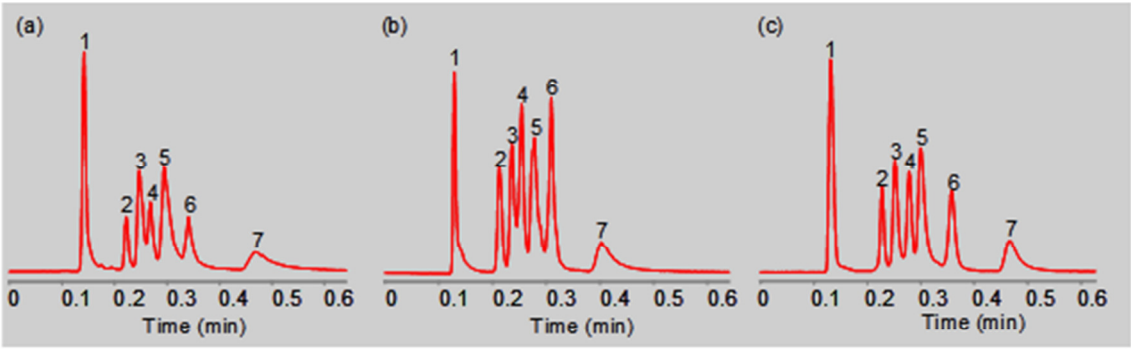

column: 100-cm, 180 x 240 µm I.D., 0.15 µm, PMDS
temperature: 160 °C
detector: FID
carrier gas: air, 2.2 mL/min
injection: 0.01 µL, 100:1 split ratio

Figure 3-14. Chromatograms of a mixture containing 1. carbon disulfide, 2. n-tetradecane, 3. 2,6-dinitrotoluene, 4. n-pentadecane, 5. 2,4-dinitrotoluene, 6. n-hexadecane, 7. 2,4,6-trinitrotoluene. Chromatograms were obtained using (a) GC oven, (b) Stamp® controller, and (c) LabVIEW based PID controller to heat the 1-m microcolumn.

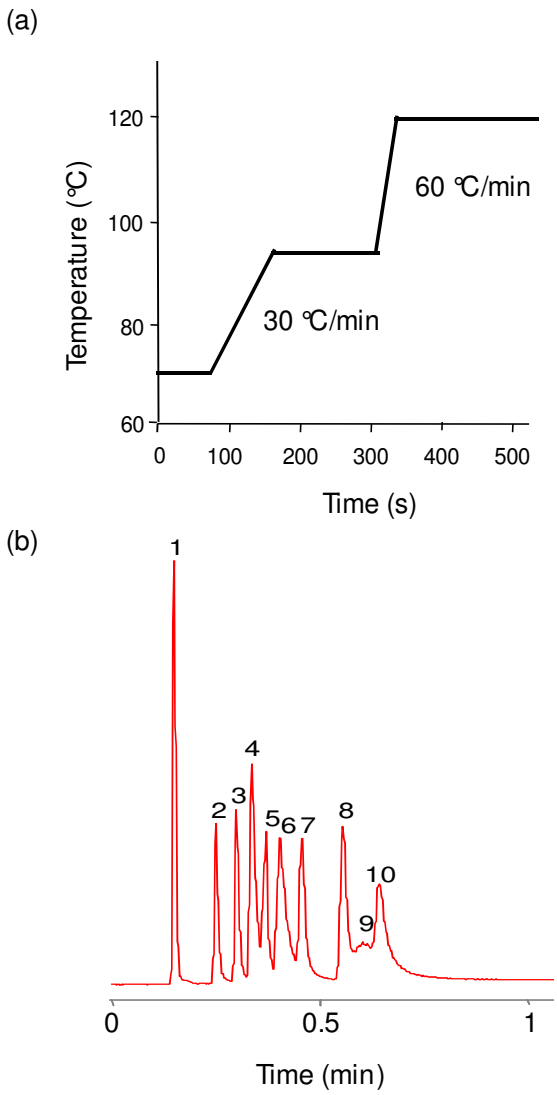

Figure 3-15. (a) Representative microcolumn temperature program obtained with system controller and integrated heaters/sensors; (b) 40-s temperature programmed separation of targets and interferences. Conditions: 120 °C (initial), 4 °C/s to 140 °C, 1 °C/s to 160 °C, 4 °C/s to 180 °C (30 sec); 100:1 split injection; 3.0 mL/min; air carrier gas; FID. Compounds: 1, CS_2; 2, n-tridecane; 3, n-tetradecane; 4, 2,6-dinitrotoluene; 5, n-pentadecane; 6, 2,4-dinitrotoluene; 7, n-hexadecane; 8, n-heptadecane; 9, 2,4,6-trinitrotoluene; 10, n-octadecane

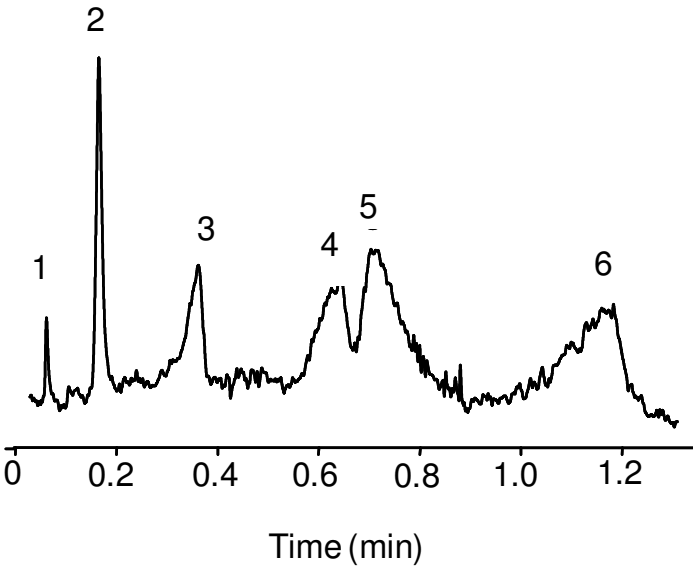

Figure 3-16. Chromatogram obtained using a 1-m PDMS-coated microcolumn and a CR sensor coated with a film of n-octane-thiolate MPN (C8). Conditions: 100 °C (oven), 0.1 µL 100:1 split injection; 0.2 mL/min; air carrier gas; C8-MPN coated CR sensor. Vapors: 1, toluene (solvent); 2, 2-nitrotoluene; 3, n-tridecane; 4, n-tetradecane; 5, 2,6-dinitrotoluene; 6, n-pentadecane .

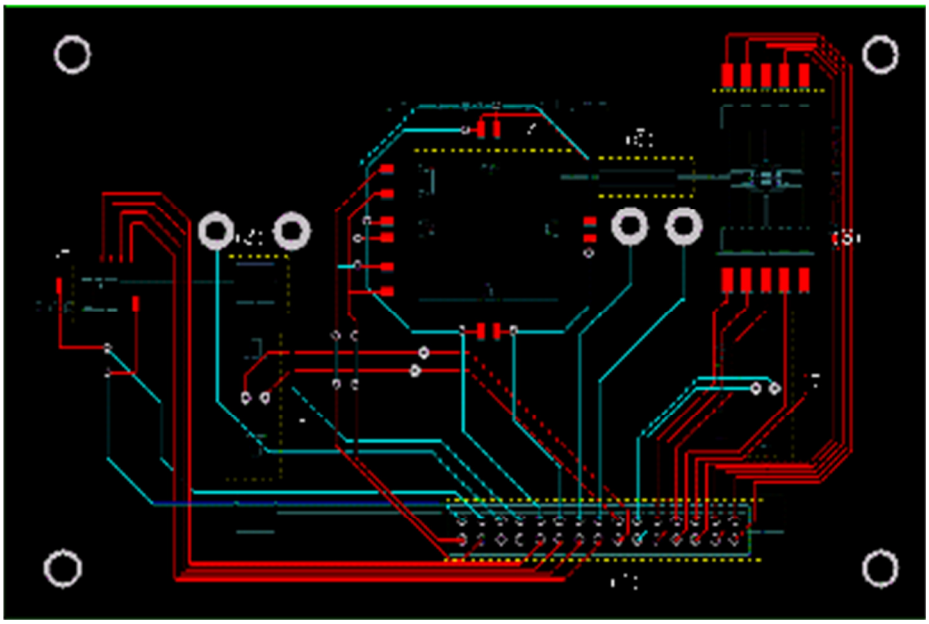

Figure 3-17. The PCB layout of the initial INTREPID microsystem. All electronic connections are routed to a 30-pin connection socket (1). The key components are a micro-focuser (2), micro-tee-connection (3), a 1-m long micro-column (4), heated inter-connection (5), chemiresistor sensor array (6), and two micro-valves (7, 8).

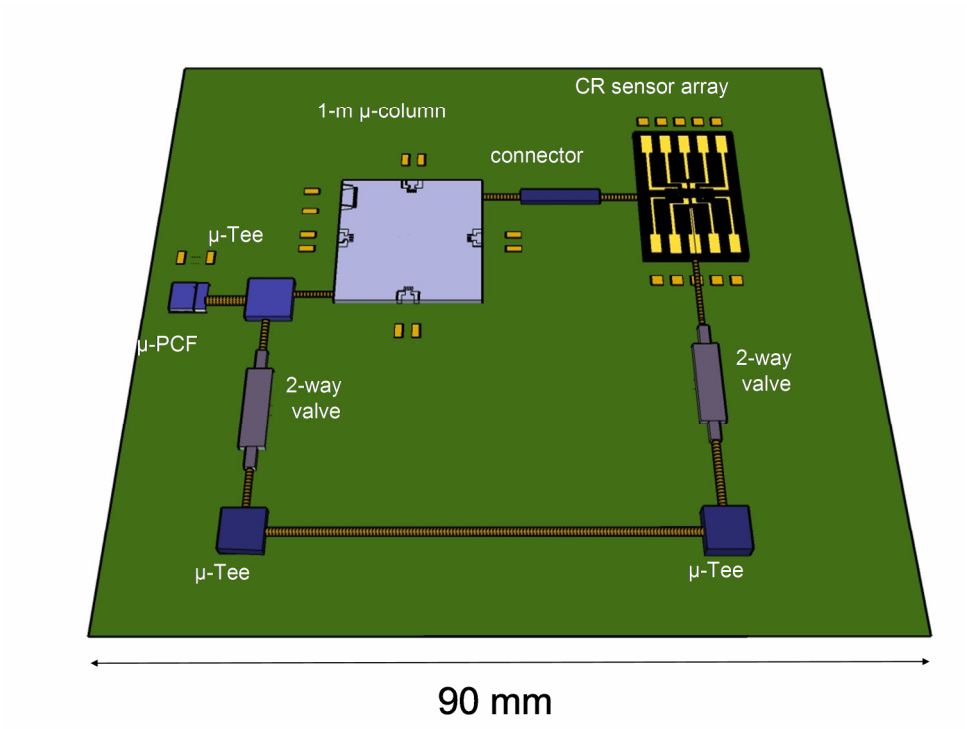

Figure 3-18. Initial design of the INTREPID I fluidic subsystem on a single PCB.

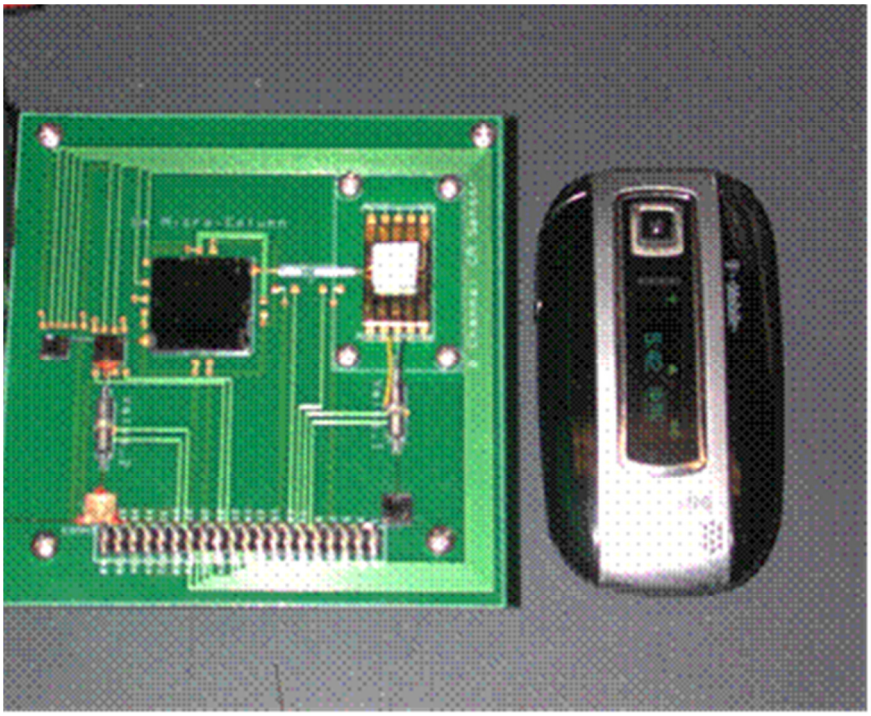

Figure 3-19. The PCB board for the INTREPID system with board-mounted components: preconcentrator-focuser, gas separation column, chemiresistor sensor array, and MEMS interconnectors. A cell phone is shown to the right, for scale.

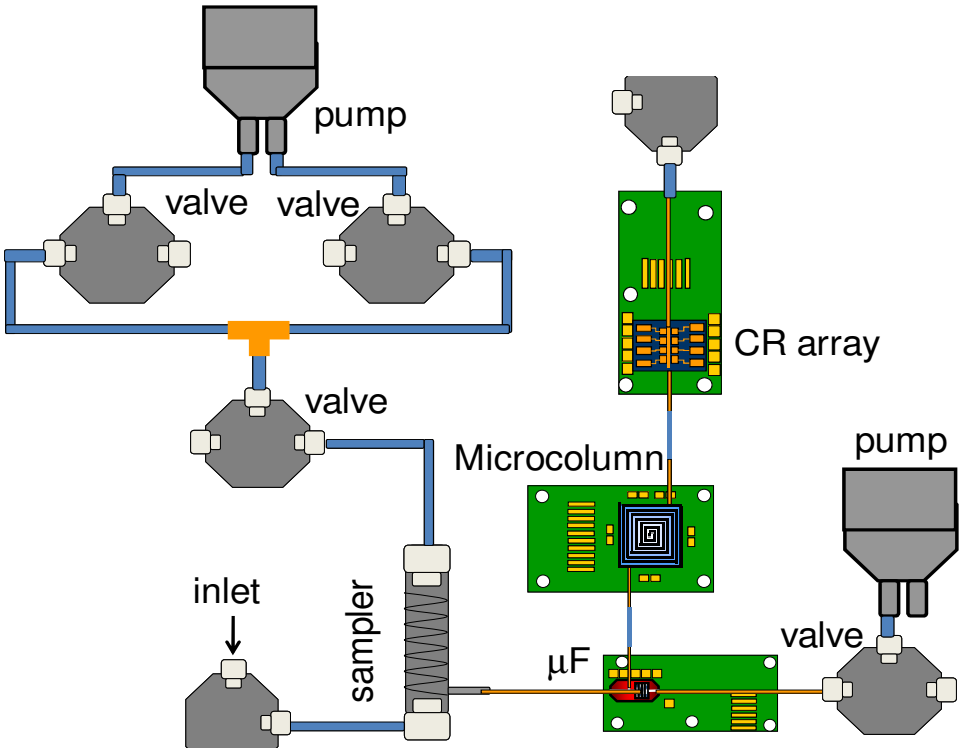

Figure 3-20. Revised layout diagram for fluidic subsystem of INTREPID I.

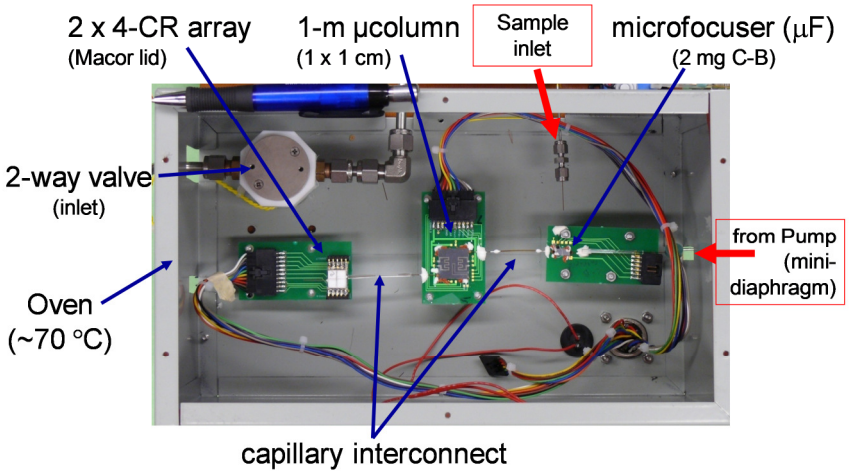

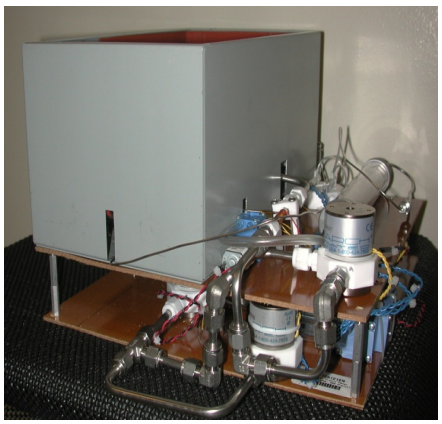

Figure 3-21. INTREPID I lab prototype: (top) microsystem components mounted in the chamber (mini-oven); (bottom) entire prototype.

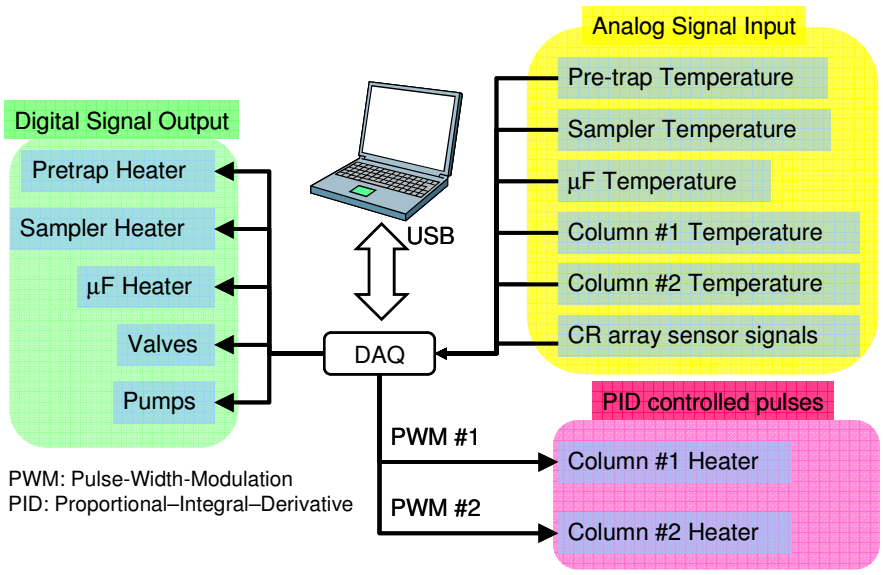

Figure 3-22. Summary of LabVIEW control functions used in the INTREPID I lab prototype.

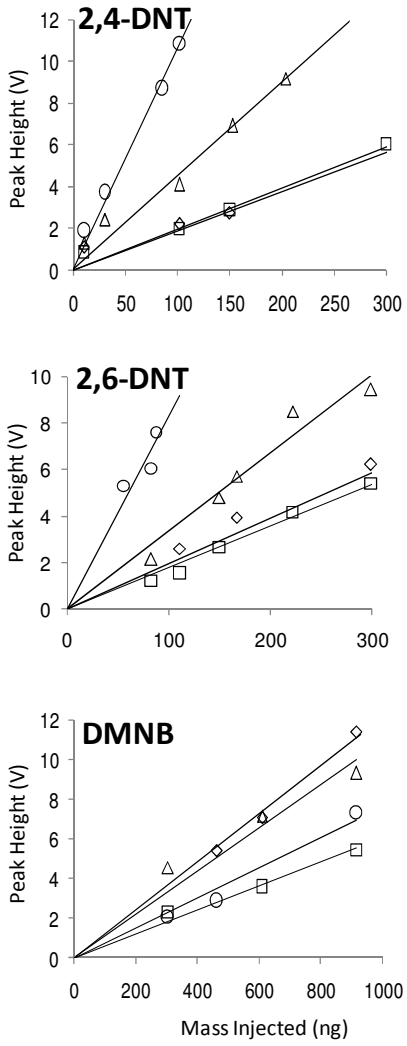

Figure 3-23. Calibration curves using CR-array µGC detector for (a) 2,6-DNT, (b) 2,4-DNT, (c) DMNB and (d) n-C13. Note, data at lower injection masses were quite variable and were removed prior to plotting.

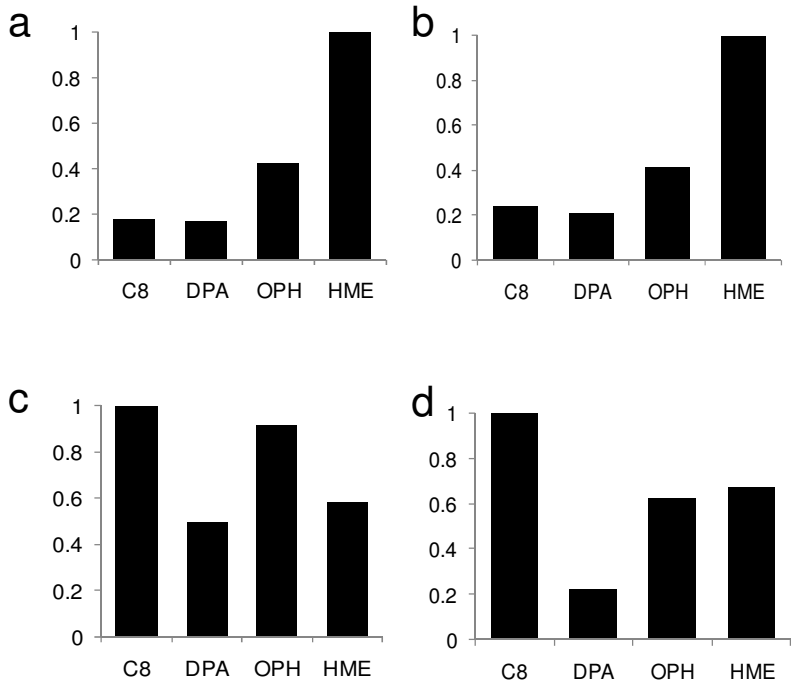

Figure 3-24. Relative response patterns using CR-array μGC detector for (a) 2,6-DNT, (b) 2,4-DNT, (c) DMNB and (d) n-C13. Each pattern was derived from the slopes of the calibration curves presented in Figure 3-23 and then normalized to the sensor giving the largest response.

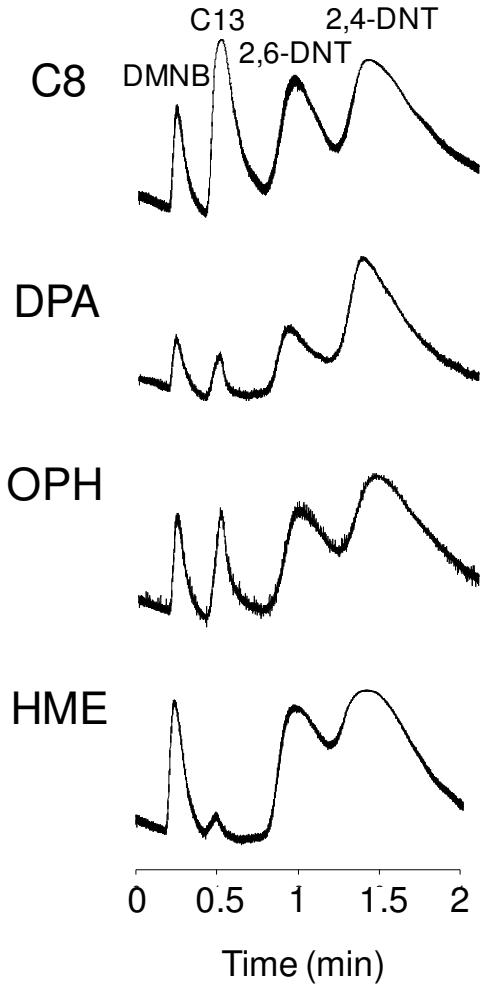

Figure 3-25. Full analysis of the three target explosive marker compounds and C13 interference with the INTREPID I lab prototype; the sampler was spiked with a mixture of the analytes in a 1-L air sample, focused, injected, separated, and detected in 3.5 min.

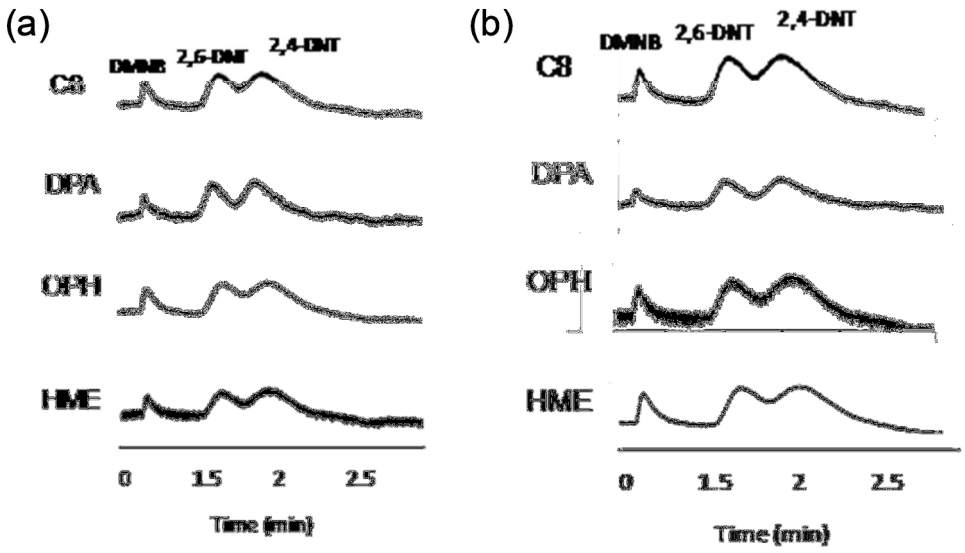

Figure 3-26. Responses from two different CR arrays used as the detectors in the INTREPID I prototype. Data demonstrate highly reproducible retention times and modularity of the sensor arrays.

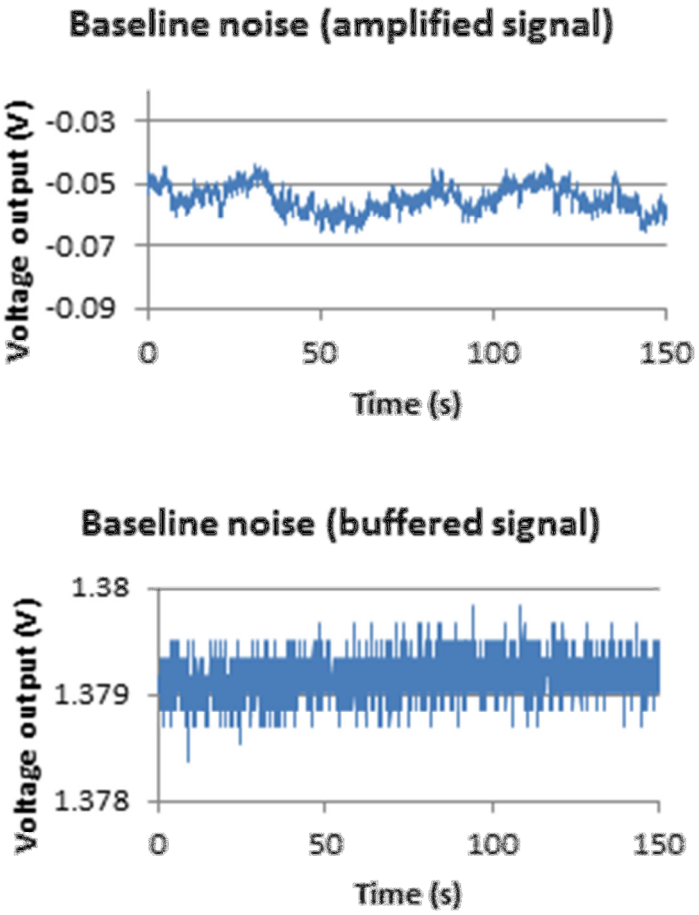

Figure 3-27. Sensor baseline noise levels for one channel using fixed resistors.

CHAPTER IV

A MICRO GAS CHROMATOGRAPH FOR HIGH-SPEED DETERMINATIONS OF EXPLOSIVE MARKERS-FIELD PROTOTYPE/INTREPID-II

4.1. Introduction

Building directly on the work performed for Chapter 3 on the INTREPID I lab prototype, here we describe the design, development, assembly, and laboratory characterization of the INTREPID II μGC field prototype. We continue to focus on determinations of the following markers of 2,4,6-trinitrotoluene (TNT) at very low concentrations in the gas phase: 2,3-dimethyl,2,3-dinitrobutane (DMNB), 2,6-dinitrotoluene (2,6-DNT) and 2,4-dinitrotoluene (2,4-DNT). As mentioned earlier, these semi-volatile marker compounds are considered vapor signatures of military-grade TNT, the vapor pressure, p_v, of which was considered too low to analyze with this prototype (p_v = 6.71 $\times 10^{-6}$ torr). The 2,6- and 2,4-DNT isomers are manufacturing impurities of TNT with p_v values of 9×10^{-4} torr and 4×10^{-4} torr, respectively. DMNB ($p_v = 2 \times 10^{-3}$ torr) has been designated by the ICAO as an explosive taggant [1]. The 2,6-DNT isomer accounts for < 4% of the equilibrium vapor mass in the headspace of TNT, whereas 2,4-DNT accounts for 35%, and other TNT and DNT isomers account for < 2%. These vapor concentrations indicate that 2,4-DNT will always be present in a higher concentration than 2,6-DNT, making it a more suitable marker [2, 3]. Therefore, although work with 2,6-DNT is

presented here, this marker was eliminated from consideration eventually due to its low concentration and marginal utility as a marker for TNT.

The main components of the μGC and the application-specific variables that dictated the component and system designs, configurations, and operating conditions are summarized in the next section. Brief descriptions of all system components are then provided along with the text methods employed for this study. Then results of component-level and subsystem-level tests are presented, and finally results obtained with the assembled prototype.

4.1.1. Analytical subsystem design and operating conditions

Figure 4-1 shows a block diagram of the primary analytical components and fluidic pathways of INTREPID II. The hybrid preconcentrator/focuser (PCF) module consists of a polymer membrane particulate filter that serves as a pre-trap, a conventional stainless-steel tube packed with a granular adsorbent that serves as a high-volume sampler, and a 0.41 cm^2 Si/Pyrex microfocuser (μF) chip with an integrated heater and temperature sensor and an etched cavity packed with a granular adsorbent that serves as a focuser/injector. A 3.2 cm^2 Si/Pyrex chip with a 1-m long spiral etched channel, integrated heaters and temperature sensors, and a wall coated stationary phase serves as the chromatographic separation microcolumn. The chemiresistor (CR) array detector chip has a set of eight interdigital metal electrodes coated with an assortment of four different thiolate monolayer-protected gold nanoparticle (MPN) interface layers and is capped with a Macor® lid. A set of 6 solenoid-actuated two-way or three-way valves was used to direct airflow provided by one of two mini-diaphragm pumps. Scrubbers were used to clean the ambient air carrier gas used for focusing and analysis. Not shown in the diagram is the stainless-steel manifold on which all valves were mounted and through which all flow streams were directed.

The instrument has three operational modes that are executed automatically in sequence. First, the sampling mini-pump (pump 1) draws an air sample through the pre-trap and manifold-mounted sampler. Next, by actuating the appropriate valves, the sampling pump draws scrubbed ambient air in the opposite direction through the sampler as it is resistively heated to desorb and transfer the captured vapors to the μF. Third, after another set of valve actuations a second mini-pump (analysis pump) draws scrubbed air in and pushes it through the μF as it is heated rapidly to backflush and inject the focused vapor mixture into the 1-m μcolumn for chromatographic separation and detection by the MPN-coated CR array. The combination of selective preconcentration, chromatographic separation, and CR-array response patterns is used to provide rapid determinations of the targeted explosive marker compounds at low concentrations in the presence of interfering volatile and semi-volatile organic compounds (S/VOC).

In operation, the pre-trap should capture and retain particles and low-vapor-pressure particle-adsorbed interferences, while allowing the marker compounds to pass unretained. The sampler should capture the marker compounds and interferences with similar vapor pressures quantitatively at a flow rate as high as a few L/min, and desorb the markers with high efficiency. The μF must have sufficient capacity to capture the bolus of vapors transferred from the sampler but also be heated and swept rapidly to provide relatively sharp injection bands. By operating the sampler and μF at elevated baseline temperatures and carefully adjusting the flow rates during sampling and focusing, most compounds more volatile than DMNB (the most volatile marker) should pass through unretained, which reduces the number of compounds reaching the microcolumn (see Chapter 2). The 1-m microcolumn is long enough to provide sufficient peak capacity, but short enough to permit separations to be completed in ~ tens of seconds. Temperature programming with the on-board microcolumn heaters facilitates high-speed

separations. The thiolates in the MPN films are intended to impart partially selective responses to all eluting vapors, such that the collective response pattern from the array differs among the markers and interferences. This, then, should enhance the reliability of the marker determinations.

The performance criteria dictating the design and operating conditions of the INTREPID II μGC prototype are the speed of analysis, limits of detection (LOD), and the selectivity/reliability of the marker determinations. A trade-off must be made between the achievable LODs and the analysis time. We found no official guidance in the literature on these criteria for explosive marker determinations at airport security checkpoints, so we adopted provisional goals of ≤ 2 min per analysis (including sampling, focusing, injection, separation and detection) and 1 ng as the LOD for each marker. Given these criteria and preliminary data collected on the sensitivities of the sensors in the CR array as GC detectors for the marker compounds, we then decided on a target sample volume of 1 L. This translates to an LOD ~0.14 ppb for 2,4-DNT, 2,6-DNT, and DMNB vapor. In order to meet the 2-min analysis time criterion, the provisional duration of each mode in the analytical sequence was set as follows: 20 sec for sampling, 40 sec for focusing, and 60 sec for separation/detection.

4.2. Experimental

4.2.1. Materials

DMNB, 2,6-DNT and 2,4-DNT were purchased from Sigma-Aldrich (Milwaukee, WI) in 99% purity and were used as received. Standard solutions of the marker compounds in acetonitrile/methanol (1 mg/mL) were purchased from AccuStandard (New Haven, CT). All other S/VOCs were purchased from Sigma-Aldrich or Fisher Scientific (Pittsburgh, PA) in 99% purity and used as received. The graphitized carbons, Carbopack B (C-B, 60/80 mesh, specific surface area = 100 m^2/g), and Carbopack Y (C-Y, 60/80 mesh, specific surface area = 24 m^2/g) were

purchased from Supelco (Bellefonte, PA). Polydimethylsiloxane (PDMS) was obtained from Ohio Valley Specialty Chemicals (OV-1, Marietta, OH), and the surface pretreatment agent Rejuv-8® was obtained from Sigma-Aldrich. MPNs derived from the following thiols were synthesized by the method reported by Rowe et. al. [4]: n-octanethiol (C8), 6-phenoxyhexane-1-thiol (OPH), 4-(phenylethynyl)-benzenethiol (DPA), and methyl-6-mercaptohexanonate (HME). The MPNs had core diameters in the range of 3.4 – 4.7 nm.

4.2.2. Primary analytical components

The PCF module components (i.e., pre-trap, sampler, and μF) have been described previously (see Chapter 2) [5]. Briefly, the sampler was constructed from a 6-cm long, 0.25-inch i.d. thin-walled stainless-steel tube with a 6-cm long, 0.0625 i.d. side-port tube located about 2 cm from one end. Either a single bed of 50 mg of C-B or a tandem bed of 35 mg of C-B and 15 mg of C-Y was used in the sampler. Fractions of these adsorbent materials with nominal diameters in the range of 212-250 μm were sieved and isolated, preconditioned at 300 °C for 6-h under helium, and packed in the sampler. A Cu resistive heater coil and a fine-wire thermocouple (Omega, Stamford, CT) were used for heating to 250 °C at 15 °C/s during thermal desorption. The capacity of the sampler, with either adsorbent bed, was determined to be sufficient in prior testing (see Chapter 2), assuming a baseline temperature as high as 40 °C.

The 0.41 cm^2 μF chip contains a deep-reactive-ion-etched (DRIE) Si cavity with a Pyrex cap, tapered inlet/outlet, a side port for filling with adsorbent and DRIE-Si pillars (0.15 mm widths and spaces, 0.38 mm height) near the inlet and outlet ports for retaining the adsorbent granules. An additional flow channel in the chip forms a tee connection with one of the two main flow channels to facilitate loading and backflushing of the sample. All three fluidic ports on the μF chip have

expansion sections that accept 250 μm i.d. fused-silica capillaries used for interconnections. The device is resistively heated with Cr/Au contacts and a Ti/Pt resistive temperature device (RTD) patterned near the contacts to control thermal desorption/injection temperatures. The device is sealed with an anodically bonded Pyrex plate (0.1 mm thick). Deactivated fused-silica capillary tubing was inserted into the three fluidic ports and secured with high temperature silicone adhesive (Duraseal® 1531, Cotronics, Brooklyn, NY). Electrical connections to a custom printed circuit board (PCB) were made using gold wire-bonds and gold pads. The μF was packed with the adsorbent by applying gentle suction at the outlet port through the fill port at the side of the cavities. After packing, the filling port was sealed with Duraseal®. Approximately 2 mg of (sieved) C-B was packed in the μF, as determined gravimetrically. The inlet capillary of the μF was connected to the side-port tube of the sampler by means of a 0.16 cm i.d. stainless steel union (Valco, Houston, TX) also wrapped with a Cu wire coil. The μF was heated from its baseline temperature of 70 ºC to 250 °C at 375 ºC/s during injection, maintained at that temperature for 60 sec, and then allowed to cool. This was sufficient to desorb the target analytes completely.

The 1-m microcolumn chip has 1.8 × 1.8 cm^2 footprint and consists of a convolved square spiral DRIE-Si channel 150 μm (*w*) × 240 μm (*h*) capped with an anodically bonded Pyrex cover plate. The fabrication and characterization of the microcolumn has been described previously [6, 7]. Two meander-line Cr/Au heaters and a Ti/Pt RTD were evaporated onto the backside of the microcolumns and are used for programmed heating during separations. The inlet and outlet ports were expanded to 350 × 250 μm to accommodate capillary interconnections. Deactivated fused silica capillaries (0.25 mm i.d) were connected to these ports with epoxy (Hysol Epoxy Patch 1C, Rocky Hill, CT). The interior walls of the microchannels (and roughly 2 cm of the connecting capillaries) were coated with a 0.15 μm thick cross-linked film of OV-1 from a 1:1

n-pentane:dichloromethane solution (0.5% w/v PDMS, 0.005% w/v dicumyl peroxide), using a static coating and thermal cross-linking method described previously [6]. The microcolumn was subsequently post-treated with Rejuv-8 to reduce surface activity. The maximum number of theoretical plates (N) produced by the coated microcolumn was 4600 plates/m (n-octane, 30 °C, k = 2.5) at 12 cm/s (u_{opt}) using air as carrier gas, which corresponds to a 0.2 mL/min volumetric flow rate [7]. The microcolumn was inverted (Pyrex side down) and mounted on a custom (PCB) with a hole cut out beneath the device, and then the heaters and temperature sensor were wirebonded to pads on the PCB.

The CR array used in this prototype has been previously described [8-10], and was characterized in work discussed in Chapter 3. The array chip has dimensions of ~2 × 1.2 cm. Each of the 8 interdigital electrodes has 24 Au/Cr finger pairs (5 μm widths/spaces, 450 μm length, 410 μm overlap), and a gold bonding pad for electrical inter-connections. Solutions of the MPNs (~ 5 mg/mL) were dissolved in an appropriate solvent (toluene for C8, DPA, OPH and dichloromethane for HME) and deposited individually by microliter syringe to create multilayer films with baseline resistances within the range of 1-10 MΩ (Note: thickness was not determined). Two sensors were coated with each type of MPN. The array was capped with a Macor™ lid with inlet/outlets ports, and sealed with a gasket of VHB tape (3M, St. Paul, MN) to create a detector cell volume of 1.6 μL (0.3 (w) × 0.4 (l) × 0.013 cm (h)). Deactivated fused-silica capillaries were sealed into the ports with Hysol epoxy. The CR array is inserted into a header socket on a custom (PCB) by means of header pins soldered to the gold bonding pads.

4.2.3. Test-atmosphere generation

Saturated test atmospheres of the marker compounds were prepared by adding small quantities of the solids to septum-sealed round-bottom flasks subsequently purged briefly with extra-dry N_2. Aliquots were then taken by gas-tight syringe and injected into a tee-connector with a septum port and a dilution line connected to the inlet of INTREPID. A separate flask was prepared with saturated test atmospheres of a mixture of several VOCs that represent potential interferences. Mixture chromatograms were obtained by injection of the appropriate volume of headspace from each of the flasks. A bench-scale GC with ECD detector (Model HP6890, Agilent Technologies, Palo Alto, Ca), previously calibrated with standards of the marker compounds, was used to confirm vapor concentrations. All tests atmospheres were used at ambient temperature.

4.3. Results and Discussion

The performance of the fully integrated system relies on reconciling the differences in optimal flow rates and temperatures of the component devices as well as the inherent limitations of each device. Although considerable work has been devoted to characterizing the performance of the system components, there integration gives rise to additional challenges. Having established the target LOD, set of interferences, and time of analysis, it remained to confirm the performance of the components, assemble the components into subsystems and then into the full system, reconcile the tradeoffs associated with system integration, and demonstrate automated operation.

4.3.1. Microcolumn characterization

The PCB-mounted microcolumn was placed inside the oven of the GC and connected to the injection port and FID with deactivated capillaries. The oven was maintained at 70 °C and the microcolumn was heated to 120 °C (isothermal) using the integrated heaters. A solution containing all three marker compounds (0.25 mg/mL in acetone) was injected by auto-sampler (0.1 µL, 1000:1 split ratio, injector temperature = 225 ºC) at each of six different flow rates ranging from 0.2 to 5 mL/min. At 0.2 mL/min, which corresponds to the Golay minimum for this microcolumn [7], the separation requires 4 min and there is a significant amount of unused space in the chromatogram. Increasing the flow rate to 5 mL/min reduces the elution time to about 70 sec and the markers are still fully resolved, but the full-width-at-half-maximum (*fwhm*) values are still quite large: 1.2, 9 and 14 sec for DMNB, 2,6-DNT and 2,4-DNT, respectively (N = 400 plates/m at this flow rate), warranting the use of temperature programming.

After a series of exploratory experiments, conditions were established to permit the separation of the three markers and four n-alkanes of similar volatility (*n*-C_{13} to *n*-C_{16}) in just 22 sec, as shown in Figure 4-2. This represents the best separation possible in the shortest period of time. The R_s values, defined as $2(t_{R2} - t_{R1})/[w_1 + w_2]$, where t_{R2} and t_{R1} are the retention times of two compounds, and w_1 and w_2 are the base peak width of the compounds, for the critical marker-alkane pairs are 1.5, 1.3, and 0.8 for DMNB/C_{13}, 2,6-DNT/C_{14}, and 2,4-DNT/C_{15}, respectively. The corresponding *fwhm* values for the markers are 1, 1.5, and 2.5 s, respectively. Thus, excellent chromatographic separation can be obtained at high speed using the 1-m microcolumn with on-board heaters and temperature sensors in air in the absence of significant extra-column band broadening.

4.3.2. Microfocuser and microcolumn integration

In Chapter 2, we reported that *fwhm* values of the injection bands generated by desorption from μF directly to an ECD at 3 mL/min were 1.3, 3.5, and 5.7 sec for DMNB, 2,6-DNT and 2,4-DNT, respectively. During initial attempts to use the μF as injector, the μF and microcolumn were connected via deactivated capillary and mounted inside the GC oven at 70 °C. The μF was connected to the GC injection port (225 °C, splitless) and the microcolumn outlet was connected to the ECD. Purified air was used as carrier gas. By temporarily blocking the flow through the column, 0.5 μL of an acetone solution of the explosive markers (0.25 mg/mL for DMNB and 2,6-DNT, and 0.75 mg/mL for 2,4-DNT) was injected by syringe and passed via the on-chip tee-branch through the μF adsorbent bed to mimic desorption from the sampler. The outlet port of the μF was vented and the acetone was not retained on the adsorbent. Then, the tee-branch inlet to the μF was disconnected from the injection port and blocked with a septum, the outlet of the μF was connected to the GC injection port, the microcolumn outlet was re-connected to the ECD, and the flow rate was adjusted to 3 mL/min. Prior to injection (with backflushing), the on-board heaters were used to raise the baseline temperature of the microcolumn to 120 °C. This procedure was followed during a series of experiments aimed at optimizing the separation conditions. Unfortunately, attempts to use the on-column heaters to program the temperature of the separation, as in Figure 4.2, resulted in significant co-elution of 2,6- and 2,4-DNT. Although all three markers could be resolved under isothermal separation conditions, as shown in Figure 4-3a, the *fwhm* values were still rather broad for the DNT isomers (i.e., 1.5, 4.3, and 9.1 sec DMNB, 2,6-DNT, and 2,4-DNT, respectively) owing largely to the injection bandwidths.

Therefore, on-column focusing (OCF) was explored as a way of reducing the on-column band broadening. OCF entails starting the μcolumn at a temperature low enough to re-focus the analytes within the stationary phase at the head of the μcolumn. With bench scale instruments and standard capillary columns this can be achieved by actively cooling a short segment of the column near the inlet. For a portable instrument this is not feasible. However, due to the very low p_v values of the markers, it was thought that the baseline temperature of 70 °C might be sufficiently low to achieve some degree of focusing.

Figure 4-3b shows the effect of starting the separation with the microcolumn at 70 °C for 20 sec and then ramping the temperature at 8 °C/s to one of several maximum temperatures ranging from 100 to 180 °C for the remainder of the separation. Nitrogen at 3 mL/min was used as carrier gas. The DMNB *fwhm* value was not affected significantly due to its higher p_v value, whereas the *fwhm* values for 2,6- and 2,4-DNT were reduced to as low as 1.4 and 2.3 sec, respectively, and the significant tailing observed under isothermal conditions was greatly reduced. As a result, the overall elution time did not change significantly, despite the 20-sec focusing segment. Although, the *fwhm* decreased with an increase in final temperature from 100 to 130 °C, R_s for 2,6- and 2,4-DNT was nearly constant due to a greater decrease in retention time of the 2,4-DNT relative to the 2,6-DNT. Above 130 °C, the *fwhm* values were constant while R_s declined further, again, due to greater reductions in the retention time of the 2,4-DNT. Higher final temperatures were not explored, to avoid possible column bleeding. Figure 4-3c shows the separation of the three explosive markers generated using OCF, with 70 °C for 20 sec followed by a ramp at 8 °C/s to 130 °C. The R_s between 2,6-DNT and 2,4-DNT is greater than 1, and no peak tailing as in Figure 4-3a is observed.

4.3.3. Microcolumn and CR array integration

Figure 4-4a shows the response of C8 sensor to 2,6-DNT at five temperatures ranging from 50 °C to 80 °C. The CR array was located in a controlled heating box in top of the bench scale GC and connected to a 30-m DB-1 capillary column held at 110 °C. The decrease in peak area reflects the reduction in partitioning as the temperature increases, and similar reductions were observed for all sensors in the CR array (see ref.10 for a more complete study of temperature effects on MPN-coated CR array detectors). A commensurate increase in resolution would be expected due to the reduction in *fwhm* (assuming constant retention times). The effect of flow rate on the *fwhm* of 2,4-DNT is shown in Figure 4-4b for two sensors, C8 and OPH, held at 70 °C. For these tests, a solution of 2,4-DNT (0.25 mg/mL CS_2, 0.5 µL injection, 100:1 split ratio), was injected through the injection port of the bench-scale into the microcolumn, which had the CR array connected downstream. A set of FID responses obtained under similar conditions is shown for comparison. In both cases, the *fwhm* values decrease with increasing flow rates. At lower flow rates, the *fwhm* for the sensor response is wider than the FID response (e.g., at 0.8 mL/min, the ratio is 1.4), however at the higher flow rates, there is almost no difference (note: the effects of flow rate on peak area and peak height are described in a separate study; see ref. 10). Although higher flow rates apparently reduce this source of extra column band broadening, the constraint on flow rate imposed by chromatographic resolution must also be considered.

In a subsequent test, the microcolumn and CR array were mounted inside the GC oven held at 70°C. The microcolumn temperature was raised to a baseline of 120 ºC using the on-column heaters. The upstream port of the microcolumn was connected directly to the GC injector (225 ºC, 100:1 split) and a CS_2 solution (0.5 mg/mL each) of the three markers and three n-alkanes (i.e., *n*-C_{14}, *n*-C_{15}, and *n*-C_{16}) was manually injected via syringe. Purified air was used as carrier gas.

Figure 4-5 shows a representative set of chromatograms generated with this subsystem at a flow rate of 1.2 mL/min (note: this flow rate provided better resolution than 3 mL/min). The mixture components elute in 3 min, and the resolution is clearly degraded. Values of R_s are 0.9 for the *n*-C_{14}/2,6-DNT pair and 0.75 for the *n*-C_{15}/2,4-DNT pair. Estimated *fwhm* values were 3, 16, and 22 sec, for DMNB, 2,6-DNT, and 2,4-DNT, respectively. The *fwhm* values for 2,6- and 2,4-DNT are 35-40% greater than those obtained by replacing the CR array with an FID at the same flow rate (data not shown). The extra band broadening associated with the CR array can be attributed to the dead volume in the detector cell, non-specific adsorption on detector-cell-wall and interconnecting surfaces, and finite sorption/desorption kinetics in the MPN films on the sensors, despite operating at an elevated detector temperature (70 ºC). It is interesting to note the selectivity toward the markers over the alkane interferences, particularly for the DPA, OPH, and HME MPN films. This selectivity leads to response patterns that differ significantly for the alkanes relative to the markers. As noted above, the use of OCF reduces the on-column band-broadening, which will enhance the separations, but the contribution of detector dynamics to extra column band broadening is significant and noteworthy.

4.3.4. Microsystem calibration

Tests were then performed with the microsystem components assembled and integrated into a subsystem comprising the μF, 1-m microcolumn, and CR array. Each was mounted on a separate carrier PCB fixed to a common substrate board via standoff bolts, and connected via press-fit connectors to the other components. This assembly was placed in a bench scale GC oven held at a baseline temperature of 70 °C. The results of these experiments were obtained by another

member of the group (Lindsay Wright) as part of this project, but are reported here, in summary fashion, for continuity.

Solutions of each of the individual markers, as well as *n*-C_{13}, were prepared at several concentrations in acetone and used as the calibration standards. Autosampler injections (0.1-0.25 µL) were made through the GC injection port to which the µF was connected. The loading flow rate was 3 mL/min and the downstream port of the µF was vented into the oven. At this temperature the acetone was not retained on the C-B adsorbent of the µF. The µF was then heated to 250 ºC at 375 ºC/s to inject the analyte at 3 mL/min into the 1-m microcolumn for elution and detection by CR array. For DMNB, 2,6-DNT and 2,4-DNT, the mass range was 5 to 25 ng, for *n*-C_{13} the mass range was 50 to 100 ng.

Figure 4-6 shows the resulting calibration curves (peak area vs. mass injected) for DMNB, 2,6-DNT, 2,4-DNT, and *n*-C_{13}. Peak areas were derived from the integrated voltage signals of the sensors by converting them to resistance changes and then dividing by the baseline resistance. As shown, the peak areas vary linearly with mass; the linear regression slopes with forced-zero intercepts had r^2 values ranging from 0.97 to 0.99. The LODs were calculated via the equation 3σ/sensitivity, where σ is the standard deviation of the baseline noise, and sensitivities were based on peak height (not peak area). On the basis of the most sensitive sensor for each analyte, the LODs were 2.2 ng (HME) for DMNB, 0.5 ng (HME) for 2,6-DNT, 0.9 ng (HME) for 2,4-DNT, and 12 ng (OPH) for *n*-C_{13}. Assuming a 1-L sample volume, these correspond to concentrations of 0.30, 0.06, 0.12, and 1.63 ppb for DMNB, 2,6-DNT, 2,4-DNT, and n-C13, respectively (note the selectivity toward the markers).

4.3.5. Prototype assembly and system operation

Following these preliminary experiments on the components and sub-systems, we commenced to build the INTREPID-II prototype. The packaged prototype has dimensions of 13 (*l*) × 11.3 (*w*) × 5.3 inches (*h*) and weighs 15 pounds. Figure 4-7 shows a picture of INTREPID-II prototype with all major fluidic and analytical components. A stainless-steel manifold was created with tapered, top-surface mounting ports designed to match those on each of the six 3-way latching solenoid valves used to direct the flow (Lee Co., Westbrook, CT). The sampler was also mounted on the manifold using 0.25 inch stainless-steel Swagelok fittings connected to stainless-steel tubing coming in/out of the manifold. A fan was mounted beneath the sampler to decrease sampler cooling time after thermal desorption, ensuring that the sampler returned to a reasonable temperature (~40 ºC) before the start of the next sample collection step. A double-headed diaphragm pump (D737B, Parker Hannifin, Cleveland, OH) was used for sampling and focusing, and a mini-diaphragm pump (E155, Parker Hannifin) was used for injection, elution, and detection. Two large cylindrical scrubbers packed with charcoal and molecular sieves and mounted on the outer wall of the instrument chassis were connected to the inlet of analysis pump and sampling pump to remove water vapor and background organic vapors during focusing (sampling pump) and analysis (analytical pump) cycles. The pumps were connected to the appropriate ports of the manifold via stainless-steel tubing.

The PCB-mounted analytical components (μF, μcolumn, and CR array) were secured on standoffs to the floor of a mini-oven comprising a fiber-glass insulated 1.5-L sheet metal chamber with a resistor-embedded silicone heater pad mounted to the lid. The chamber is heated so that the components are maintained at a baseline temperature of 70 °C to reduce adsorptive losses on interconnection surfaces that cannot be heated by direct means. Fluidic interconnections among

these components were made using custom-made stainless-steel unions that accept the 0.25 mm i.d. capillary tubing attached to the components. The unions were modified to fit in a small copper cradle, which was heated with a 20Ω resistor and monitored with a thermocouple. This allowed the unions to be maintained at an elevated temperature (~ 90 °C), which further reduced the potential for wall adsorption.

Two circuit boards populated with the appropriate components were used to control and actuate all the components. A custom pneumatic control PCB connected to a digital I/O card (USB-6501, National Instruments, Austin, TX) was used to actuate the pumps, valves, fans, interconnection heaters, and sampler heaters. A second PCB connected to a 16-bit multi-functional DAQ card (USB-6218, National Instruments) provided control of the μF and microcolumn heaters as well as the readout of the thermistors on the PCBs and RTDs on the devices. This control board also provided sensor response amplification, signal filtering, and sensor signal readout in real-time. A USB hub connected the boards to a laptop computer running a control program written in LabVIEW (Ver. 8.5, National Instruments, Austin, TX). This program provided proportional-integral-derivative (PID) temperature control of the heated devices (sampler, heated interconnects, μF, μcolumn). It also provided on-off control for valve switching, pump activation, fan activation, and sensor response readout. User-defined pump, valve, and heater actuation timing and temperature settings, and temperature programming of the microcolumn could be configured at the start of a run through a graphic user interface on the laptop for automatic operation. A manual operation mode of each step and a continuous operation mode, which consists of defining the number of sequential automatic operation modes to be performed, were both possible. Additional components of INTREPID-II included a power supply and a mini-oven temperature control with a digital meter, which were embedded together in a separate external unit.

Resistance changes of the CR-array sensor elements were measured by applying a 3 VDC bias to each CR through a matched reference resistor for each of the eight sensors. The voltage drop across each CR-array element was recorded by the DAQ card at 20 Hz after amplification of the signal difference between baseline and measured values. Data was processed using GRAMS 32 (version 6.0 Thermo Scientific, Pittsburgh, PA). Response patterns derived from the normalized responses from the four MPNs on the CR array were generated using MS Excel (Ver. 14, Office 2010, Microsoft, Redmond, WA).

Due to the net pressure drop associated with the narrow-bore channels in the manifold, the constrictions in the valves, and the length of interconnecting tubing, the maximum flow rate achievable with the dual-head diaphragm pump was 2.7 L/min. Thus, collection of a 1-L sample required 22 sec. Focusing at 40 mL/min for 40 sec was sufficient to transfer the explosive markers quantitatively to the μF with < 10 % breakthrough and minimal carry over (< 1.5 %) (see Chapter 2). An analytical flow rate of 3.0 mL/min was adopted, because it results in a total elution time of < 60 sec for all three explosive markers; however it represents a compromise between the efficiency, resolution, speed, and sensitivity of each of the components.

4.3.6. Prototype testing

Prior to testing INTREPID-II with the explosive markers, the short-term reproducibility of the retention time and responses was examined for a series of VOCs that include: n-octane, xylene, n-nonane, and limonene (25 ppb-L each), at room temperature. A Tedlar® bag containing the mixture was drawn through the sampler at 2 L/min for 25 sec. Then the sample was thermally desorbed with backflushing and transferred to the μF at 40 mL/min for 60 sec. The μF was rapidly heated to 250 ºC and the mixture was backflushed and injected onto the microcolumn at a reduced

flow rate of 2 mL/min , and detected using the CR array kept at *room temperature*. An analysis of the mixture was performed every hour for 4 hr. Scrubbed air was passed through the CR array between analyses.

Figure 4-A1 shows the overlaid chromatograms of the four replicates. The retention times ranged from 22 sec for n-octane to 55 sec for d-limonene, and varied by < 5% (RSD) for all four CR sensors. The variation in peak height ranged from 5% (m-xylene, C8) to 12 % (n-nonane, DPA), and the variation in peak area ranged from 3% (limonene, HME) to 20% (octane, HME). The high RSD can be attributed to changes in ambient temperature, transfer efficiency, and instability of the sensor response. In addition, as evidenced in the chromatograms, an exceptionally large artifact peak (presumably water vapor), at the beginning of the chromatogram overlapped with the first eluting compounds, affecting peak integration, especially with HME.

To demonstrate the capability for selective determination of the markers in the presence of expected interferences, a set of 15 VOCs representative of indoor air contaminants, and a set of 5 n-alkanes from C_{10}-C_{16} (similar to the range found in jet fuel) [11] was identified. The list of S/VOCs is given in the caption of Figure 4-8. A CS_2 solution of a mixture of these 20 compounds along with the two markers was prepared, and analyzed by GC-FID using a 6-m long capillary column with a PDMS stationary phase (0.25 mm i.d., SPB-1, 0.25 µm thickness, Supelco, Belafonte, PA) and He carrier gas at 3 mL/min. Note that 2,6-DNT was eliminated from the set of markers at this point because it was realized that its vapor concentration would be so much lower than those of the other two markers. Figure 4-8a shows the FID chromatogram. Peak assignments are based on individual runs of each component. As shown, the indoor air contaminants elute early, followed by the jet fuel model compounds, and the markers, consistent with a separation dictated primarily by analyte volatility (however the markers elute faster than expected due to their

polar structures). This reference chromatogram serves to document the complexity of the test mixture and the expected elution order on a non-polar column.

Using a 50-mL gas-tight syringe, headspace samples from the three flasks containing either the 20 interferences, DMNB, or 2,4-DNT were collected and injected slowly into a scrubbed air stream directed past the inlet of the prototype at ~ 100 mL/min, which was connected by a tee-fitting. The flasks had been allowed to sit for a few days to allow the headspace to come to equilibrium prior to sampling. The sample consisted of 5 mL of the headspace of the 20 VOC mixture, 5 mL of the DMNB headspace, and 20 mL of the 2,4-DNT headspace. The prototype analytical sequence was initiated via the laptop controller and it proceeded to sample this dynamic test atmosphere at 2.7 L/min for 22 sec, focus for 40 sec at 40 mL/min, stop the sampling pump and start the analytical pump with an associated pause for 5 sec, then heat the μF to inject, separate and detect the mixture at 3 mL/min. The column temperature program employed was the same as that described in the caption of Figure 4-3.

Figure 4-8b shows the traces for all four CR sensors in the array. Of the 22 compounds, only 7 appear in the chromatograms; the other 15 were, by design, not retained by the sampler and/or μF. Compounds with p_v values less than ~ 1.4 torr (n-decane) were effectively captured, transferred to the μF, and analyzed. As shown, DMNB and 2,4-DNT were completely resolved from the alkane interferences, and gave retention times of ~20 and ~45 sec, respectively. The entire mixture elutes within 60 sec, although it takes around 80 sec to reach baseline. The time to reach baseline, however, does not necessarily add extra time to the total analysis, as the analytical subsystem could be flushed while the next sample is collected by the high-volume sampler. The alkanes are also well resolved, and baseline separation between components is achieved.

Overall, good peak shapes are observed, except for 2,4-DNT which tails significantly. As seen in the sub-system test results, this can be due to the relatively low temperature at which the CR array is operated (70 ºC), wall adsorption in the Macor® lid, or finite dead volume in the detector cell. Note that 2,4-DNT is the least volatile compound in the mixture. Similarly broad bands would be expected for other compounds of similar volatility. The *fwhm* values were 2 and 12 sec for DMNB and 2,4-DNT, respectively. The values of R_s are 1.6 (DMNB-n-C_{11}), 1.3 (DMNB-n-C_{12}), and 1.7 (2,4-DNT-n-C_{13}). This degree of separation is more than adequate for determining the explosive markers, even if response pattern data are not considered. The overall analytical cycle time is ~ 122 sec distributed as follow: sampling (22 sec), focusing (40 sec),and analysis (60 sec).

Normalized response patterns were generated for DMNB, n-C13, and 2,4-DNT from data collected from the assembled prototype, as shown in Figure 4-9. This process involved first converting measured voltage response to ΔR/R using the following equation:

$$\frac{\Delta R}{R} = \frac{V_{meas.}}{gain \times V_{base} \times \left(1 - \frac{V_{base}}{V_{ref}}\right)} \qquad \text{Eq. 1}$$

where V_{meas} is the measured voltage response, gain is an instrumental quantity, V_{base} is the average baseline voltage and V_{ref} is the reference voltage. The ΔR/R values were then normalized to the highest responding sensor.

For both marker compounds, the HME-coated sensor yields the highest sensitivity. In addition, both of these response patterns differ significantly from the model fuel compound interference (*n*-C_{13}). The response patterns generated using the assembled prototype differ slightly from those obtained from the analytical subsystem [12]. This is attributed to a poorly functioning

C8 sensor in the prototype. Due to problems with carry-over in the sampler, quantitative analysis was not possible.

4.4. Conclusions

This is the first report of the characterization of a fully integrated and automated μGC prototype for analysis of explosive markers in vapor phase. Optimized for this application, the instrument relies on fast and selective preconcentration/injection, rapid, temperature-programmed μcolumn separation; and microsensor-array detection to analyze the explosive markers in the presence of a complex mixture of background VOCs. Although this study fell short of performing quantitative and reproducible analysis of the explosive markers using the prototype, the selectivity towards the explosive markers, achieved within a 2 min analytical cycle time, coupled with the capability for automated operation, demonstrate the potential of this instrument as an effective stand-off detection system of explosive markers in the vapor phase.

The use of on-column focusing reduced the net band broadening attributable to μF injection and microcolumn elution by 15-20%. Other options that could be explored in the future include the use of split-flow injection, which can reduce the mass injected into the microcolumn to narrow the elution band. Split injection, however, comes with a loss of sensitivity. The use of longer microcolumns coated with low-bleed stationary phases could be operated at higher isothermal temperatures or with temperature programming without affecting the total elution time or the R_s values between critical marker-interference pairs considerably. However, a limiting factor is the maximum operating temperature of the MPN-coated CR sensor. Even at 70 ºC, 2,6- and 2,4-DNT elute rather slowly through the detector cell, generating extra broadening.

Residual carry over in the sampler or interconnecting tubing precluded demonstrating reproducible quantification of the explosive markers. Maintaining the fluidic path at a higher minimum temperature (> 70 ºC), and heating the manifold will likely be necessary modifications to solve this problem.

In summary, this portable μGC has the potential to be an alternative to current systems for near-real-time, stand-off determinations of vapor-phase explosive markers. The lower cost of fabricating the μGC system, compared to commercial spectrometric methods, favor its use for routine continuous monitoring for explosives at airport security checkpoints.

12.4. References

1. Convention on the marking of plastic explosives for the purpose of detection, available at http://www.ciaonet.org/cbr/cbr00/video/cbr_ctd/cbr_ctd_33.html, accessed August 2012.
2. T. F. Jenkins, D. C. Leggett, T. A. Ranney, CREEL, special report 99-21, available at http://www.dtic.mil/cgi-bin/GetTRDoc?AD=ADA373402, accessed October, 2012.
3. R. P. Murrmann, T. F. Jenkins, D. C. Leggett, CREEL, special report 158, available at http://www.dtic.mil/cgi-bin/GetTRDoc?AD=ADA040632, accessed October, 2012.
4. M. P. Rowe, K. E. Plass, K. Kim, C. Kurdak, E. T. Zellers, A. J. Matzger, Single-phase synthesis of functionalized gold nanoparticles, *Chem. Mater.*, 16, (2004), 3513-3517.
5. G. Serrano, T. Sukaew, E. Zellers, Hybrid preconcentrator/focuser module for determinations of TNT marker compounds with a micro-scale gas chromatograph, *J. Chrom. A., accepted.*
6. S. Reidy, G. Lambertus, J. Reece, R. Sacks, High-performance, static-coated column silicon microfabricated columns for gas chromatography, *Anal. Chem.*, 78, (2006), 2623-2630.
7. G. Serrano, S. M. Reidy, E. T. Zellers, Assessing the reliability of wall-coated microfabricated gas chromatographic separation columns, *Sens. Actuators. B.*, 141, (2009), 217-226.
8. R-S. Jian, R-X. Huang, C-J. Lu, A micro GC detector array based on chemiresistors employing various surface functionalized monolayer-protected gold nanoparticles, *Talanta*, 2012, 88, 160-167.
9. W. H. Steinecker, M. Rowe, A. Matzger, E. T. Zellers, Chemiresistor array with nanocluster interfaces as a micro-GC detector, *Proc. Transducers 03'*, Boston, MA, USA, June 2003, pp. 1343-1346.
10. Q. Zhong, W. H. Steinecker, E. T. Zellers, Characterization of a high-performance portable GC with a chemiresistor array detector, *Analyst*, 134, 283-293.
11. K. Shafer, C. Jahn, P. Sturm, B. Lechner, M. Bacher, Aircraft emission measurements by remote sensing methodologies at airports, *Atmos. Environ.*, 2003, 37, 5261-5271.

12. E. T. Zellers, G. Serrano, H. Chang, and L. K. Amos, A micro gas chromatograph for high-speed determinations of explosive markers, *Proc. Transducers 11'*, Beijing, China, June 5-9, 2082-2085.

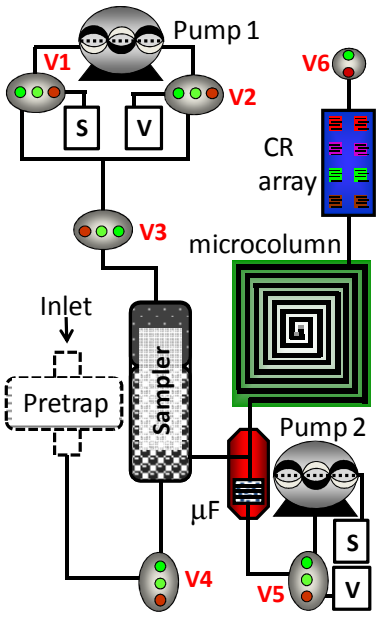

Figure 4-1. Fluidic pathway diagram of the INTREPID-II µGC prototype.

S = scrubber, V = vent. V1, V2, etc. are valves.

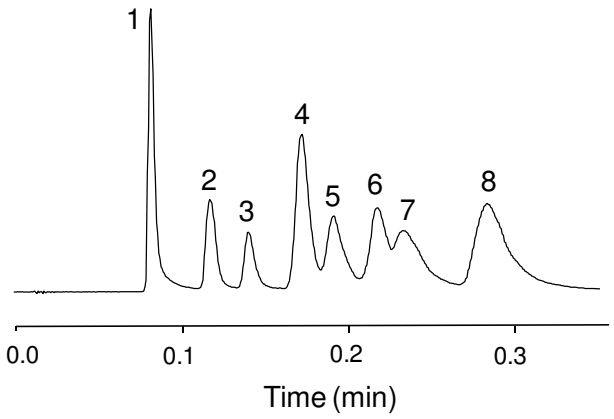

Figure 4-2. 22-s temperature programmed separation of markers and alkane interferences using 1-m μcolumn mounted within the oven of a conventional GC and connected to the split/splitless injector and FID via passivated capillaries. Conditions: air carrier gas; 3 mL/min; 100:1 split injection; 120 °C (initial), 4 °C/s to 140 °C, 1 °C/s to 160 °C, 4 °C/s to 180 °C, hold for 10 s (total = 20 s). Compounds: 1, CS_2 (solvent); 2, DMNB; 3, n-tridecane; 4, n-tetradecane; 5, 2,6-dinitrotoluene; 6, n-pentadecane; 7, 2,4-dinitrotoluene; 8, n-hexadecane.

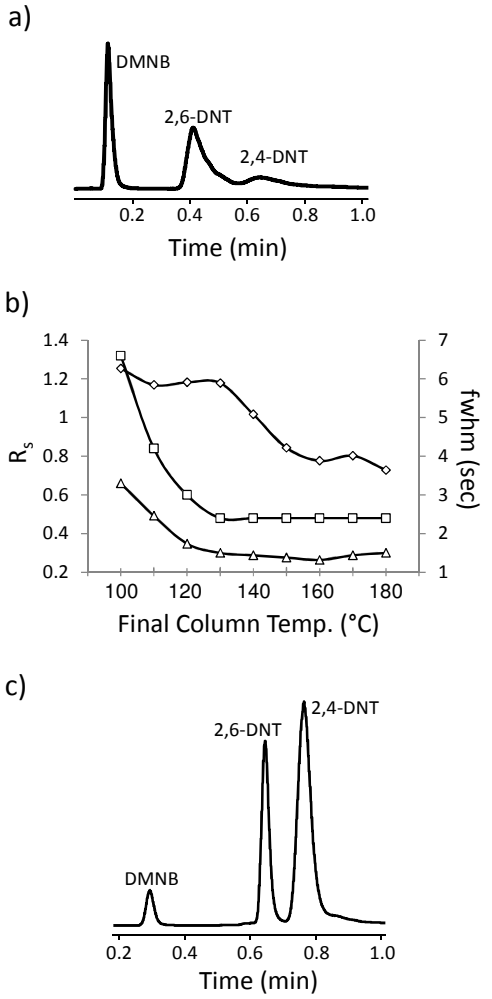

Figure 4-3. a) 120 °C isothermal separation of target compounds illustrating broad peaks and somewhat low poor resolution (conditions: µF injection to microcolumn; ECD; 3 mL/min N_2 carrier gas. b) Effect of final temperature following OCF at 70 °C on resolution (R_s) between 2,4- and 2,6-DNT (diamond) and *fwhm* of 2,6-DNT (triangle) and 2,4-DNT (square). c) Chromatogram showing marker separation generated using OCF and temperature program that maximizes resolution between 2,4- and 2,6-DNT while minimizing peak width (conditions: 70 °C for 20 s, ramp at 8 °C/s for 7.5 s, hold at 130 °C for 32.5 s; µF injection to microcolumn; ECD; 3 mL/min N_2 carrier gas.

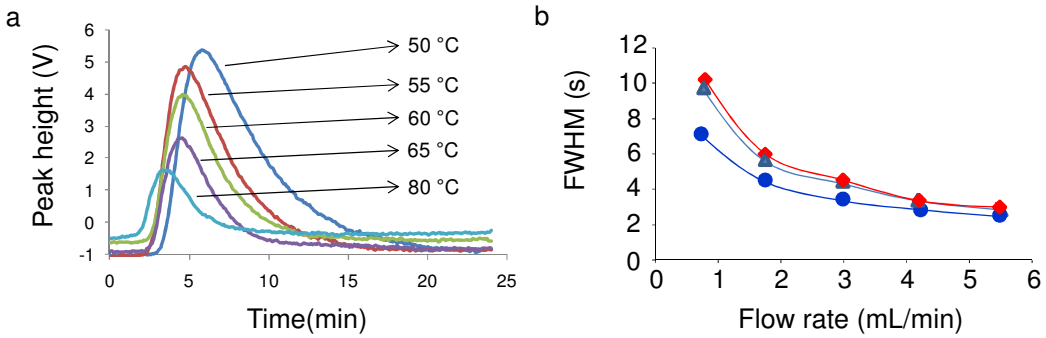

Figure 4-4. a; Overlaying chromatograms of the sensor response to 2,4-DNT at several sensor temperatures. Conditions: 1 mg/mL (CS_2, 0.5 µL injection, splitless, 250 °C inlet), 30-m DB-1 column, kept isothermal at 110 °C, carrier gas: He. b; 2,4-DNT *fwhm* at different flow rates using an FID detector (circle), and two CR array sensors at 70 °C, C8 (diamonds) and OPH (triangles). Conditions: 0.25 mg/mL (CS_2, 0.5 µL injection, 100:1 split, 225 °C inlet), 1-m µcolumn kept isothermal at 120 °C, carrier gas: N_2.

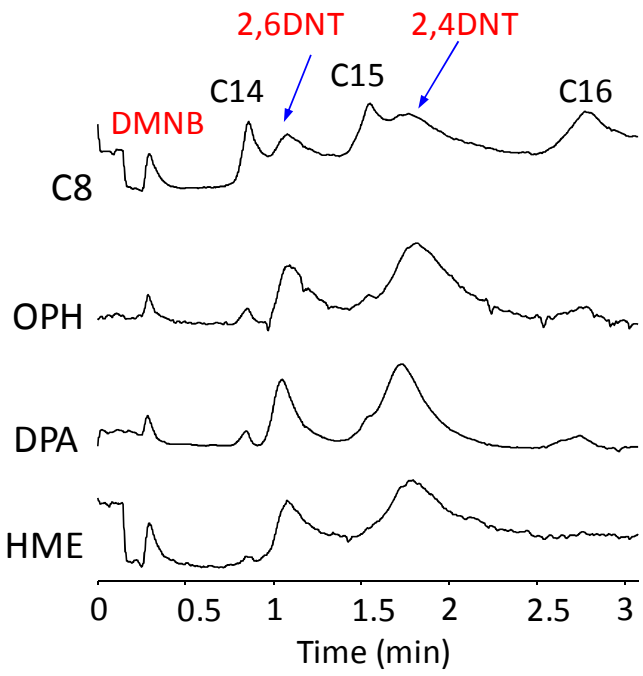

Figure 4-5. Chromatogram obtained using the analytical subsystem composed of a 1-m µcolumn and a CR sensor array. Compounds: DMNB, n-tetradecane (C14), 2,6-dinitrotoluene (2,6-DNT), n-pentadecane (C15), 2,4-dinitrotoluene (2,4-DNT), n-hexadecane (C16). Conditions: microcolumn temperature = 120 °C ; CR array temperature = 70 °C; 0.5 µL, 100:1 split injection, GC inlet at 225 °C, 1.2 mL/min flow rate, purified dry air carrier gas.

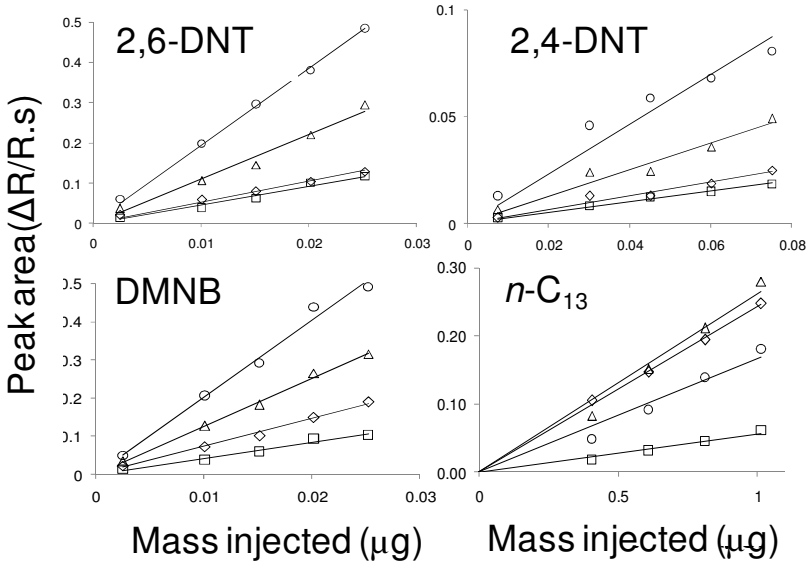

Figure 4-6. Calibration curves generated for 2,6- and 2,4-DNT, DMNB and n-tridecane using the analytical subsystem (µF, 1-m µcolumn, and CR array) connected to a bench-scale GC inlet, and liquid standards of the compounds in CS_2. Concentrations were confirmed by independent GC/FID analysis. Symbols designate MPN materials. Circles for HME, triangles for OPH, diamonds for C8 and squares for DPA.

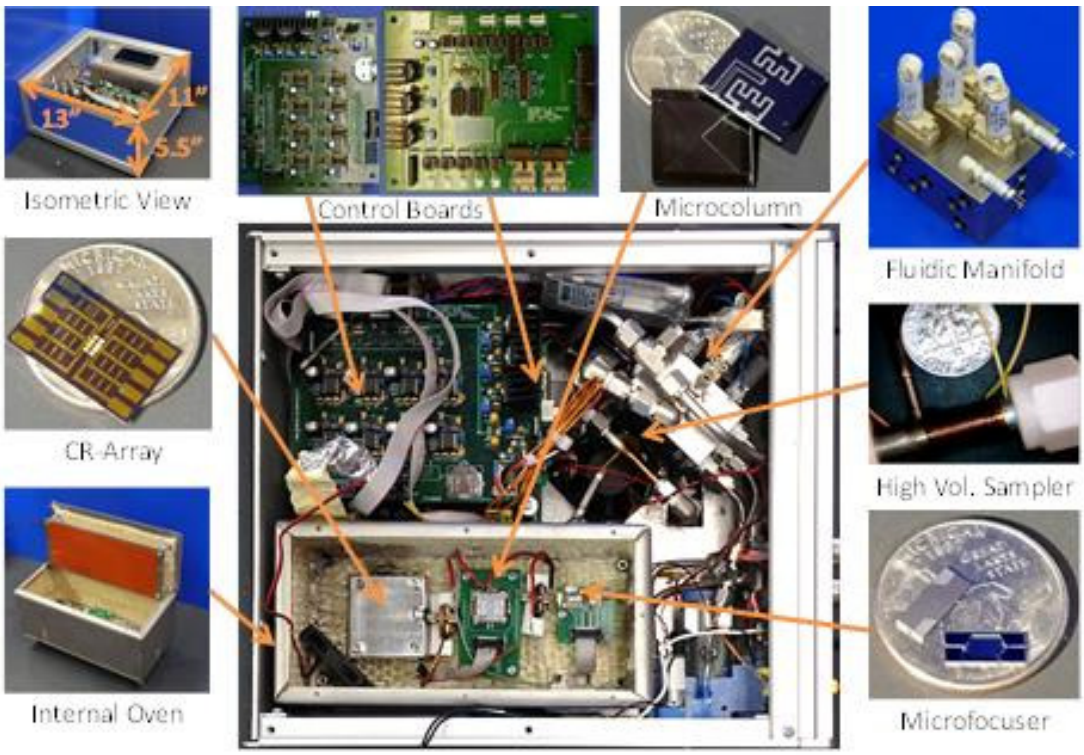

Figure 4-7. Photographs of the INTREPID-II μGC prototype (center) and the primary main components (periphery, as labeled).

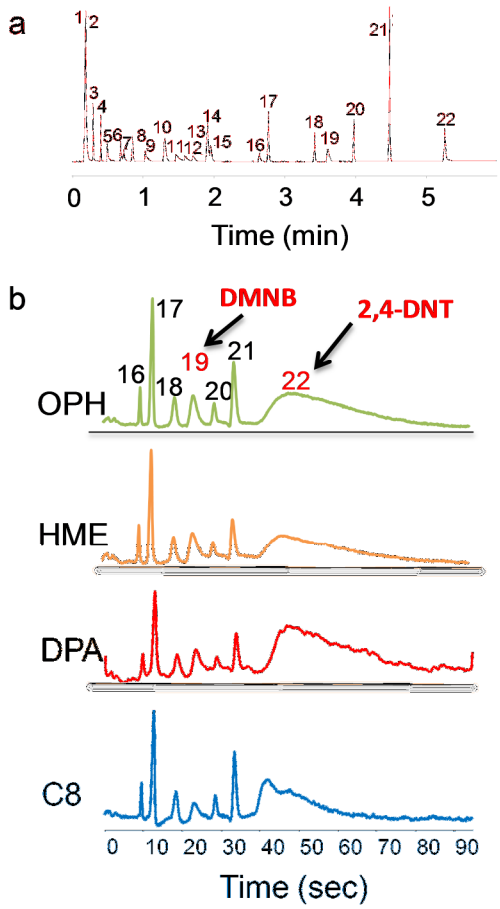

Figure 4-8. (a) 1-D chromatogram of a 22-component mixture (including DMNB and 2,4-DNT). Conditions: 6-m, 0.25 mm i.d. PDMS (0.25 μm thick PDMS); 40 °C (10 s) to 160 °C (60 s) at 30 °C/min; He carrier gas; 3 mL/min flow rate; FID. (b) Chromatograms from the four CR microsensors generated from the analysis of a 1 L air sample spiked with DMNB and 2,4-DNT and 20 interferences. Fifteen of the interferences were not trapped by the PCF module and therefore do not appear in the chromatograms. Compounds: 1, benzene; 2, 1-propanol; 3, n-heptane; 4, toluene; 5, n-octane; 6, hexanal; 7, 2-hexanone; 8, isoamyl alcohol; 9, m-xylene; 10, 2-methyl-2-hexanol; 11, 2-heptanone; 12, n-nonane; 13, cumene; 14, heptanal; 15, 1-hexanol; 16, octanal; 17, n-decane; 18, n-undecane; 19, DMNB; 20. n-dodecane; 21, n-tridecane; 22, 2,4-DNT.

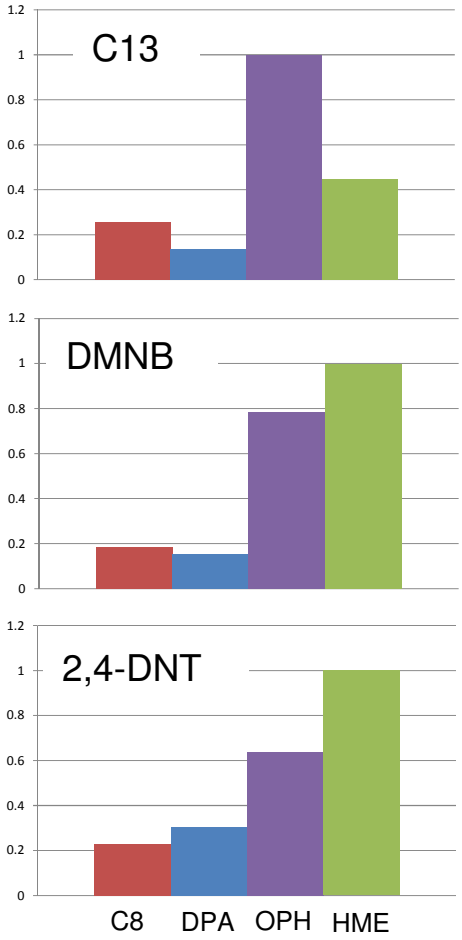

Figure 4-9. Normalized response patterns for 2,4-DNT, DMNB and n-tridecane, using CR array. Unique response patterns are observed for the marker compounds as compared to the alkane (model fuel compound) interference.

APPENDIX II

LabVIEW program for control, data acq., and alarm determination

The LabVIEW program used to control the INTREPID I prototype had all of the essential elements required for autonomous operation of the core analytical components (μF, μcolumn, μsensor array) and for display of the responses from the array. But the sequencing of the pumps and valves was controlled with a separate program. For the INTREPID II prototype, it was necessary to consolidate all code required for autonomous operation. Toward that end, we developed and debugged new LabVIEW modules, and reworked/re-bundled the component LabVIEW routines into a package that permits continuous autonomous operation for multiple cycles and display of instrument status. We also strove to incorporate additional features such as peak finding, decision-making on the fly, and exporting of the data to a separate package for peak integration, multivariate curve resolution, vapor recognition and quantification (from sensor-array responses), data reduction, and final target determinations. The software was developed and configured to afford the least cumbersome and fastest approach to determinations of the targets. The goal was a menu-driven, user-adjustable, graphic-user-interface for operating the INTREPID II μGC and acquiring chromatographic data from all sensors and displaying results.

To allow automated as well as manual operation of the instrument, the structure of the code was revised. The original routine-based code structure was replaced by an event-based one, where a precisely timed main loop runs acquisition and control tasks in background, while a secondary loop waits for user inputs or programmed sequences and then commands task states in the main loop. Additional advantages of this structure are the possibility to drive controls independently and to customize the operation sequences of the instrument after the development stage. A copy of this revised code was debugged with the Intrepid I circuit boards. The revised code, as well as new

functionalities, worked as expected. Revised codes were eventually tested with the new INTREPID II boards.

One of the new functionalities is a μF initial temperature control, which allows the temperature of the μF to be set at a slightly elevated level via the integrated heater rather than being controlled by the mini-oven of the prototype. This function employs a PID control routine that generates a PWM signal at 50Hz. The PID control routine was integrated with the previously existing on/off heating control. It deactivates itself automatically when the on/off control is activated, which results in fast heating and also rapid adjustment of baseline temperature. This new feature was useful for implementing the on-column focusing technique for improving the resolution of explosive markers from potentially interfering vapors. It enables the μF to be heated to 70-80 °C, for example, while the microcolumn remains unheated. Figure 4-S2 shows the temperature profile of a μfocuser at an initial temperature of 75 °C, and then at a final temperature of 250 °C achieved in less than a second.

Acquisition channels and corresponding graphs were added for monitoring the sampler and oven temperatures. Sampler and capillary interconnection temperatures are acquired using thermocouples while the temperatures of the carrier boards are measured using IC thermistors. A closed-loop control for the heating of the sampler was implemented in order to achieve a heating rate that would permit reaching 250ºC in 15 sec. A pair of digital outputs from the DAQ switches on/off two voltages, one of 17V to achieve fast initial heating, and one of 9V for reducing ripple.

A set of manual controls for turning on and off valves and pumps independently was incorporated into the LabVIEW front panel control GUI. As well, a set of controls for programming automation of the instrument was added in the form of a time table. A routine executes the programmed sequences by triggering corresponding controls accordingly. It allows

an “Auto” mode for one time execution of the sequence and “Continuous” mode for a loop execution. Figure 4-S3 provides a screenshot of the control panel relevant to these functions. In order to allow integration of generated code into an executable stand-alone program, a set of controls was added for setting up workspace variables like RTD calibration parameters, heating temperatures for sampler and μfocuser, and valve default states.

Algorithm for critical peak finding and pattern recognition

Significant progress was made in developing algorithms to extract information about the identities of the compounds in partially overlapping binary peaks generated by the INTREPID prototype. These techniques employ multivariate curve resolution (MCR) methods for this purpose, specifically adaptive least squares in conjunction with evolving factor analysis (ALS-EFA). ALS and EFA have been coupled together as a way of determining how many components are contributing to an apparent binary peak cluster and to extract their separate response patterns for subsequent pattern recognition by principal components regression. The context for this has been a desire to perform reliable quantitative analysis, which requires precise pattern recovery. But the procedures involved are time consuming and must be done off-line after the data has been collected, stored, downloaded, and transferred to Excel or GRAMS.

For the INTREPID-II field prototype, there is a need to make determinations more rapidly so that decisions about the presence of explosives could be made in near-real-time. In order to move closer to such an operating scenario, it was necessary to develop an abbreviated data management routine to allow a decision to be made more rapidly as to whether explosives are present or not. Although not complete, progress toward this goal was made. For example, it was thought that it would be possible to focus on the retention time windows where each of the 2 (or 3) targets elute and if measurable signals (peak heights) were found in all three of these windows, this

would trigger a 'cautionary' alarm that would prompt a more thorough data analysis. Such a decision might also be based on the presence of only two such signals or even just one. This might be sufficient, in a screening operation, to detain an individual or a piece of luggage while more in-depth analyses are performed. For the latter, signal intensities could be assessed and algorithms developed to perform rapid pattern recognition to possibly confirm or refute the possibility of explosives. Should this second-level of analysis suggest the presence of explosives, then a full analysis could be performed or the analysis repeated.

A program was developed for off-line analysis of a given sensor data set, capable of finding relevant peaks and calculating their height and position (retention time). The program is based on a peak/valley detection tool that performs quadratic curve fitting after proper signal filtering. This function along with a decision making routine could be automated and incorporated into the main LabVIEW program. The general approach is illustrated in Figure 4-S4.

In summary, the LabVIEW code was developed and integrated into a final, coherent program with user definable settings, where appropriate, that permits single analyses or a continuous series of analyses (the number of which would be user-selected) to be run automatically prior to subsequent user intervention. Using the peak finding algorithm, it will eventually be possible to implement an alarm function to indicate that there is a peak at each of several possible characteristic retention times with characteristic patterns to merit a cautionary alarm, so that the person or item being analyzed could be investigated more carefully.

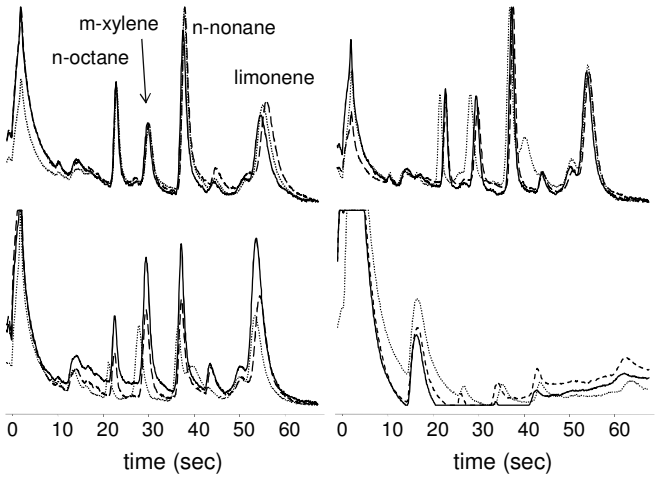

Figure 4-A1: Results of fully automated operation of INTREPID field prototype for a series of VOCs. Five consecutive sampling/analysis cycles were completed, though only three are shown for clarity. Good retention time reproducibility is evident across all sensors, and good peak height reproducibility is seen with respect to sensor coating. Note: The peak at around 5s in each chromatogram is likely due to water vapor. The peak at 18s is an unknown contaminant. See text for conditions.

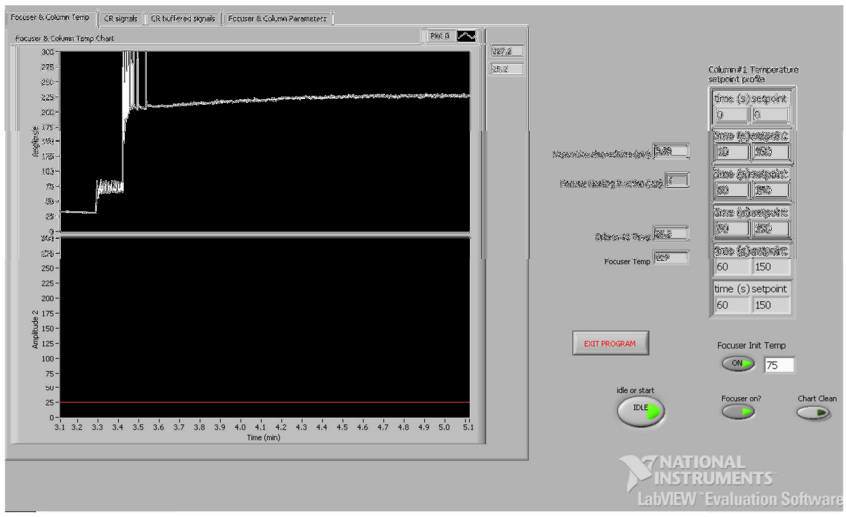

Figure 4-A2. Labview code with the new temperature control for the μF

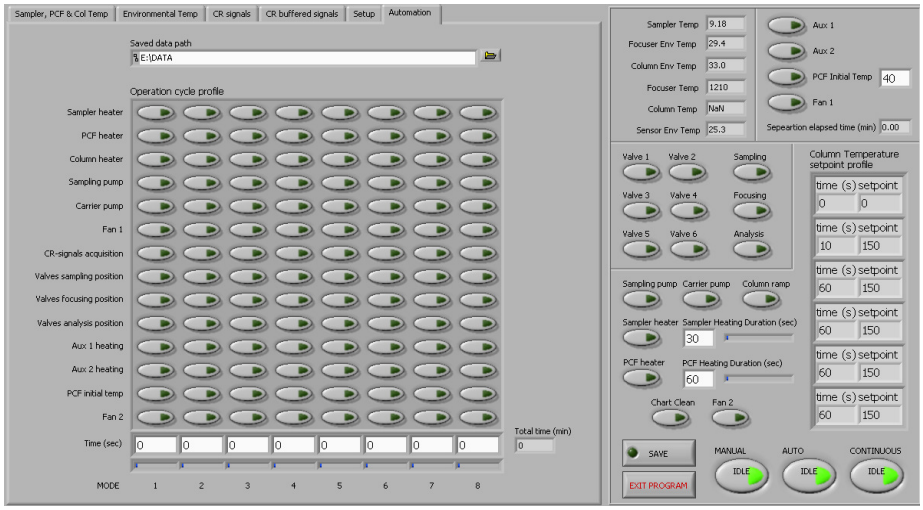

Figure 4-A3. Screenshot of Labview controls for automated and manual operation

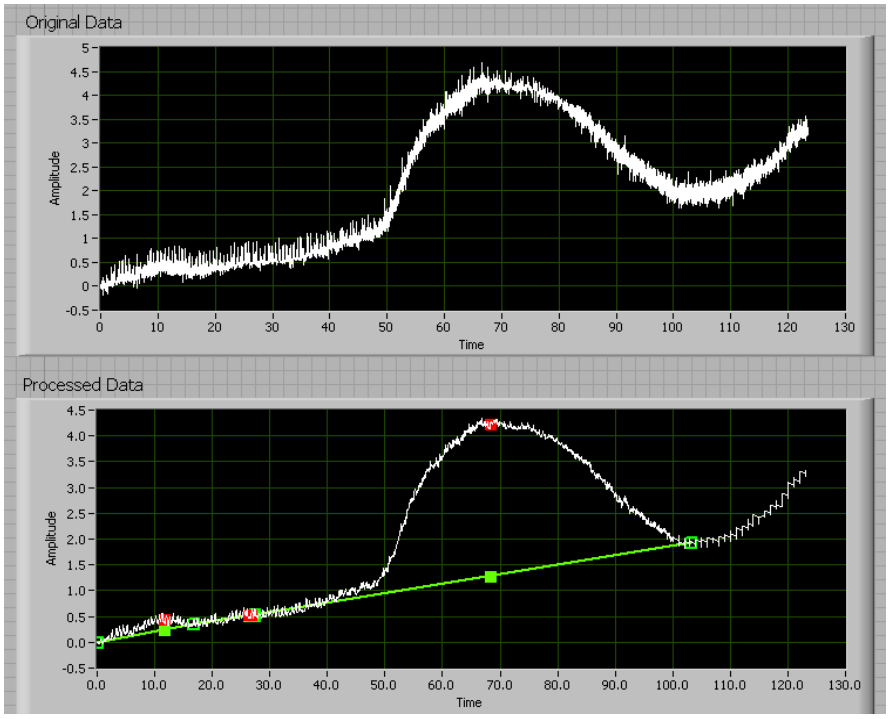

Figure 4-A4. Screen shots of LabVIEW program for relevant peak detection

CHAPTER V

COMPREHENSIVE TWO-DIMENSIONAL GAS CHROMATOGRAPHIC SEPARATIONS WITH A MICROFABRICATED THERMAL MODULATOR

5.1 Introduction

Numerous reports have appeared over the past decade or so on micro-scale gas chromatograph (μGC) components [1-13], subsystems [14-16], and systems [17-25], consisting of one or more microfabricated Si devices. The low power requirements, small size, and eventual low production cost of μGC systems favor their use in field or clinical settings for measuring volatile and semi-volatile organic compounds (SVOC), such as explosive markers, chemical warfare agents, indoor air pollutants, and breath biomarkers of disease or toxic chemical exposure. Although the scaling laws governing GC separations generally favor miniaturization [26], inherent limitations on the maximum length and minimum diameter of the (micro)columns, as well as the minimum injection bandwidth, place limits on the achievable peak capacity (n_p) and resolution (R_s). One approach to relieving these constraints on performance entails the use of comprehensive two-dimensional gas chromatography (GC×GC).

GC×GC is a highly effective method for separating the components of complex mixtures of (S)VOCs [27]. A junction-point modulator couples a relatively long first-dimension (^{1}D) column to a relatively short second-dimension (^{2}D) column having a different stationary phase and, thereby, different retention properties. As each compound elutes from the ^{1}D column it is re-injected in a series of narrow bands that elute through the ^{2}D column rapidly enough to preserve

the ^{1}D separation. Pneumatic modulation is achieved by tapping a second carrier gas source into the junction point and toggling a series of valves that transfer the effluent from the ^{1}D column to the ^{2}D column at very high frequency [28, 29]. Re-injection bandwidths as narrow as 22 ms can be obtained but little or no focusing occurs, and therefore the peak amplitude enhancement (*PAE*; i.e., the modulated/unmodulated peak-height ratio) is generally quite limited [29]. Thermal modulation is achieved by alternately bathing a small section of capillary at the junction point in a cooled gas to trap and focus peak segments from the ^{1}D column and then heating to transfer them to the ^{2}D column [30-34]. Re-injection bandwidths as narrow as 50 ms and *PAE* values as high as 70 have been reported by virtue of the refocusing that occurs with the thermal modulator (TM) [27, 32, 33]. Plotting the ^{1}D retention times against the ^{2}D retention times provides a 2-D chromatogram that conveys the net differential retention of the mixture components on the two columns.

The primary difficulties faced in trying to miniaturize GC×GC systems with commercial TM subsystems are the need for large quantities of consumable cooling fluids or the power demands for both heating and cooling, which can be on the order of Kw [32b, 33, 34]. As part of an on-going effort concerned with the development of μGC systems and components in our laboratories [1,4,7,8,14-16,18,21,22,24,25] we recently described a microfabricated TM (μTM) that operates with relatively low power and without cryogenic fluids [35-37]. The μTM chip consists of two series-coupled, convolved-square-spiral, deep-reactive-ion-etched (DRIE) Si microchannels (stages) with an anodically bonded Pyrex cap, a crosslinked PDMS wall coating, and individual thin-metal-film heaters and temperature sensors. The chip is mounted on a thermoelectric cooler (TEC), which is used for focusing. Highlights of that work include modulated peaks with full-width-at-half-maximum (*fwhm*) values as low as 70 ms (for n-heptane) and *PAE* values as high as 50. Testing performed to date, however, entailed only a ^{1}D column so

that the modulated peaks emerging from the μTM could be characterized without the influence of a ^{2}D column.

In this article, we describe a GC×GC system that uses a μTM of similar design to that reported previously. Relatively short commercial ^{1}D and ^{2}D capillary columns are used in anticipation of developing a μGC×μGC system for (S)VOCs. The effects of varying the stage temperatures, modulation period, stage-heating offset period, and volumetric flow rate are examined with respect to several performance metrics using a small set of VOCs as test analytes. The reproducibility of the 2-D separations provided under a given set of conditions is examined and then a structured chromatogram is produced and assessed. Finally, a fast GC×GC 21-component VOC mixture separation is presented. The implications of the results for using this type of μTM in benchscale GC×GC systems and in portable μGC×μGC systems for fast analysis of (S)VOC mixtures are considered.

5.2 Experimental

5.2.1 μTM preparation

The design, thermal analysis, and fabrication of the μTM device have been described previously [35, 36]. Figure 5-1a shows a photograph of the device (see refs. 35 and 36 for dimensional diagrams). The 13×6 mm μTM chip consists of two square-spiral, boron-doped Si microchannels, 4.2 cm (stage 1) and 2.8 cm (stage 2) long, with cross-sections of 250 (w) × 140 (h) μm and wall thicknesses of 30 μm. The microchannel dimensions were chosen on the basis of the modulator reported by Libardoni, et al. in Ref. 34 and prior work by that group cited in that article. A 100-μm thick Pyrex cap is anodically bonded to the top surface, sealing the microchannels and providing additional mechanical strength to the Si frame. There is a 0.5-mm long microchannel

interconnection segment between the two stages. Connections to upstream and downstream capillaries are made at opposing sides of the rim. Four Ti/Pt resistive heaters and temperature sensors are patterned on the Pyrex surface; one set beneath each stage and another set beneath the inlet and outlet ports on the rim.

Two 5-cm long sections of deactivated fused-silica capillaries having 250 μm i.d. and 100 μm i.d., were connected to the inlet and outlet ports, respectively, with epoxy (Hysol Epoxy Patch 1C, Rocky Hill, CT). The interior walls of the microchannels (and connecting capillaries) were coated with a 0.3 μm thick cross-linked film of polydimethylsiloxane (PDMS, OV-1, Ohio Valley, Marietta, OH) from a 1:1 n-pentane:dichloromethane solution (0.6% w/v PDMS, 0.005% w/v dicumyl peroxide), using a static coating and thermal cross-linking method described previously [7]. The μTM chip was then mounted and wirebonded to a custom printed circuit board in proximity to an underlying thermoelectric cooler (TEC) as described in the Supporting Information accompanying this article.

5.2.2 Performance Testing

The μTM-TEC testing platform was placed inside the oven of a bench-scale GC (Model 6890, Agilent Technologies, Santa Clara, CA). Resistance values of the integrated temperature sensors were calibrated using the GC oven. The TEC was operated continuously at an applied power of 21 W, which yielded a minimum stage temperature, T_{min}, of −40 °C with the rim heaters deactivated and an ambient temperature of 23 °C. Reducing the power to the TEC allowed for higher T_{min} values. Modulations entailed applying 100-ms voltage pulses independently to each stage heater through two solid-state relays (D1D12, Crydom, San Diego, CA). The voltage applied to each stage was adjusted manually between 55 and 60 V to achieve the desired maximum

stage temperature, T_{max}, which ranged from 195 to 250 °C. A custom Visual C# program was used to control the timing of the applied voltages, as well as to read the temperature sensors via a DAQ card (NI USB-6212, National Instruments, Austin, TX) installed on a laptop computer. A constant voltage was applied independently to each rim heater and adjusted to maintain the ports at the ambient temperature when the TEC was on.

Inlet and outlet capillary sections were connected to commercial fused-silica capillary columns by means of press-tight connectors. The ^{1}D column was a 6-m long, 0.25-mm i.d. capillary, with 0.25-μm thick stationary phase of PDMS (Rtx-1, Restek Corp., Bellefonte, PA) and the ^{2}D column was a 0.5-m long, 0.1-mm i.d. capillary with a 0.1-μm thick stationary phase of polyethylene glycol (PEG, Rtx-Wax, Restek). The temperature of the ^{1}D column corresponded to that of the GC oven. The ^{2}D column was wrapped with insulated Cu wire (100 μm o.d., EIS, Inc., Atlanta, GA) and then heat-resistant thin polyimide tape (McMaster Carr, Santa Fe Springs, Ca). A fine-wire thermocouple (Type K, Omega, Stamford, CT) was placed between the capillary and heater coil. For all tests the ^{2}D column was maintained at ~80 °C. Note that the outlet capillary segment affixed to the μTM chip was coated with PDMS and was at oven temperature for all testing. The distal end of the ^{2}D column was connected to the FID via a 5-cm segment of deactivated fused silica capillary (100 μm i.d.). For some testing, the ^{2}D column was bypassed and the TEC was deactivated so that the ^{1}D peak widths could be measured.

Test compounds were > 98% pure (Sigma-Aldrich, Milwaukee, WI) and used without further purification. Vapor mixtures were prepared by injecting 1 μL of each component into a 10-L Tedlar bag (SKC Inc., Eighty-Four, PA) filled with a known volume of dry N_2. A sample of this test atmosphere was drawn by a small diaphragm pump (UN86, KNF Neuberger, Trenton, NJ) through a 112-μL sampling loop connected to a six-port valve. The valve and loop were housed in

a heated (80 °C) enclosure on the GC chassis. Actuating the six-port valve injected the contents of the loop to the ^{1}D column of the GC×GC subsystem via a short section of deactivated fused-silica capillary. Using He as the carrier gas, the volumetric flow rate, F, was adjusted by varying the GC inlet pressure and was measured at the end of the ^{2}D column with a bubble flow meter.

The data sampling rate and temperature of the FID were 200 Hz and 250 °C, respectively. ChemStation software (Rev.B.01.01, Agilent Technologies, Santa Clara, CA) was used for data acquisition, GRAMS32 (Version 6.0. ThermoScientific, Pittsburgh, PA) was used for 1-D data processing, and GC Image (Rev 2.2, Zoex, Houston, TX) was used for 2-D data processing and display of 2-D chromatograms.

5.3 Results and Discussion

Several μTM operating variables must be set for a GC×GC analysis, and each has an effect on performance. The stage-heating offset, O_s, is the time delay between heating of the first and second stage heaters, which can affect sample transfer efficiency. The modulation period, P_M, is the time between successive first-stage heating events (i.e., modulations), and it must be considered together with the retention time, t_R, on the ^{2}D column which, in turn, is affected by the F value, ^{2}D column temperature, and the analyte-stationary phase interactions. The values of T_{min} and T_{max} affect the efficiencies of trapping and remobilization, and the rates at which T_{min} and T_{max} are achieved affect the minimum achievable P_M as well as the re-injection bandwidth for the ^{2}D column separation. The rate at which T_{max} is reached for the μTM design used here is determined by the magnitude and duration of the applied heater voltage, and was as high as 2300 °C/s for the range of T_{min} and T_{max} values studied. The rate at which T_{min} is reached is determined by the thermal mass of the stage and the net thermal resistance of all heat dissipation pathways [35].

Although the thermal time constant for cooling the μTM was ~ 0.34 s, regardless of T_{max}, it required ~3-4 s to fully return to T_{min}.

Thermal crosstalk between the rim and each stage and between the two stages can also affect performance. If no voltage were applied to the rim heaters, then the inlet and outlet ports would reach temperatures similar to T_{min}, creating a cold spot in the sample transfer path. By applying a constant bias in the range of 2-3 V to each rim heater, the temperatures of the inlet and outlet ports were adjusted to match that of the GC oven (i.e., 25 or 33 °C). The inter-stage thermal crosstalk was ~7-10% for the μTM design used in this study under the conditions employed. This is as much as 3% higher than that for the device described in Ref. 36 owing to the shorter interconnection microchannel employed (i.e., 0.5 mm vs. 1 mm). As a result, heating the first stage led to a transient increase of ~16-19 °C in the value of T_{min} for the second stage during each modulation over the ranges of T_{max} and T_{min} values studied. Increasing O_s from the default value of 600 ms to 1800 ms prolonged the transient temperature and reduced the trapping efficiency of the 2nd stage. Reducing O_s to 200 ms gave performance similar to that for O_s = 600 ms, indicating that inter-stage heat transfer is rapid.

Performance was assessed with respect to the *fwhm* of the primary modulated peaks, the t_R values and critical-pair resolution in the ^{2}D column (R_{s2}), the modulation ratio (M_R, i.e., number of detectable ^{2}D peaks per ^{1}D peak), n_p, and the extent of breakthrough. The latter phenomenon was assessed qualitatively by careful inspection of the 2-D chromatograms. Breakthrough occurs when the trapping capacity of the μTM is exceeded in one or both stages. It is accompanied by the appearance of vertically broadened signals in the 2-D chromatogram at ^{1}D retention times that are earlier than expected, and it results in unpredictable ^{2}D retention times. Wrap-around occurs when P_M is shorter than the retention time on the ^{2}D column. It results in compounds eluting in a later

modulation cycle at an unpredictable, though reproducible, ^{2}D retention time. R_{s2} is defined as (t_{R2} - t_{R1})/w_A, where t_{R2} and t_{R1} are the ^{2}D retention times of adjacent compounds, assuming co-elution in the first dimension, and w_A is the average base peak width of the primary modulated peaks [38]. Values of R_{s2} for the ("critical") n-octane/hexanal pair were used to compare the performance under certain operating conditions.

The peak capacity represents the hypothetical number of perfectly spaced peaks that could be separated at a specified value of R_s: $n_p = 1 + N^{1/2}/(4R_s)\ln(t_{Rn}/t_M)$ [38], where N is the plate number derived from the expression $5.545(t_R/fwhm)^2$, $R_s = 1$ for this study (arbitrary), and t_{Rn} is retention time of the last retained peak. For GC×GC separations, $n_{p,GC\times GC}$ is the product of the peak capacity for each dimension, i.e., $n_{p1} \times n_{p2}$,[27] and P_M is used instead of t_{Rn} for the ^{2}D column [34].

5.3.1 Modulator temperatures

The influence of T_{min} and T_{max} on performance was evaluated using the following seven VOCs, the boiling points (*bp*) of which range from 80 to 174 °C: benzene, isoamyl alcohol, hexanal, n-octane, 2-methyl-2-hexanol, 2-heptanone, and n-decane. The values of O_s, P_M, and F used initially were 0.6 s, 6 s, and 0.9 mL/min, respectively. Four different combinations of T_{min} and T_{max} were tested; as the value of T_{min} was adjusted the corresponding value of T_{max} was also adjusted so as to maintain a span (i.e., $\Delta T = T_{max} - T_{min}$) of 220-230 °C.

For the first tests, with T_{min} = -27 °C and T_{max} = 195 °C, the ^{1}D column temperature was 25 °C and the 2-D chromatogram in Figure 2a was obtained. M_R values were between 2 and 3 for all compounds, all ^{2}D t_R values were < 2.5 s, R_{s2} was 1.7, and the separation required 4.4 min. Importantly, the most volatile test compound, benzene, was trapped efficiently in the μTM under these conditions. The ^{2}D t_R values of the polar compounds were generally larger than those of the

hydrocarbons, as expected, and the *fwhm* value of the primary modulated peak of each compound ranged from 82 ms (n-octane) to 300 ms (n-decane). The tailing observed along the ^{2}D axis could arise from any of several of factors, including the low value of T_{min}, the relatively thick PDMS wall coating in the μTM, and the short segment of downstream interconnecting capillary, which was at the oven temperature of 25 °C. The horizontal band apparent in most of the Figure 5-2 panels has a retention time similar to that of n-octane in the ^{2}D column, and can be ascribed to a small amount of bleed arising from decomposition of the PDMS in the μTM each time it is heated.

For the second test condition (Figure 5-2b), the GC oven (^{1}D column and capillary interconnect) temperature was increased to 33 °C, and the lowest T_{min} value that could be maintained was -20 °C. The value of T_{max} was therefore increased to 210 ºC. Under these conditions, breakthrough of benzene occurred; it eluted from the ^{2}D column as a broadened signal in the modulation cycle preceding that in which it was expected, and gave an anomalous ^{2}D t_R value of ~5.4 s. This can be attributed to the inter-stage thermal crosstalk, which led to a transient increase in the second-stage T_{min} value to −1°C during each modulation and reduced the trapping capacity for benzene. The ^{2}D t_R and M_R values of the remaining test compounds were similar to those in Figure 5-2a, but the ^{1}D retention times were shorter due to the higher ^{1}D column temperature. In addition, there was less ^{2}D peak tailing due to the higher T_{min}, T_{max}, and interconnect temperatures; values of *fwhm* of the primary modulated peaks decreased slightly for the more volatile compounds (e.g., 72 ms for n-octane) and significantly for the less volatile compounds (e.g., 197 ms for n-decane). The R_{s2} value increased to 2.4 while the separation time decreased to 2.9 min.

For the data shown in Figure 5-2c, T_{min} was increased to 0 ºC (transient second-stage T_{min} = 16 °C) and T_{max} was increased to 230 °C while maintaining the column temperatures as in the

previous run. In this case, both benzene and n-octane showed evidence of breakthrough from the second stage, and *fwhm* values increased 2- to 3-fold for all other compounds except n-decane, for which *fwhm* decreased by ~10% (i.e., 180 ms) in spite of the higher value of T_{min}. Apparently, the increase in *fwhm* for the four other compounds arises from a reduction in focusing within the second stage of the modulator and a consequent increase in the re-injection bandwidth. Accordingly, the ^{2}D t_R and M_R values, and total separation time were the same as those for Figure 5-2b. Due to n-octane breakthrough, R_{s2} could not be calculated. The separation required < 3 min.

For T_{min} = 20 ºC (transient second-stage T_{min} = 35 °C) and T_{max} = 250 °C, all compounds except for n-decane broke through the modulator (data not shown). The *fwhm* of n-decane remained at 180 ms, suggesting that these conditions would be suitable for compounds of similar and somewhat lower volatility than n-decane. Note that *fwhm* for n-decane did not change upon reducing T_{max} to 210 ºC, which indicates that the re-injection bandwidth was not limited by this factor.

From the preceding results, values of T_{min} = -20 °C and T_{max} = 210 °C seemed to provide the best performance for this set of compounds, with the exception of benzene. With these modulator temperatures and the other operating conditions used in this series of experiments, $n_{p,GCxGC}$ was 216 on the basis of the n-decane t_R and *fwhm* values (n_{p1} = 18; n_{p2} = 12) and 60 on the basis of 2-heptanone t_R and *fwhm* values (the latter allows comparisons with data from the next series of experiments).

5.3.2 Flow rate

In GC×GC, it is generally necessary to compromise between optimal carrier gas velocities for the ^{1}D and ^{2}D columns, because they are connected in series and F cannot be adjusted

independently. In general, F should be adjusted such that the maximum ^{2}D t_R value is less than P_M. This places a constraint on the minimum F value. At higher F values, several issues can arise. First, the trapping capacity of the modulator can be exceeded because of sample overloading or because insufficient time is available for the first stage to cool down after the first modulation heating event. Second, M_R values can be reduced because the peaks eluting from the ^{1}D column are narrower [39]. Third, the retention on the ^{2}D column could be reduced to a point where resolution is compromised. These factors, thus, place constraints on the maximum F value.

Golay plots generated separately for each column using He as carrier gas, (n-octane, k = 2.7, 33 °C for ^{1}D; and n-tridecane, k = 2, 80 °C for ^{2}D) indicated optimal velocity values, u_{opt}, of 37 and 14 cm/s for the ^{1}D and ^{2}D column, with H_{min} values of 0.028 and 0.017 cm, respectively. The corresponding values of N are 3570 and 5500 plates/m, respectively. This translates to F values of 1.2 mL/min for ^{1}D column, and 0.06 mL/min for ^{2}D column. The effect of F was explored for a subset of 5 test compounds (i.e., benzene, isoamyl alcohol, hexanal, n-octane, and 2-heptanone) at discrete F values of 0.1, 0.4, 0.9, and 1.5 mL/min. Values of the other relevant operating variables are given in the caption of Figure 5-2.

As shown in the 2-D chromatograms in Figure 5-2d-f, increasing F leads to a commensurate decrease in the ^{1}D column t_R values of all compounds. Notwithstanding the breakthrough of benzene under these conditions, the effects on the ^{2}D column separation vary. At F = 0.1 mL/min the ^{2}D t_R values exceeded P_M and all compounds exhibited wrap around, however, all compounds were well separated (data not shown). Due to the broadness of the ^{1}D peaks at this low flow rate, the M_R values were > 3 and the separation required 4.4 min. The large *fwhm* values of the primary modulated peaks of the compounds are also attributed to the low F in the ^{2}D column (e.g., n-octane *fwhm* = 627 ms).

At F = 0.4 mL/min (Figure 5-2d), all compounds were effectively separated in 1.6 min. R_{s2} was 2.7, M_R values ranged from 2.5 to 3.5, and the *fwhm* for the primary modulated peak of n-octane was 130 ms. On the basis of 2-heptanone, the $n_{p,GC\times GC}$ for this flow rate is 72 (n_{p1} = 9; n_{p2} = 8). At F = 0.9 mL/min (Figure 5-2e), the compounds were also effectively separated, R_{s2} was 2.5, M_R values ranged from 2 to 3, and the separation required 1.1 min. The *fwhm* for the primary modulated peak of n-octane was 76 ms. On the basis of 2-heptanone, the $n_{p,GC\times GC}$ for this modulation period is 60 (n_{p1} = 6 and n_{p2} = 10); slightly lower than at 0.4 mL/min. Increasing F to 1.5 mL/min (Figure 5-2f) led to very short t_R values on the ^{2}D column. R_{s2} was not calculated due to breakthrough of n-octane, however, the resolution among the other compounds was lower than that at 0.9 mL/min. At this F, the base peak widths from the ^{1}D column decreased to where M_R values were < 2. The separation required <1 min. Although similar results were obtained for F values of 0.4 and 0.9 mL/min, the latter was deemed preferable because it reduced the analysis time by 30% with minimal reductions in R_{s2} (8% reduction) and $n_{p,GCxGC}$ (10% reduction).

5.3.3 Modulation period

For the next series of tests, P_M was varied from 2 to 10 s while keeping all other variables at the values shown in the caption of Figure 5-2e. The same subset of five test vapors was used. The shortest P_M value of 2 s (Figure 5-2g) resulted in breakthrough for all compounds due to insufficient time for cooling the μTM stages between successive heating events. There was also evidence of wrap-around for those compounds with t_R (^{2}D) close to 2 s. At P_M = 4 s (Figure 5-2h), all compounds were effectively separated, R_{s2} was 2.4, M_R values ranged from 2.2 - 3, and the separation required 1.1 min. The *fwhm* for the primary modulated peak of n-octane was 80 ms. On the basis of 2-heptanone, the $n_{p,GC\times GC}$ for this modulation period is 57 (n_{p1} = 6; n_{p2} = 9.5). The data

for P_M = 6 s was already presented in Figure 5-2e. R_{s2} was 2.2, M_R values ranged from 2.0 - 3.0, and the ^{2}D t_R values were similar to those with P_M = 4 s. Despite the slightly smaller values of M_R and R_s, a P_M of 6 s is considered preferable to 4 s because it allows more time for the ^{2}D separation and a slightly higher $n_{p,GC\times GC.}$ (i.e., 60, based on 2-heptanone, see above)**.**

At P_M = 10 s (Figure 5-2i), all compounds were effectively separated and only benzene suffered breakthrough. At this P_M value breakthrough might have been expected due to the limited capacity of the μTM, however, none was observed for other compounds. R_{s2} was reduced to 1.6 and M_R values were < 1.5 for all compounds, which is less than optimal, since the resolution in ^{2}D is degraded. The separation required 1.1 min. The *fwhm* of the principal modulated peak for n-octane was 78 ms. The $n_{p,GC\times GC}$ value determined on the basis of 2-heptanone increases to 78 (n_{p1} = 6; n_{p2} = 13) primarily by virtue of using the value of P_M as the default retention time in the peak capacity calculation. It is clear from Figure 5-2i that one would want to operate at a lower flow rate to take full advantage of such a long P_M setting.

5.3.4 Reproducibility

To examine reproducibility, four replicate separations were performed for the same subset of five test compounds used in previous experiments under the conditions presented in Figure 5-2e. Table 5-S1 (Supporting Information) shows the relative standard deviation (RSD) of the ^{2}D t_R values and the total area of the modulated peaks. The former ranged from 2.2% for 2-heptanone to 4.6% for isoamyl alcohol and is largely a consequence of the lack of an automatic modulation event start timer for the GC×GC analysis. The tailing peaks obtained for isoamyl alcohol in the ^{2}D column contribute to its higher RSD value. The sums of the modulated peak areas show a similar degree of variability, with RSDs ranging from 1-5%. RSD values of the peak areas for individual

modulated peaks, also shown in Table 5-S1, are as high as 7%, undoubtedly due to changes in modulation phase associated with slight changes in the timing of the modulations [40].

5.3.5. Structured chromatogram

Figure 5-3 shows more clearly the effect of the different stationary phases of the two columns. A mixture of 12 compounds composed of sets of n-alkanes (n-heptane, n-octane, n-nonane), aromatics (toluene, m-xylene, cumene), aldehydes (hexanal, heptanal, benzaldehyde) and alcohols (1-propanol, 1-hexanol, 2-heptanol) was separated using the conditions described above (see Figure 5-2e).

The alkanes eluted in order of *bp* from the ^{1}D column and were well separated, but they were not retained significantly on the polar ^{2}D column. The aromatic compounds also eluted in order of *bp* from the ^{1}D column and were retained only slightly longer than the alkanes on the ^{2}D column, due to p-π interactions with the ether moieties on the PEG stationary phase of the ^{2}D column. The ketones and aldehydes also showed *bp* separations on the ^{1}D column and moderate retention on the ^{2}D column that reflects their relative polarities and the dominance of dipole-dipole interactions with the PEG. Note that several of these compounds co-eluted with the aromatics and alkanes on the ^{1}D column, but they were separated on the ^{2}D column. As expected the alcohols, except 1-propanol, had the largest t_R values on the ^{2}D column by virtue of strong dipolar and hydrogen-bonding interactions with the PEG. The relative low ^{2}D t_R for 1-propanol can be explained by its high polarity and high volatility, which lead to second-stage breakthrough, as seen for benzene in previous experiments.

The grouping of homologues within a functional group class is a well-known feature/advantage of GC×GC analyses of complex samples, where compound-specific analyses

are often not necessary or feasible [27]. Although a high degree of orthogonality is observed between the ^{1}D and ^{2}D column separations, the increase in ^{2}D retention time with increasing carbon number within a homologous group reflects some residual volatility-based separation. This could be reduced or eliminated with temperature programming of the ^{2}D column.

5.3.6. Fast GC×GC separation of a moderately complex mixture

Figure 5-4a shows the chromatogram from the ^{1}D column (i.e., bypassing the μTM and ^{2}D column) of a 21-component test mixture containing compounds spanning a *bp* range of 80 °C (benzene) to 178 °C (benzaldehyde). The column temperature was 33 °C and *F* had to be increased to ~ 5 mL/min to obtain t_R values similar to those for the ^{1}D column obtained at 0.9 mL/min with the GC×GC set-up (Figure 5-4b). Peak assignments are based on individual runs of each component. The total analysis time was only 3 min. Overall, good peak shapes were obtained with some tailing of the more polar compounds. The following full or partially co-elutions are apparent: peaks 3/4 (1-propanol/n-heptane), 9/10 (cyclopentanone/isoamyl alcohol), 14/15 (n-nonane/cumene), and 13/21 (2-heptanone /benzaldehyde). The n_p for this chromatogram is ~ 31 on the basis of the n-decane t_R value. Note that the relatively high value of *F* employed in this 1-D separation is well above the optimal value. However, operating at F = 1.2 mL/min (corresponding to u_{opt}) increased the total separation time 3-fold (i.e., to 9 min).

Figure 5-4b shows the GC×GC chromatogram for the same mixture with the same modulator settings and operating conditions as used in the preceding section. Peaks 1, 2, and 3 correspond to the most volatile members of the mixture, benzene, trichloroethylene and 1-propanol, respectively. They all showed evidence of breakthrough, as expected (*vida supra*). The peaks of the polar compounds (i.e., peaks 17, 18, 20, 13, and 21) were broader than those of

the non-polar compounds due to the longer ^{2}D t_R values. Values of *fwhm* of the primary modulated peaks ranged from 75 ms (n-heptane) to 900 ms (benzaldehyde). All of the overlapping peaks in the ^{1}D separation (Figure 5-4a) are resolved in the ^{2}D dimension, however peaks 8/11 (2-hexanone/m-xylene) are only partially resolved in the 2-D plot. The $n_{p,GC\times GC}$ is ~ 216.

5.4 Conclusions

This is the first study to demonstrate GC×GC separations with a μTM. Short ^{1}D and ^{2}D columns were employed in anticipation of using microfabricated columns to assemble a μGC×μGC system, which resulted in fast separations even for the moderately complex mixtures tested. The effects of the key operating variables T_{min}, T_{max}, O_s, P_m, and F on the quality of isothermal GC×GC separations were rationalized in terms of the trapping capacity and transfer efficiency of the μTM, and the retention time on the ^{2}D column. Results demonstrate that under proper operating conditions the performance of this robust μTM rivals that of some commercial modulators requiring much higher operating power or consumable cryogenic fluids.

Due to the need to control the ^{1}D column temperature by means of a conventional GC oven in this series of experiments, the lowest value of T_{min} achievable was limited by the oven temperature, which in turn reduced the trapping efficiency of the more volatile compounds tested. This problem will be easily resolved in the planned μGC × μGC system by using on-chip heaters and temperature sensors to control the ^{1}D and ^{2}D microcolumn temperatures. Thermal crosstalk between stages also contributed to breakthrough of the more volatile compounds, and the relatively slow cooling time of the μTM stages limited the minimum P_M to about 4 s. These issues should be resolved by increasing the length of the inter-stage interconnection channel and reducing

the air gap between the μTM and the TEC (at the cost of somewhat greater heating power dissipation), respectively.

Although a T_{max} of 210 °C was sufficient to remobilize even the least volatile compounds tested here, a higher T_{max} would be required to analyze mixtures containing components with boiling points > 200 °C (e.g. essential oils, pesticides, and diesel fuel). Furthermore, progressive ramping of T_{min} and T_{max} would be required to analyze more complex mixtures. The former may require use of a different stationary phase in the modulator due to the possibility of excessive bleed at higher temperatures. The latter could be addressed by implementation of temperature controllers to coordinate T_{min} and T_{max} with the (micro)column temperature program over the course of the separation, while maintaining a constant value of ΔT [33]. These modifications would increase the range of compounds and the effective peak capacity of a μGC×μGC system.

5.5. References

1. W. C. Tian, H. K. L. Chan, C. J. Lu, S. W. Pang, E. T. Zellers. *J. Microelectromech. Syst*., 2005, 14, 498-507.
2. R. P. Manginell, D. R. Akins, M. W. Moorman, R. Hadizadeh, D. Copic, D. A. Porter, J. M. Anderson, V. M. Hietala, J. R. Bryan, D. R. Wheeler, K. B. Pfeifer, A. Rumpf. *J. MEMS*, 2008, 17, 1396-1407
3. B. Alfeeli, D. Cho, M. Ashraf-Khorassani, L. T. Taylor, M. Agah. *Sens. Actuators B*, 2008, 133, 24-32.
4. S. Reidy, G. Lambertus, J. Reece, R. Sacks. *Anal. Chem*., 2006, 78, 2623-2630.
5. A.D. Radadia, R.I. Masel, M.A. Shannon, J.P. Jerrell, and K.R. Cadwallader. *Anal. Chem*., 2008, 80, 4087- 4094.
6. M. A. Zarejan-Jahromi, M. Ashraf-Khorassani, L. T. Taylor, M. Agah. *J. Microelectromech. Systems*, 2009, 18, 28-37.
7. G. Serrano, S. M. Reidy, E. T. Zellers. *Sens. Actuators. B.*, 2009, 141, 217-226.
8. Q. Y. Cai, E. T. Zellers. *Anal. Chem.*, 2002, 74, 3533-3539.
9. R-S. Jian, R-X. Huang, C-J. Lu. *Talanta*, 2012, 88, 160-167.
10. M. Li, E. B. Myers, H. X. Tang, S. J. Aldridge, H. C. McCaig, J. J. Whiting, R. J. Simonson, N. S. Lewis, M. L. Roukes. *Nano Letters*, 2010, 10, 3899-3903.
11. K. Reddy, Y. Guo, J. Liu, W. Lee, M. K. K. Oo, X. D. Fan. *Sensors Actuators B*, 2011, 159, 60-65.

12. D. Cruz, J. P. Chang, S. K. Showalter, F. Gelbard, R. P. Manginell, M. G. Blain. *Sensors Actuators B*, 2007, 121, 414-422.
13. P. Galambos, J. Lantz, M. S. Baker, J. McClain, G. R. Bogart, R. J. Simonson. *J. MEMS*, 2011, 20, 1150-1162.
14. G.R. Lambertus, C.S. Fix, S.M. Reidy, R. Miller, D. Wheeler, E. Nazarov, R.D. Sacks, *Anal. Chem*., 2005, 77, 7563-7571.
15. G. Serrano, H. Chang, E. T. Zellers. *Proc. Transducers 09'*, Denver, Co, USA, June 2009, pp. 1654-1657.
16. S.K. Kim, H. Chang, E.T. Zellers. *Proc. Transducers 09',* Denver, Colorado, USA, June 21-25, 2009, pp. 719-723.
17. Canary-Three, Defiant Technologies, available at http://www.defiant-tech.com/canarythree.php, accessed February 2012.
18. C. J. Lu, W. Steineker, W. C. Tian, M. Oborny, J. Nichols, M. Agah, J. Potkay, H. Chang, J. Driscoll, R. Sacks, K. Wise, S. Pang, E. T. Zellers. *Lab Chip*, 2005, 5, 1123-1131.
19. P. R. Lewis, R. P. Manginell, D. R. Adkins, R. J. Kottenstette, D. Wheeler, S. Sokolowski, D. E. Trudell, J. Bymes, M. Okandan, J. M. Bauer, R. G. Manley, G. C. Frye-Mason. *IEEE Sensors J.*, 2006, 6, 784-795.
20. S. Zampolli, I. Elmi, F. Mancarella, P. Betti, E. Dalcanale, G. C. Cardinali, M. Severi. *Sens. Actuators B*, 2009, 141, 322-328.
21. E. T. Zellers, G. Serrano, H. Chang, L. K. Amos. *Proc. Transducers 11'*, Beijing, China, June 5-9, pp. 2082-2085.
22. S. K. Kim, H. Chang, E. T. Zellers. *Anal. Chem.*, 2011, 83, 7198-7206.
23. R. P. Manginell, J. M. Bauer, M. W. Moorman, L. J. Sanchez, J. M. Anderson, J. J. Whiting, D. A. Porter, D. Copic, K. E. Achyuthan. *Sensors*, 2011, 11, 6517-6532.
24. S. K. Kim, D. R. Burris, H. Chang, J. Bryant-Genevier, E. T. Zellers. *Environ. Sci. Technol.*, *accepted*.
25. S. K. Kim, D. R. Burris, H. Chang, J. Bryant-Genevier, K. A. Gorder, E. M. Dettenmaier, E. T. Zellers. *Environ. Sci. Technol.*, *accepted.*
26. V. R. Reid, R. E. Synovec. *Talanta*, 2008, 76, 703-717.
27. J. Dalluge, J. Beens, U. T. Brinkman. *J. Chromatogr. A*, 2003, 1000, 69-108.
28. R. E. Mohler, B. J. Prazen, R. E. Synovec. *Anal. Chim. Acta*, 2006, 555, 68-74.
29. J. V. Seeley, N. J. Micyus, S. V. Bandurski, S. K. Seeley, J. D. McCurry. *Anal. Chem.*, 2007, 79, 1840-1847.
30. J. B. Philips, R. B. Gaines, J. Blomberg, F. W. M. Van der Wielen, J. M. Dimandja, V. Green, J. Granger, D. Patterson, L. Racovalis, H. J. de Geus, J. de Boer, P. Haglund, J. Lipsky, V. Sinha, E. B. Ledford. *J. High Res. Chromatogr.*, 1999, 22, 3-10.
31. M. Adahchour, J. Beens, U. A. T. Brinkman. *Analyst*, 2003, 128, 213-216.
32. a. J. Harynuk, T. Gorecki. *J. Chromatogr. A*, 2003, 1019, 53-63; b. O. Panic, T. Gorecki, C. McNeish, A. H. Goldstein, B. J. Williams, D. R. Worton, S. V. Hering, N. H. Kreisberg, *J. Chromatogr. A*, 2011, 1218, 3070-3079.
33. F. Begnaud, C. Debonneville, J-P. Probst, A. Chaintreau, P. D. Morrison, J. L. Adcock, P. J. Marriott. *J. Sep. Sci.*, 2009, 32, 3144-3151.
34. M. Libardoni, C. Fix, J. H. Waite, R. Sacks. *Analytical Methods*, 2010, 2, 936-943.
35. S.-J. Kim, S. M. Reidy, B. P. Block, K. D. Wise, E. T. Zellers, K. Kurabayashi. *Lab Chip*, 2010, 10, 1647-1654.

36. S.-J. Kim, G. Serrano, K. D. Wise, K. Kurabayashi, E. T. Zellers. *Anal. Chem.*, 2011, 83, 5556-5562.
37. D. Paul, G. Serrano, E. T. Zellers, K. Kurabayashi. *Proc. MEMS '12*, Paris, France, Jan 29 - Feb 2, pp. 96-99.
38. R.L. Grob, Modern Practice of Gas Chromatography, 3rd Ed, Wiley-Interscience, New York, 2005, Chapter 3.
39. W. Khummueng, J. Harynuk, P. J. Marriott. *Anal. Chem.*, 2006, 78, 4578-4587.
40. R. A. Shellie, L.-L. Xie, P. J. Marriot, *J. Chromatogr. A*, 2002, 968, 161-170.

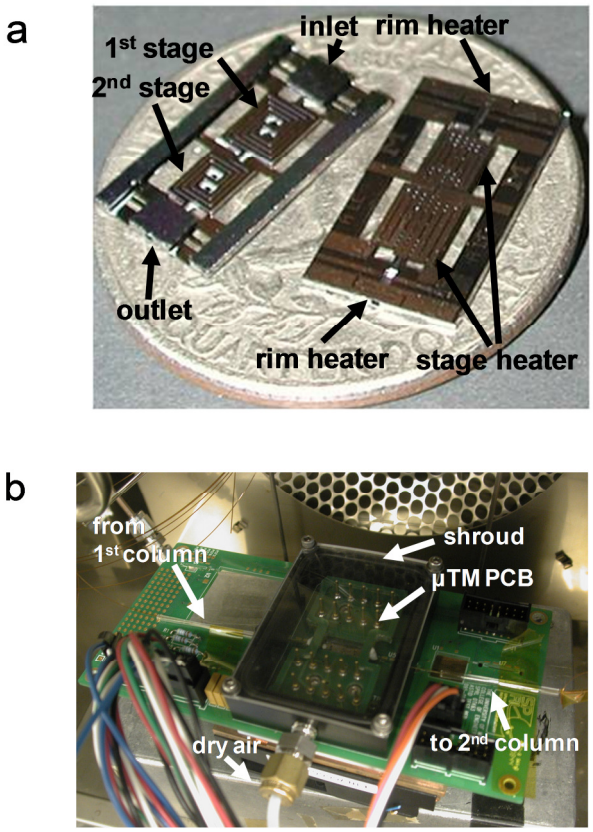

Figure 5-1. (a) Photograph of the microfabricated two-stage thermal modulator (µTM), with labels identifying the essential features; (b) Photograph of the fully assembled µTM mounted on a printed circuit board (PCB). The TEC is located beneath the µTM PCB and the ^{1}D and ^{2}D columns are beyond the field of view.

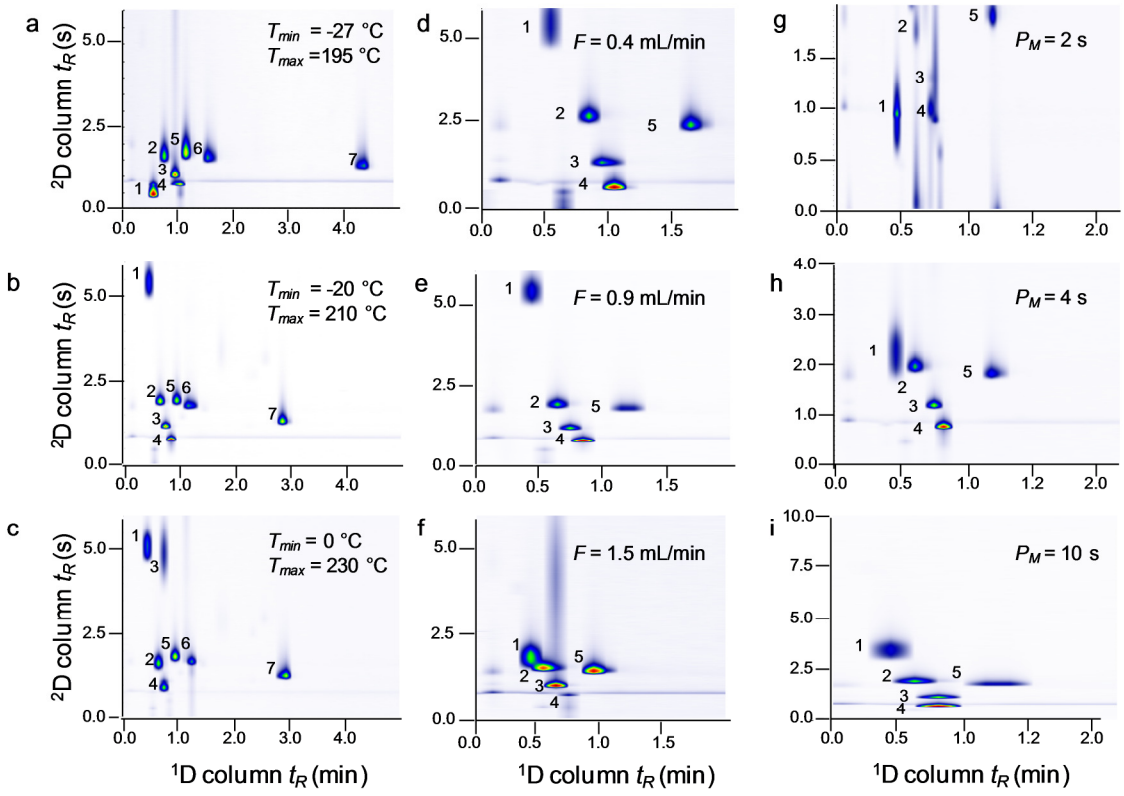

Figure 5-2. 2-D chromatogram showing the effect of the modulator temperatures (a, b, c), volumetric flow rate (d, e, f), and modulation period (g, h, i) on the quality of separations; ^{1}D column temperature = 33 °C (25 °C for (a)), ^{2}D column temperature = 80 °C. Conditions for a, b, and c: F = 0.9 mL/min, P_M = 6 s, O_s = 600 ms. Conditions for d, e, and f: P_M = 6 s, O_s = 600 ms, T_{min} = -20 °C, T_{max} = 210 °C. Conditions for g, h, and i: F = 0.9 mL/min, O_s = 600 ms, T_{min} = -20 °C, T_{max} = 210 °C. Compounds: 1, benzene; 2, isoamyl alcohol; 3, hexanal; 4, n-octane; 5, 2-methyl-2-hexanol; 6, 2-heptanone; 7, n-decane.

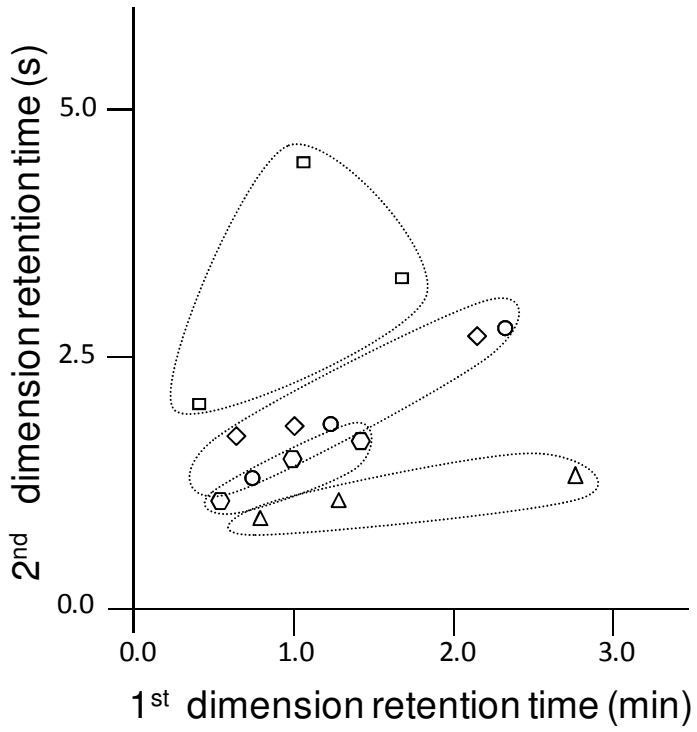

Figure 5-3. Structured chromatogram of compounds from several functional group classes. Symbols designate subsets: triangles for alkanes (in order of ^{1}D t_R, n-heptane, n-octane, n-nonane); hexagons for aromatics (in order of ^{1}D t_R, toluene, m-xylene, cumene); circles for ketones (in order of ^{1}D t_R, 2-hexanone, cyclopentanone, 2-heptanone); diamonds for aldehydes (in order of ^{1}D t_R, hexanal, heptanal, benzaldehyde); and squares for alcohols (in order of ^{1}D t_R, 1-propanol, 1-hexanol, 2-heptanol).

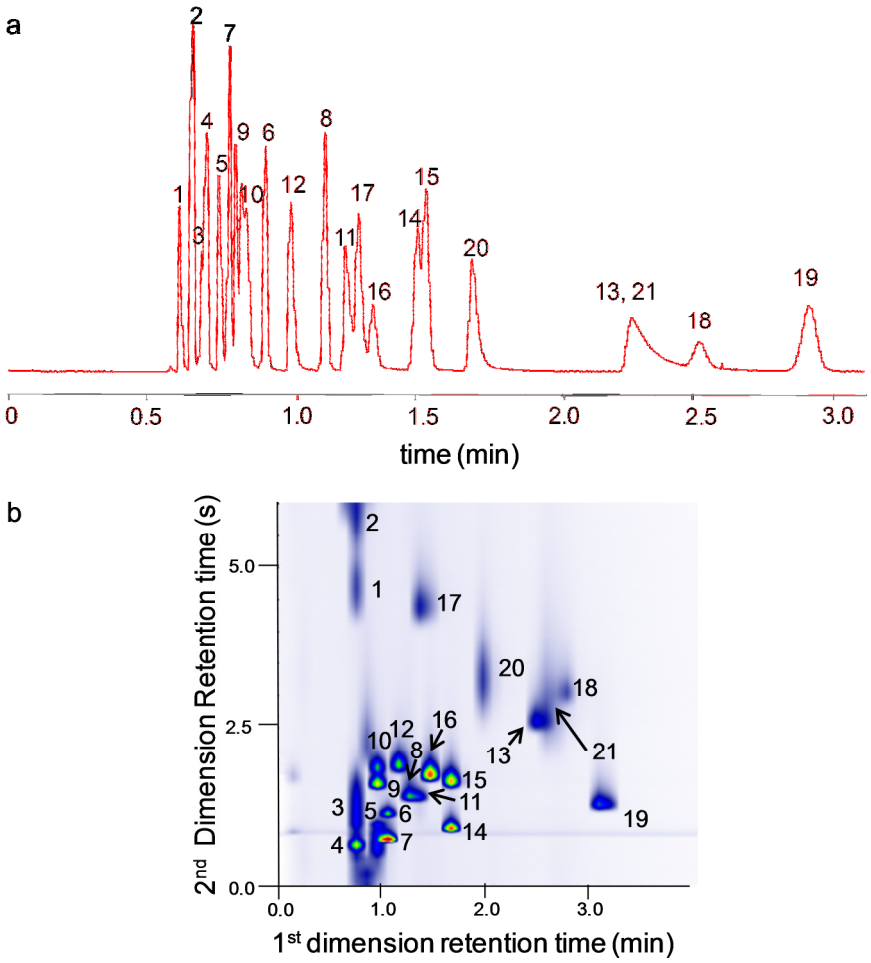

Figure 5-4. (a) 1-D chromatogram of a 21-component mixture (16-20 ng of each compound, injected as vapor). Conditions: 6-m, 0.25 mm i.d. PDMS (0.25 µm thickness); 33 °C (oven); F = 5 mL/min, FID. (b) GC×GC chromatogram of the same mixture. The ^{1}D column was same used for the 1-D chromatogram (33 °C), the ^{2}D column was a 0.5-m, 0.10 mm i.d. PEG (0.10 µm thickness, 80 °C), F = 0.9 mL/min, T_{min}/T_{max} = -20/210 °C, P_M = 6 s, O_s = 600 ms, FID. Compounds (*bp*, °C): 1, benzene (80); 2, trichloroethylene (87); 3, 1-propanol (97); 4, n-heptane (98); 5, toluene (111); 6, hexanal (119-124); 7, n-octane (125); 8, 2-hexanone (127); 9, cyclopentanone (130); 10, isoamyl alcohol (131); 11, m-xylene (139); 12, 2-methyl-2-hexanol (141); 13, 2-heptanone (150); 14, n-nonane (151); 15, cumene (152); 16, heptanal (153); 17, 1-hexanol (155-159); 18, octanal (171); 19, n-decane (174); 20, 1-heptanol (175); 21, benzaldehyde (178).

APPENDIX III

µTM Mounting. The µTM chip was mounted with epoxy (EE129-4, Epoxy Technology, Billerica, MA) and wirebonded to a custom printed circuit board having a central rectangular cut out that allowed access to the underside of the chip. Two microfabricated Si spacer structures (7.5 × 4.5 mm, and 7.5 × 3.5 mm, for the first and second stage, respectively) were affixed to the Pyrex beneath each stage using thermally conductive paste (Silicon Heat Sink 340, Dow Corning, Midland, MI). Each spacer has a central mesa structure the cross section of which matches that of the overlying stage. The air gap between the mesa and the device substrate (Pyrex) was 19 µm. In addition, a pair of 3×3 mm, 450-µm thick Si slabs was inserted between each Si spacer and the TEC surface to localize the cooling to the regions beneath the stages. A thin layer of thermally conductive paste was spread on both surfaces of the Si slabs to ensure good thermal contact between the TEC and the device. This assembly was inverted and manually mounted and aligned on the top surface of the four-stage TEC (SP2394, Marlow Industries, Dallas, TX). A small axial fan (E1U-N7BCC-03, Sundial Micro, Ontario, CA) was placed below the TEC to facilitate heat dissipation. Finally, a shallow, rectangular glass shroud with a thick frame was bolted to the top side of the PCB on which the µTM was mounted. A barbed fitting in one wall of the frame permitted a tube to be connected for purging the µTM and TEC surfaces with dried house air to prevent ice formation.

Table 5-A1. Reproducibility of the t_R values and areas of modulated peaks eluting from the ^{2}D column.[a]

compound	t_{R2} (s)	Peak area (pA·s)[b]			
		mod 1	mod 2	mod 3	A_t
benzene	1.31 (3.6)	0.08 (4.5)	0.70 (5.9)	n/a	0.78 (4.9)
hexanal	1.52 (4.7)	0.09 (5.7)	0.51 (0.8)	0.06 (6.7)	0.66 (2.6)
isoamyl alcohol	1.87 (2.9)	0.07 (5.9)	0.13 (5.4)	0.23 (6.0)	0.43 (5.0)
n-octane	2.57 (2.8)	0.41 (2.8)	0.17 (5.4)	0.08 (4.9)	0.66 (1.0)
2-heptanone	2.76 (2.2)	0.21 (5.5)	0.23 (4.7)	0.07 (3.6)	0.51 (1.3)

[a] From replicate sample-loop injections of test atmospheres containing 16-18 ng of each vapor (n = 4). Values in parentheses are RSDs (%). Conditions: ^{1}D column temp.: 33 °C, ^{2}D column temp. = 80 °C, F = 0.9 mL/min, T_{min}/T_{max} = -20/210 °C, P_M = 6 s, O_s = 600 ms, FID.

[b] mod 1, 2, and 3 refer to the series of modulated peaks for a given compound; A_t = total area of all modulated peaks.

CHAPTER VI

Summary and Conclusions

The preceding chapters of this dissertation have described a series of projects related to the development and characterization of microanalytical systems for determining airborne volatile and semi-volatile organic compounds (VOC and SVOC) at low concentrations in complex mixtures. The broad goals were 1) to demonstrate rapid, automated analyses of selected markers of the explosive trinitrotoluene (TNT) at low- or sub-parts-per-billion (ppb) concentrations in the presence of expected background (S)VOCs with a field-portable microfabricated gas chromatograph (μGC) prototype, and 2) to demonstrate rapid, comprehensive two-dimensional GC (GC×GC) separations of moderately complex VOC mixture components using a novel microfabricated thermal modulator (μTM).

A primary emphasis was placed on developing the fieldable μGC prototype, which was configured specifically to provide rapid determinations of TNT marker compounds for ultimate deployment at airports for screening passengers and luggage. One project, described in Chapter 2, was concerned with developing a front-end, multi-stage preconcentrator-focuser (PCF) module for a μGC that was capable of rapidly sampling a relatively large air volume and capturing the markers partially selectively, focusing them, and then injecting them to a downstream separation column and detector. The next project, described in Chapter 3, concerned the assembly and testing of a

laboratory μGC prototype, dubbed INTREPID-I, that incorporated all essential system components and was capable of performing semi-automated analyses of the TNT markers. The third project, described in Chapter 4, concerned the assembly and testing of the fieldable μGC prototype, dubbed INTREPID II, for fully automated air monitoring of the TNT markers. The final project, described in Chapter 5, concerned demonstrating GC×GC separations of VOC mixture components using a μTM.

Each of these independent yet interrelated projects contributed to the overall goals of the dissertation. The most important results from this body of work are summarized, briefly, immediately below. First, a multi-stage preconcentrator-focuser (PCF) module designed for use in a μGC for the determination of selected markers of TNT is assembled and exhaustively characterized. The module had three fluidically-linked components and was shown capable of sampling 1 L of air, focusing the marker compounds, and injecting them to a downstream separation column and detector within 60 sec with a transfer efficiency of ~80-94%. This study built on a previous project in the group concerned with designing a selective PCF module for trichloroethylene. Similar design features are incorporated into this PCF module but the set of targets was more difficult to deal with because of their high polarity and low volatility. This is the first study to systematically design such a module for the fast analysis of TNT marker compounds in the vapor phase; it should be adaptable to other portable systems requiring rapid sampling, preconcentration, focusing and injection of similar SVOCs. Second, a fully automated field-ready μGC prototype was produced, which combined an adsorbent-packed, deep-reactive-ion-etched (DRIE) Si/glass microfocuser (μF), a 1×1cm^2 long DRIE-Si/glass separation microcolumn, and a nanoparticle-coated chemiresistor microsensor array with a PCF module, and was capable of analyzing explosive marker compounds in the vapor phase in about 2 min. Third, a GC×GC

subsystem that coupled primary (^{1}D) and secondary (^{2}D) fused-silica capillary columns to a mid-point μTM was assembled. This work was an extension of the studies by our collaborators Dr. Sung-Jin Kim and Prof. Katsuo Kurabayashi from the Mechanical Engineering Deparment at the University of Michigan, who designed, built and characterized the μTM used in this study. This is the first study to demonstrate GC×GC separations with a μTM.

Chapters 2-4 concern the development of a μGC prototype for markers of TNT. These markers included 2,4-dinitrotoluene (2,4-DNT), 2,6-dinitrotoluene (2,6-DNT), which are natural byproducts of TNT production and are found as impurities in all explosives employing TNT, and the taggant 2,3-dimethyl-2,3-dinitrobutane (DMNB), which is added to TNT and other explosives produced in the U.S and other United Nations affiliated countries.

Since the vapor pressures of these compounds, and their anticipated environmental concentrations are quite low (i.e., < 0.001 torr), it was necessary to include the PCF module to reduce analysis time while also achieving low limits of detection. Chapter 2 describes the assembly and characterization of this multi-stage PCF module. In addition to the preconcentrating the target analytes, the PCF module was designed to be partially selective – allowing only those VOCs and SVOCs with vapor pressures near those of the marker compounds to be captured and passed to the separation and detection modules. This was achieved by selecting the appropriate type and quantity of adsorbent materials, and the appropriate operating conditions, to allow compounds more volatile than the target analytes to pass unretained, and to preclude, via a pre-trap, compounds much less volatile than the target analytes from entering the instrument. The selectivity imparted to the sampling function reduced the complexity of the sample reaching the separation and detection modules, thereby significantly reducing the analysis time.

The PCF module consists of three components. The first component is a pre-trap, a commercial membrane filter for removing particles and low volatility interferences. The second component is a high-volume sampler that comprised a stainless steel tube packed with the graphitized carbons Carbopack B® (30 mg) and Carbopack Y® (15 mg), which traps the target analytes but permits more volatile interferences to pass through largely unretained, and the third component is a microfocuser (μF), packed with ~2 mg of Carbopack B®, which is used to generate sharp injection bands. The sample is first collected in the sampler, then thermally desorbed, passed to the μF, and then thermally desorbed/injected into the downstream separation (micro)column. The adsorption capacities, sampling and desorption flow rates, and heating profiles were optimized for each device while minimizing the analysis time.

Results showed that the optimized sampler (~40 °C) has < 10% breakthrough for a 1 L sample captured at 3 L/min and > 90 % transfer to the μF in 40 sec when heated to 225 ºC with a 40 mL/min desorption flow rate. The μF can provide injection bandwidths of ~ 2 sec (DMNB) when heated to 250 °C in 0.6 sec at a desorption flow rate of 3 mL/min, which is compatible with (micro)column separations. Transfer efficiency of ~ 86 ±5% and 94 % for DMNB, and 80±5% and 83 % for 2,4-DNT, were obtained for the markes at 0.2 and 2.5 ppb, respectively. The selective preconcentration, injection and separation of the markers in the presence of 22 interferences were demonstrated. These results demonstrated that the PFC module is suitable as a front-end sampler of the INTREPID μGC prototypes, and possibly, other portable instruments that require a fast collection of sVOCs.

Although this project was successful, several issues arose that deserve mention here, and that should be considered in future work that might be done related to this subsystem. Among those issues, the presence of carry over proved to be a problem when connecting the PCF module

to the μGC prototype, and more tests are required to determine the problem. The use of a filter as a pre-trap, although effective to unretained 2,4-DNT, should be tested to trap interferences less volatile than 2,4-DNT. In addition, the long-term reproducibility of the transfer efficiency needs to be tested to evaluate the performance of the PCF for continuous monitoring of the explosive markers.

As the PCF module was being developed, work was also performed on the development of the INTREPID-I μGC lab prototype, as described in Chapter 3. A series of experiments was performed with individual components and then with subsystems and, ultimately, the entire system. Using a DRIE-Si/glass microcolumn (1-m channel length, 150 × 240 μm cross-section, 1 cm^2 footprint, 0.15μm of PDMS stationary phase) connected to a standard GC injector and an FID detector, tests were run with mixtures containing TNT, the targets and alkanes of similar volatility. Results showed that the microcolumn had enough resolution to efficiently separate the explosive markers from co-contaminants of similar volatility. Fast (15-sec) separations were achieved by using the on-column heaters and temperature programming the column (up to 180 °C). The sensor array employed consisted of two integrated array of 4 chemiresistors coated with functionalized thiolate- monolayer-protected gold nanoparticle (MPN) interface layers. Upon integrating the sensor array with the microcolumn, however, the resolution was severely degraded. Results indicated that the sensor array, which was heated to 70 °C, is the major contributor to extra peak band broadening. This can be caused by wall adsorption of the high molecular weight compounds into the walls of the detector cell (Macor® lid). Wall adsorption can be reduced by increasing the baseline temperature of the sensor array, however, sensitivity and lifetime of the MPNs films is significantly reduce at higher temperatures. In addition, dead volume inside the detector cell can also be a contributor factor to band broadening.

The INTREPID-I lab prototype interfaced the PCF module to the 1- µcolumn and CR array. In addition INTREPID-I consisted of several valves, pumps and controllers that allow the user to operate among thee different modes: sampling, focusing, and analysis. An in-house written labVIEW software was used as an interface to operate the modes in a laptop. A full analysis of the target compounds DMNB, 2,4- and 2,6-DNT, and n-tridecane, which was used as a representative interference was achieved in < 3 minutes with LODs in the sub-parts-per-billion range for a preconcentrated air-sample volume of 1 L. Results from Chapter 3 were used to guide several design modifications incorporated in the INTREPID-II µGC field prototype (Chapter 4), including a faster sampling time by operating at higher sampling flow rates, reduction of injection band width by use of on-column focusing, implementation of high-speed temperature programming to improve chromatographic resolution and reduce analysis time, and use of localized heating mechanisms to reduce footprint and power dissipation of the system. The fluidic system was also improved by the use of a manifold that integrated the valves, and pumps, and all other fluidic connections.

Characterization OF INTREPID II included calibration, limits of detection, chromatographic resolution of TNT markers from complex mixtures, and response patterns from the CR array. Results obtained with an analytical subsystem consisting of the µF, 1-m µcolumn, and CR array, showed that the calibration curves of the TNT markers were linear for each sensor ($R^2 > 0.97$). The limits of detection for DMNB, 2,6-DNT and 2,4-DNT were 2.2, 0.5 and 0.9 ng, respectively. For a 1-L sample volume, these LODs were equivalent to 0.3, 0.8 and 0.12 ppb, respectively. In both cases, HME was the most sensitive MNP in the CR array, due to the greater affinity of the polar target analytes towards the polar HME. Quantitative results could not be

generated with the fully integrated μGC system, due to residual quantities of the explosive markers after subsequent analysis.

Using, the fully integrated INTREPID-II μGC system, a mixture of 24 compounds, including the TNT markers were sampled, focused, separated and detected. Most of the VOCs passed unretained, and only compounds with p_v values < 2.7 torr were effectively captured and analyzed. The two target analytes, DMNB and 2,4-DNT were completely resolved and eluted within 60 sec. At this point, 2,6-DNT was removed from the set of markers because it was realized that its vapor concentration would be so much lower than those of the other two markers and that it would contribute relatively little to the problem of explosive detection. Response patterns, derived from the CR sensor array responses were obtained for each target analyte and an n-alkane co-contaminant. The overall analytical cycle time was ~ 2 min distributed as follow: sampling (22 sec), focusing (40 sec), stabilization (5 sec), and analysis (55 sec). The sensitivity, selectivity, and analytical cycle time demonstrated here, coupled with the capability of autonomous operation and portability of the instrument, indicate that the INTREPID μGC would be effective for selectively detecting markers of TNT in a timely manner, suitable for homeland security applications.

Future work needs to be performed to improve the performance of INTREPID μGC, which include identifying the source of carry over; this can be due to an inefficient heating of the sampler, or cold spots in the fluidic path. In addition, other work that can be done to improve the performance of the μGC includes the design of a peak deconvolution algorithm for adequate peak identification, the use of other stationary phases in the microcolumn with increased selectivity towards the target compounds, and the use of thinner MPN films coatings to reduce residence time of analytes in the sensor surface. The use of shorter microcolumns can also be explored to reduce analysis time. Further modifications can also be made to the μGC hardware components, such as a

more efficient localized heating mechanism, and a new manifold design with a shorten fluidic paths to reduce possibility of cold spots. The use of microcontrollers, instead of LabVIEW-based controllers, and surface-mount technology (SMT) electronics, will greatly reduce the footprint of the μGC system, making it more portable. Finally, the ultimate goal is to deploy this μGC system for explosive marker detection in a real environment (e.g. personnel or luggage).

The assembly and characterization of a fast GC×GC system with a mid-point μTM for analysis of indoor VOC air contaminants was presented in Chapter 5. Short ^{1}D and ^{2}D fused-silica capillary columns were employed in anticipation of using microfabricated columns to assemble a μGC×μGC system, which resulted in fast separations even for the moderately complex mixtures tested. Using sets of 5-7 volatile test compounds (boiling point ≤ 174 °C), the effects of the minimum (T_{min}) and maximum (T_{max}) modulation temperature, stage heating lag/offset (O_s), modulation period (P_M), and volumetric flow rate (F) on the quality of the separations were evaluated with respect to several performance metrics, including resolution, peak capacity, and *fwhm*. Best results were obtained with a T_{min} = -20 °C, T_{max} = 210 °C, O_s = 600 ms, P_M = 6 s, and F = 0.9 mL/min. Replicate modulated peak areas and retention times were reproducible to < 5%. A structured 9-component GC×GC chromatogram was produced, and a 21-component separation was achieved in < 3 min under isothermal conditions. Results demonstrate that under proper operating conditions the performance of this robust μTM rivals that of some commercial modulators requiring much higher operating power, as well as consumable cryogenic fluids.

There are some tasks not included in this dissertation that could be performed in the near future to improve the performance of the μTM and GC×GC system. Thermal crosstalk between μTM stages contributed to breakthrough of the more volatile compounds, and the relatively slow cooling time of the μTM stages limited the minimum P_M to about 4 s. These issues could be

resolved by increasing the length of the inter-stage interconnection channel and reducing the air gap between the μTM and the TEC, respectively. In addition, although a T_{max} of 210 °C was sufficient to remobilize even the least volatile compounds tested here, a higher T_{max} would be required to analyze less volatile compounds; furthermore, progressive ramping of T_{min} and T_{max} can be explored to analyze more complex mixtures. Ultimately, the μTM should be implemented into a μGC system to develop the first μGC×μGC system.

In conclusion, this dissertation reports the first field deployable μGC for trace-level determination of TNT markers in a mixture of VOC air contaminants. This μGC is one of very few portable systems specifically engineered for the analysis of trace amounts of explosive markers in vapor phase. In addition, the INTREPID μGC possesses other advantages, which include sub-ppb detection limits achievable with a 20-sec short preconcentration period, and the ability to discriminate the target analytes from possible interferences by means of selective preconcentration, chromatographic separation and unique response patterns. This dissertation also reports the first GC×GC separations with a μTM. This is a significant contribution to the emerging field of comprehensive GC×GC gas chromatography. Results demonstrated performance comparable to GC×GC systems with macroscale thermal modulators, but with significant less power consumption and without the need of cryogenic material.

The research has contributed to the advancements of MEMS technology for air monitoring applications. Microfabricated devices that can be engineered to serve a specific purpose (e.g. μF, μcolumn, μsensor, μTM) possess several inherent advantages, including small fluidic path dimensions, low-power heating, and low dead volumes. The integration of these devices with other non-microfabricated components, controllers, and electronics, as described in this document,

has enormous potential for re-defining the next generation of direct-reading air monitoring instrumentation.